Spring 4-9-2018

Patient Specific Radiation Doses From Projection Radiography Images: Improving the Accuracy of Low Dose Radiation Calculations

Daniel J. Sandoval
University of New Mexico - Main Campus

Recommended Citation

Daniel J. Sandoval
Candidate

Nuclear Engineering
Department

This dissertation is approved, and it is acceptable in quality and form for publication:

Approved by the Dissertation Committee:

Reed G. Selwyn , Chairperson

Gary W. Cooper

Adam Hecht

Shuang Luan

i

**PATIENT SPECIFIC RADIATION DOSES FROM
PROJECTION RADIOGRAPHY IMAGES:
IMPROVING THE ACCURACY OF LOW DOSE
RADIATION CALCULATIONS**

by

DANIEL J. SANDOVAL, MS DABR

B.S., Mathematics Education, University of New Mexico, 1999
M.S., Nuclear Engineering, University of New Mexico, 2008

DISSERTATION

Submitted in Partial Fulfillment of the
Requirements for the Degree of

**Doctor of Philosophy
Engineering**

The University of New Mexico
Albuquerque, New Mexico

May 2018

DEDICATION

To Kristen, Gabriel, and Roman, thank you for all of your love and support. You are my strength and my love, I know I could not have done any of this without you.

To Irene Sandoval, you were always proud of me no matter what, I wanted so much for you to see me finish this. Thank you for always supporting us in everything we do, I miss you every day mom.

To Dr. Phil Heintz, without you, none of this would have happened. I wish you could have seen it completed.

ACKNOWLEDGEMENTS

Patient Specific Radiation Doses from Projection Radiography

Images: Improving the accuracy of low dose radiation calculations

By

Daniel J. Sandoval

B.S. Mathematics Education, University of New Mexico, 1999

M.S., Nuclear Engineering, University of New Mexico, 2008

Ph.D., Engineering, University of New Mexico, 2018

ABSTRACT

Due to an increase in regulatory scrutiny and medical facility accreditation requirements to monitor patient radiation dose from diagnostic imaging procedures, there is a growing necessity to determine and record accurate patient radiation dose from diagnostic medical imaging procedures. Current methods of patient dosimetry in diagnostic imaging are both extremely difficult and time consuming, require large computing resources (such as Monte Carlo computations), or lack accuracy due to using data based on homogenous materials and "standard-man sized" anthropomorphic models.

This dissertation provides an algorithm that calculates a more accurate dose using patient-specific projection radiographic images. The algorithm includes measurements acquired during routine physics testing of the x-ray unit, data from

two-view (Anterior-Posterior and Lateral chest) radiographic images, and accounts for patient specific and body habitus.

The algorithm developed in this work uses formulas for calculating entrance and exit dose utilizing a new dose correction factor. The dose correction factor is based on the exposure index and average grayscale from radiographic images specific to the subject and shows improved accuracy of traditional calculation methods for entrance and exit dose calculations.

Measurements using optically stimulated luminescent dosimeters, physics measurements on radiographic equipment, and Monte Carlo simulations were used to test and develop the algorithm. This new algorithm uses the mean radiographic image grayscale value over the region of interest and the reported Exposure Index to create a correction factor to correct patient dose calculations. The final product is an algorithm for calculating patient specific dose from AP and lateral chest radiographs that is more accurate with less associated uncertainty than current traditional dose calculation methods.

Table of Contents

List of Figures

List of Tables

1 Introduction

1.1 Necessity of Patient Radiation Dose Calculations

Recent attention to the rise in diagnostic imaging exams has caused an increase in the scrutiny towards patient radiation dose. Although most of the attention has been towards the escalation in computed tomography (CT) examinations, the use of non-advanced imaging modalities (i.e., not CT, MRI, nuclear medicine, or ultrasound) comprise the majority of all diagnostic imaging procedures [1]. One study of 6 large integrated health systems reported that between 1996 and 2010 there were 30.9 million imaging examinations performed, of which 65% were from non-advanced imaging modalities [2]. Due to its availability, speed and lower cost when compared to other imaging modalities, projection radiography continues to be the most commonly ordered diagnostic imaging exam [3], [4]. The chest radiograph in particular accounts for approximately 45% of all projection radiography exams, consequently adding up to over 150,000,000 chest radiographs performed in the U.S. annually [5].

In 2010, the International Atomic Energy Agency (IAEA) put forth an effort to begin recording patient radiation doses from all diagnostic imaging procedures [6]. In January of 2015, the Joint Commission, one of the foremost accrediting bodies for health care organizations and programs in the United States, changed their accreditation requirements to include tracking of patient radiation dose [7]. Although the push for patient radiation dose tracking stems from the increase in computed tomography (CT) exams, the intent is to eventually track patient specific radiation dose from all diagnostic imaging procedures. This creates an issue, in

1

that, even though projection radiography exams are the most common imaging procedure, the patient-specific dose from these procedures is estimated with a large uncertainty.

1.2 Radiation dose Risk Models

The Linear No-Threshold (LNT) model is currently still the most widely used estimate of risk from radiation exposure. The absence of a lower threshold dose in the LNT model leads to the interpretation that there is no amount of radiation that is safe [8], [9]. Many professional societies, such as the American Association of Physicists in Medicine (AAPM) and the Health Physics Society (HPS), recognize that this model is flawed, especially at low radiation doses. The AAPM has stated "Risks of medical imaging at patient doses below 50 mSv for single procedures or 100 mSv for multiple procedures over short time periods are too low to be detectable and may be nonexistent" [10], [11]. The Health Physics Society has stated "For doses below [50-100mSv] risks of health effects are either too small to be observed or are nonexistent" [10], [12].

Current risk models for estimating risk of cancer induction and fatal cancer induction, are primarily created using the Biological Effects of Ionizing Radiation (BEIR) VII reports. These reports are generally based on data collected from Japanese atomic bomb survivors, where doses were delivered to the whole body and do not adequately account for the different type of exposures, dose rates, and specific organ doses from medical imaging exams [10]. This data also leads to the extrapolation of low dose radiation effects with a substantial level of uncertainty. Risk models developed with these uncertainties are themselves left up to broad

interpretation. Inaccurate low dose calculations are then matched to clinical outcomes that may not be associated with the actual doses at those levels [10], [13], [14].

The LNT model and the arguments against using it lead to the same conclusion: there is a need for more accuracy in the dosimetry of low dose radiation imaging procedures. This project intends to improve the accuracy of low dose radiation calculations by developing a method for calculating patient specific doses for projection radiography exams.

1.3 Current Radiation Dose Calculation Methods

Current mathematical algorithms tend to rely on average patient sizes, or phantom models, and do not account for specific patient differences, such as body habitus, and how these differences may affect not only entrance skin dose (ESD), but dose to specific radiosensitive organs such as lungs, breasts etc. The dose estimates for the "average patient", or standard-man phantom, do not bring us closer to tracking patient specific doses from projection radiography exams. This is due mainly to the fact that patient size, and body habitus, greatly influences the amount of radiation dose a patient receives. Larger patient sizes not only serve to increase the technique (kV and mAs) chosen for radiographic exams, but will also affect the SID and field size needed to encompass all the anatomy.

1.3.1 The Exposure Index

New projection radiography systems attempt to address the concern for patient dose by adding an Exposure Index (EI) to their readout. The initial implementation of the EI was to give the technologist an idea as to the quality of

their images along with a general estimate as to the patient dose [15]. Unfortunately, each vendor initially started with a different method of calculating and displaying the EI, thus making it impossible to accurately compare images and estimated patient doses between various systems [16].

The EI has since evolved to become a standardized metric by which the radiographers are given feedback on the quality of their image, as well as an indirect measure of the exposure to the digital detector [16], [17]. The standardized EI adopted by nearly all of the digital radiography vendors presents a linear relationship between the detector exposure and the EI value as shown in equation 1-1 [18], [19].

$$EI = C_0 \cdot g(V) \qquad\qquad 1\text{-}1$$

Where C_0 is the calibration factor and $g(V)$ is an equipment-specific inverse calibration function of the value of interest, V. V is defined as the air kerma detected at the image receptor under the relevant anatomy as determined by the vendor specific processing algorithms [16], [20], [21].

It has been shown that the EI is a very effective QA tool for monitoring correct use of equipment and tracking variations in detector dose [15], [19]; however, it is widely known that the EI cannot be directly used as a measure of patient radiation dose due to the fact that patient specific factors are not taken into account, such as body habitus and patient thickness [18]. Research has been performed in order to calculate patient entrance exposure and entrance skin dose

4

(ESD), based on the EI of various imaging systems [22], [23], however, these methods assume an average patient size, or standard-man size phantom, and do not accurately take into account varying patient size or body habitus.

1.3.2 Entrance Skin Dose

Historically, patient doses have been determined by first calculating the entrance surface (or skin) dose (ESD), then applying various weighting factors in order to obtain organ dose, or whole body effective dose [24]. The equation for ESD is as follows:

$$ESD = \frac{X * mAs * D^2}{[SID - (t + b)]^2} * BSF \qquad \text{1-2}$$

Where **X** is the x-ray tube output at a known distance, **D**. **X** is typically given in units of dose (Gy) per milliamp-second (mAs). The **mAs** is the product of the tube current and exposure time, which is chosen at the control console. **SID** is the source to image detector distance, **b** is the detector to table top (or detector housing face) distance. The patient thickness is given by the variable **t** [24]–[26]. The final variable is the back scatter factor (**BSF**), which are values usually found in lookup tables produced by measurements with varying field size, HVL and kVp.

The BSFs are typically measured at the surface of a water phantom or water similar material, such as Lucite or some other uniform tissue mimicking material, and have shown differences of up to 10% when compared to each other [27]–[29]. Additionally, BSF measured in uniform materials do not account for the heterogeneous makeup of actual tissue [30]–[32]. It is readily apparent that this

5

basic equation does not take into account the quality, or penetrating power as determined by the kVp and filtration, of the x-ray beam itself.

Stanton et al were able to demonstrate the dependence of BSF on the composition of phantom, with differences of up to 10% between Lucite, tissue and water [30]. This difference is attributed to the quality of the beam as well as the nature of the tissue being irradiated. Without taking into account the beam quality, the traditional calculations ignore the variation of radiation dose deposited in differing tissues.

This method begins with typical ESD calculation

$$ESD \ = \frac{X * mAs * D^2}{[SID - (t + b)]^2} * BSF \qquad\qquad \text{1-1}$$

Where X and D are obtained from previous physics measurements for the kVp selected. mAs, SID, and t (patient thickness) are noted by the technologist. In this step, the only information not readily available is the backscatter factor (BSF) [24]–[26]. There are many sources of backscatter factor tables, and there is good agreement between all of them. For this project, the tables created by Petoussi-Henns et. al which compiles backscatter factors created by Monte Carlo methods for various field sizes, various beam qualities (HVL) and materials (water, ICRU tissue, and PMMA) [29] were used for the backscatter factor data.

Once the ESD is calculated, the exit dose is traditionally calculated by

6

$$exit\ dose = ESD * e^{-\mu d} \qquad\qquad 1\text{-}3$$

Where μ is average linear attenuation coefficient for the material of interest, and d is the total thickness of the subject [33]. As will be discussed later, this simplified calculation neglects to take into account any scatter contributions in the calculation area of interest that may increase the dose.

1.3.3 Monte Carlo Modeling

Monte Carlo modeling has long been used to improve the accuracy of patient dose calculations. Some limitations to using Monte Carlo codes for patient specific dosimetry are the intensive processing times required, as well as the time and effort required for those unfamiliar with programming to accurately set up a simulation. In order to facilitate the use of Monte Carlo simulations, especially for the clinical medical physicist, some companies have created "customizable" programs that allow the user to make certain limited adjustments to the calculation, without having to learn how to program. One such software program, the most readily available, is PCXMC by the Radiation and Nuclear Safety Authority in Finland (STUK) [34]. PCXMC allows the clinical end user to adjust the radiation field size, the source to image distance, and the height and weight of the patient, which it then attempts to model with a mathematical phantom (See Fig 1-1). Other technical factors that need to be supplied by the end user are x-ray tube potential, x-ray tube anode angle, filter material and thickness. This amount of information appears to be the minimum needed in order to create a decent simulation.

7
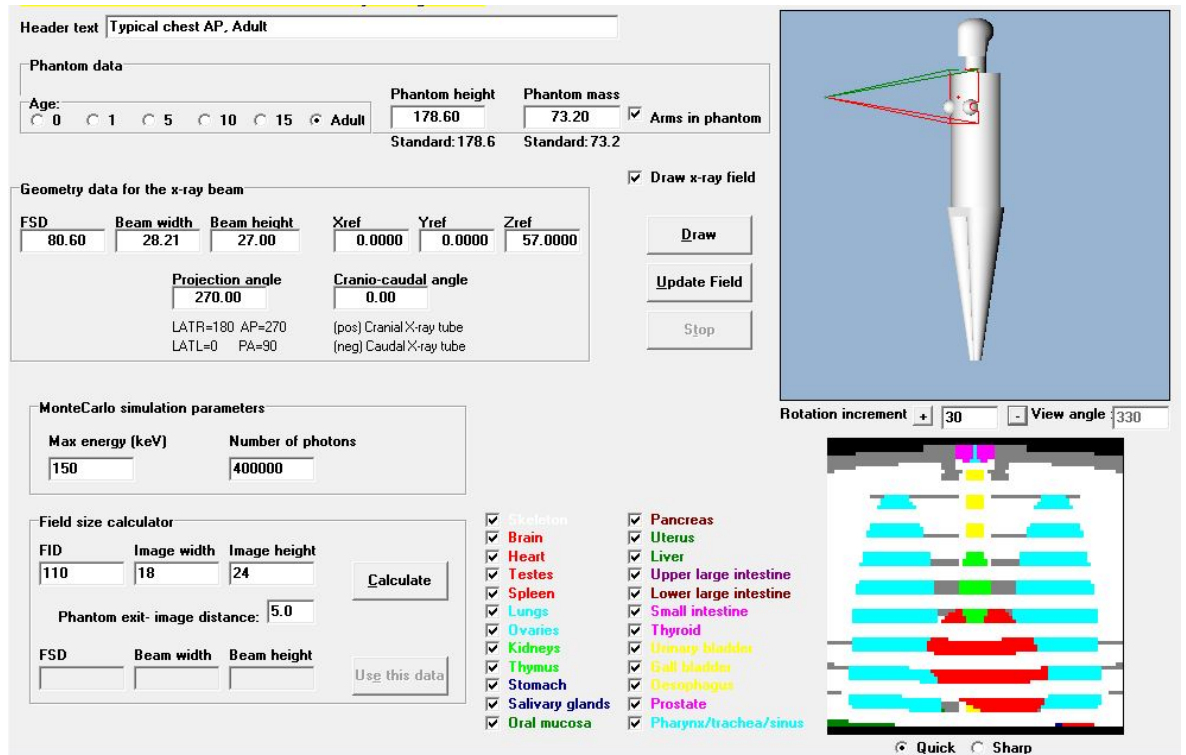
Figure 1-1: Screen capture of the PCXMC interface showing the mathematical model as well as various user customizations.

There are noticeable limitations to the PCXMC software such as constraints on beam characterization, air kerma reference points, and phantom representation. In addition to only being able to model a nearly uniform radiation field, the user defined beam is only capable of minor customizations, such as total filtration rather than beam homogeneity, and air kerma at the "patient entrance" rather than a fixed reproducible point which has been shown to result in variances of up to 40% [35], [36]. However, the main limitation with PCXMC, as with most other Monte Carlo simulations, is the use of a standard mathematical phantom based on the "standard man" philosophy. These phantoms are rarely able to

8

accurately represent the variations in size, shape, and body habitus of real patients. Studies have shown that, due to the use of these standard mathematical phantoms, calculated doses can differ from measured doses by 28-72% [37].

1.4 Lack of accuracy of patient dosimetry

Techniques published to date for attempting to estimate patient dose have relied on average patient sizes, or phantom models, and do not account for specific patient differences, such as body habitus, and how they may affect not only ESD but dose to specific organs such as lungs, breasts etc. Ultimately, dose estimates for the "average patient" do not provide an accurate solution to tracking patient specific doses from projection radiography exams.

In order to improve the accuracy of the dose calculation, specifics of the radiographic equipment in use, such as kV, mAs, Source-to-Image-Distance (SID), x-ray beam quality, patient thickness and patient area irradiated need to be known. Current Digital Radiography (DR) systems are capable of tracking nearly all of the required elements (kV, mAs, SID, area irradiated) except for x-ray beam quality and patient thickness. With little effort, patient thickness can be measured by the technologist, or from the subsequent images, and beam quality can be determined by the medical physicist at acceptance testing and verified annually during equipment surveys or after major service or upgrade. Thus, all required parameters to calculate patient specific dose are available.

1.5 Proposed solution

The final product of this dissertation will provide a validated mathematical algorithm to accurately calculate patient-specific doses based on physics measurements and information available from digital radiographs with improved precision over current methods.

The remaining chapters of this dissertation cover the following:

- Chapter 2: Physics tests and data collection performed on the radiographic unit.

- Chapter 3: Methods for calibration and understanding of nanoDot OSLD dosimeters is discussed.

- Chapter 4: Discussion and testing of Monte Carlo code techniques required to complete the development and validation of the mathematical algorithm.

- Chapter 5: Details of the experimental in situ measurements are provided and discussed.

- Chapter 6: Algorithm development and validation are detailed and discussed in this chapter.

- Chapter 7: This chapter presents the final conclusions, and future work of this dissertation.

2   Physics measurements

Before work can begin on the development of a dosimetry algorithm, it is necessary to understand the imaging equipment being used. Since all radiographic equipment can vary from manufacturer to manufacturer, or even more simply, device to device, it is necessary for medical physicists to perform various measurements on a regular basis to ensure consistency. The measurements outlined below have either been standardized in the medical physics profession, or are adapted from various reputable sources and are widely accepted by various AAPM task groups [38]–[41].

1. Determine Air Kerma (AK) at a reference point for use in projection radiography. This would entail:

    a. Determine AK for various device settings such as kV mAs and focal spot size

    b. Measure AK at a reference point for various kV stations

    c. Calculate the AK in mGy at the reference point, which will give an AK/mAs (mGy/mAs) for each kVp at the reference point

2. Characterize the x-ray beam and radiographic unit by ensuring proper functioning, as applicable, based on standards set forth by the American College of Radiology, The American Association of Physicists in Medicine, New Mexico State Regulations, and the Code of Federal Regulations. The following measurements are typically performed with a commercially available detector system. This would entail:

www.manaraa.com

i. Verification of the kV by measuring accuracy and reproducibility of the kV

　　　b. Measuring the first and second Half Value Layer (HVL) in order to determine the homogeneity coefficient using narrow beam geometry

　　　c. Checking the exposure output and timer reproducibility of the system

　3. Exposure Index calibration check to ensure proper functioning within manufacturer specifications.

2.1 Steps for determining Air Kerma at a reference point

The setup consists of a calibrated ion chamber placed with its center located at the AK reference point (100 cm from the focal spot). The beam is well collimated to cover the ion chamber (5x5 cm field) with only a small margin around the chamber in order to conform to narrow beam geometry standards [42]. The chamber is placed perpendicular to the x-ray tube axis in order to negate the heel effect. There is sufficient space beyond the ion chamber (50 cm) to negate any effects of backscatter [39], [42], which will be accounted for separately.
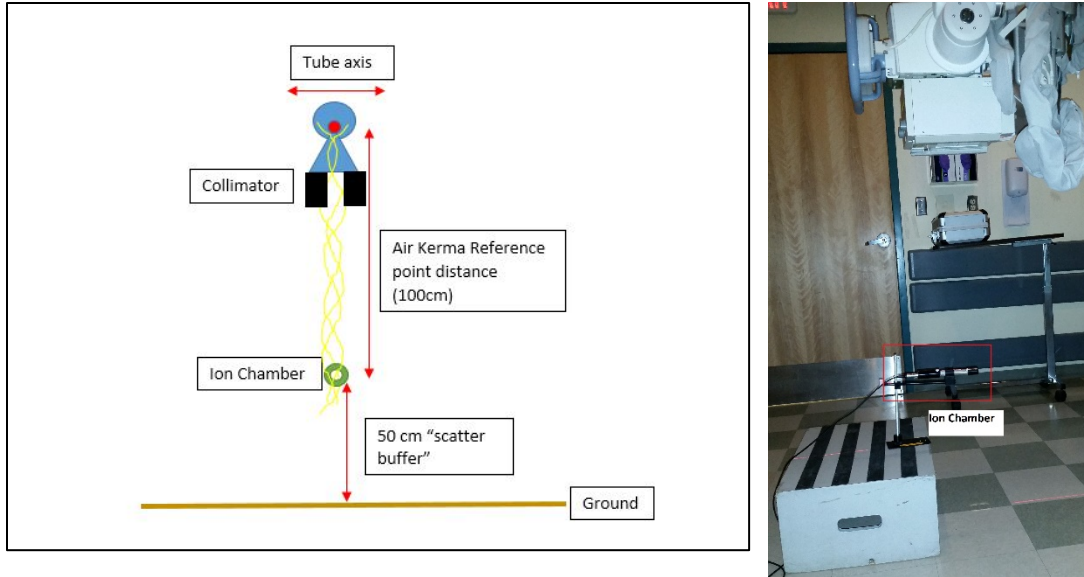
Figure 2-1: a. Diagram of proper setup of air kerma measurement using ion chamber. b. photograph of actual setup.

In addition to ion chamber measurements, it is now acceptable practice by American Board of Radiology certified medical physicists to perform these, and other measurements, using a solid state detector in addition to, or instead of, ion chamber measurements [43], [44]. Therefore, after verification with a NIST traceable ion chamber, most measurements were completed using either a recently calibrated RadCal Accu-gold+ (Radcal, Monrovia, CA), or Raysafe X2 (Fluke Biomedical, Everett, WA) solid state detector system.

Measurements of AK in mGy (or exposure in Roentgen for later conversion to mGy) are taken at a range of kVp stations. Table 2-1 shows the data collected for various kVp stations on the GE Discovery XR656 radiographic unit located in the University of New Mexico Hospital Radiology Department general x-ray room

13

1. The data collected consists of the set kV, the set mAs, measured kVp, and exposure (mR). From these values it is possible to calculate the exposure per milliamp-second (mR/mAs), the AK in mGy at the reference point, and finally the Air Kerma (mGy) per mAs for each kVp at the reference point.

Table 2-1: Data collected at Air Kerma reference point using Radcal Accu-gold+ measurement system.

Set kVp	Set mAs	kVp measured	Exposure (mR)	mR/mAs	AK (mGy)	AK/mAs (mGy)
60	32	60.0	91.62	2.86	0.8026	0.025
80	32	80.4	172.1	5.38	1.507	0.047
100	32	100.7	269.2	8.41	2.358	0.074
110	32	110.9	322.5	10.08	2.825	0.088
120	32	121.2	378.8	11.84	3.318	0.103
125	10	126.7	125.9	12.59	1.103	0.110
130	32	131.4	438.5	13.7	3.841	0.120

The end result from the measurements is an Air Kerma per mAs (AK/mAs) at selected kV stations. From the graph of the AK/mAs as a function of kV (Figure 2-2), the best fit can be solved for an AK/mAs at any kV setting of the system at the given AK reference point.

14
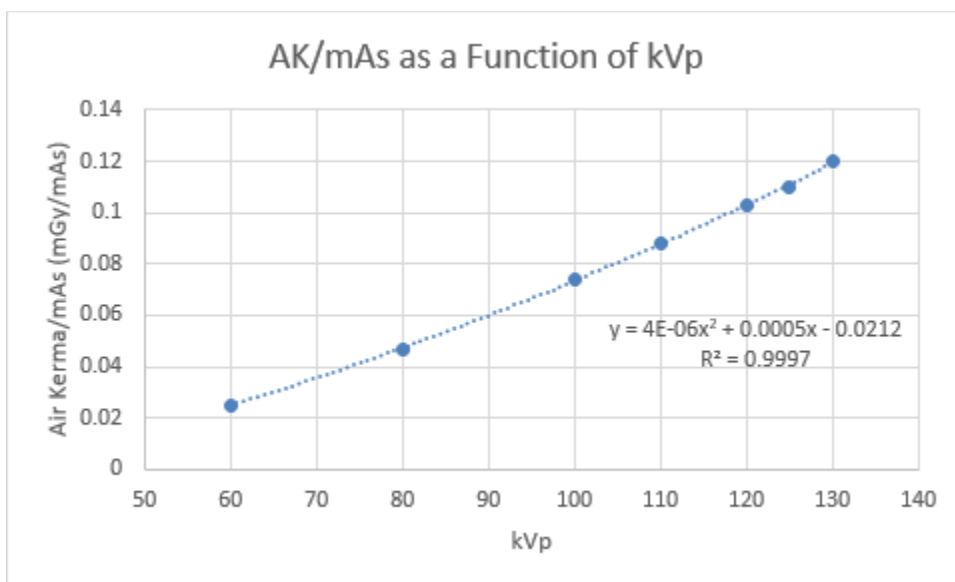
Figure 2-2 Graph depicting AK/mAs as a function of kV for the GE Discovery XR656 radiographic unit.

2.2 Characterization of the x-ray beam

X-ray beam characterization is performed to provide an understanding of how the x-ray beam will interact with various tissues and phantoms due to attenuation and scattering. Medical physicists characterize the x-ray beam using procedures as described below to check the accuracy of the beam energy (verification of kV), the reproducibility of the exposure and timer settings (mAs and timer), and by measuring the 1st and 2nd half value layer in order to calculate the homogeneity coefficient. The homogeneity coefficient describes the polyenergetic character of the beam. A monoenergetic beam has a homogeneity coefficient of 1.0, whereas polyenergetic beams will be <1.0. Typical homogeneity coefficients

15

of diagnostic x-ray beams are between 0.5 – 0.7 and can be used as description of the stability and quality of the x-ray beam as it traverses the subject [45].

Verification of the kV was performed using the Radcal Accu-gold+ system (Radcal, Monrovia, CA) to determine accuracy and reproducibility. Five exposures were made at each of the desired kV stations. The five kV measurements were then used to determine the reproducibility of the exposure (mR/mAs) and exposure time (msec), as well as the accuracy of the kV indicator. The measured kV should be within ±5% of the indicated value as is typical for diagnostic medical physics testing procedures.

Table 2-2 kV accuracy of the GE Discovery XR656 radiographic unit. The percent difference of the selected kV on the unit to the measured kV should be less than 5%.

kVp Set	60	80	100	110	120	125	130
kVp Obs.	60.0	80.4	100.7	110.9	121.2	126.7	131.4
% Diff.	0.0%	0.5%	0.7%	0.8	1.0%	1.4%	1.1%

Reproducibility is determined by the coefficient of variation from the five measurements. A well calibrated x-ray unit should have a coefficient of variation less than 0.05 [38].

Table 2-3 Reproducibility of the exposure and exposure timer at 80kV for the GE Discovery XR656 radiographic unit.

Measurement #	Exposure (mR)	Time (ms)
1	53.3	40.45
2	54.1	40.45
3	53.6	40.45
4	52.4	40.45
5	53.9	40.45
COV	0.01	0.00

The steps for determination of the first and second half value layer outlined below closely follow the process described by several sources [38], [39], [42], [46]. Figure 2-3 details the setup for the HVL measurements.
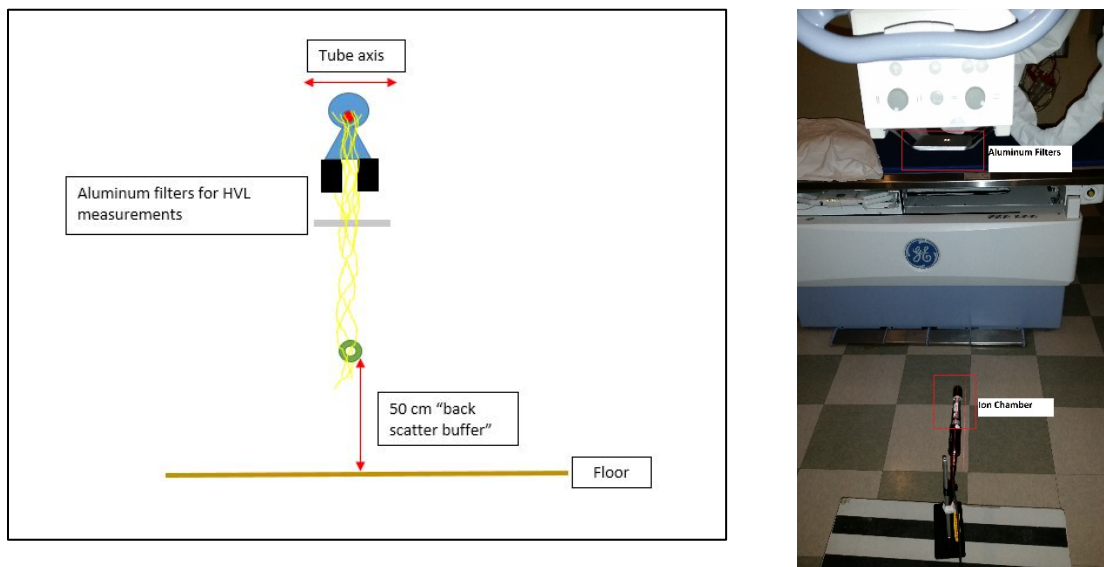
Figure 2-3: a. Diagram depicting HVL measurement setup. Aluminum filters are attached to the collimator. Scatter detected by the ion chamber is reduced due to the "back scatter buffer" beyond the chamber, as well as the distance between the filters and the detector. b. Photograph of actual setup.

Place the 0.6cc calibrated ion chamber 100 cm from the x-ray tube focal spot, leaving at least 50 cm beyond the ion chamber to minimize back scatter contributions. The beam should be collimated to an area around the ion chamber of approximately 5x5 cm, ensuring that the ion chamber is centered in this area and perpendicular to the axis of the x-ray tube. The first exposures made are "free in air" with no attenuating material (other than inherent filtration) between the ion chamber and the x-ray tube. Exposures are made at each kV of interest with a constant mAs setting, and the exposure in Roentgen (R) recorded. Attenuator material is then placed at the face of the collimator in order to minimize any scatter effects from the attenuator material. High-purity (99.9%) aluminum filters are used as attenuator material. The thickness of the attenuator material shall be increased by 1.0mm for each exposure, keeping the kV and mAs constant and the exposure (R) is recorded. This process continues for each added aluminum filter until the exposure measured is reduced to less than 25% of the exposure measured without any attenuator material in place. Once this data is collected for every kV of interest, the results are plotted with the exposure in Roentgen as a function of attenuator thickness in mm.

18
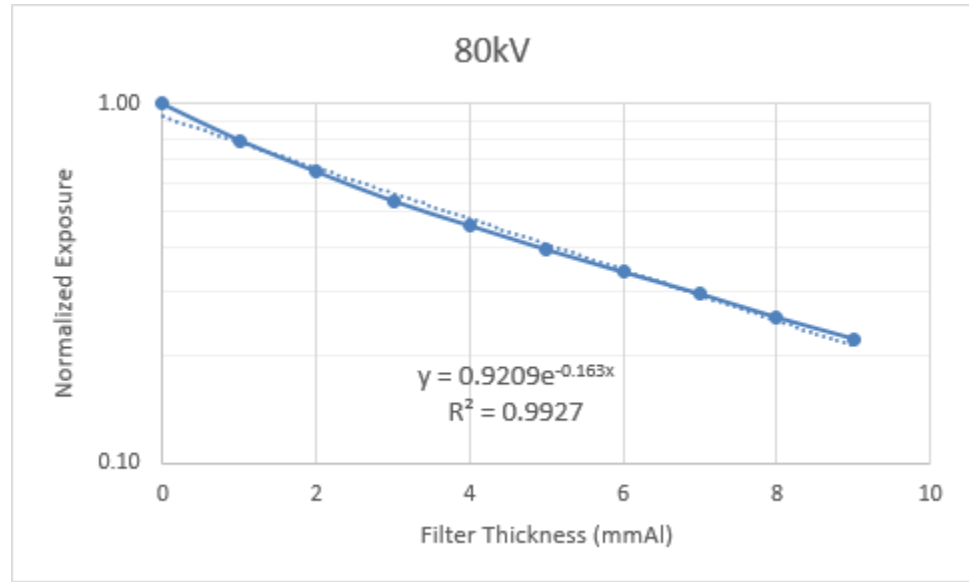
Figure 2-4 Example calculation of first and second Half Value Layer measurements and calculation for GE Discovery unit for 80kVp.

The best fit line for this graph will give a logarithmic equation which can then be solved for the 1st and 2nd HVL of the beam at a given kV. The homogeneity coefficient is calculated by taking the ratio of the 1st to the 2nd HVL. The homogeneity coefficient will be calculated for each kV of interest.

Table 2-4 first and second Half Value layer calculated for kV's of interest on the GE Discovery XR656 unit.

	60 kV	80 kV	100 kV	125 kV
HVL 1 (mmAl)	2.65	3.55	4.40	5.44
HVL 2 (mmAl)	5.76	7.72	9.57	11.83
Homogeneity Factor	0.46	0.46	0.46	0.46

The above measurements were performed in accordance with industry accepted equipment and techniques. If the radiographic equipment was found to

be out of specification, or if any other issues were found, a service call would have been placed and physics measurements repeated before continuing with data collection.

2.3 Exposure Index calibration check

GE X-ray systems define the EI as the ratio between the median image counts within the relevant anatomic region in the value of interest and the uncompensated detector sensitivity:

$$EI = 100[\mu Gy^{-1}] \cdot \frac{Median\ Count\ [counts]}{Detector\ sensitivity\ [\frac{counts}{\mu Gy}]} \qquad \text{2-1}$$

The International Electrotechnical Commission defines the Median Count as "the central tendency of the original data in the relevant image region" [20]. For the GE x-ray system the relevant image region is defined as the anatomic region which is identified from the specific image processing algorithm chosen at the console. The detector sensitivity is an inherent property of the digital detector based on its ability to convert x-ray photons to detected signal and is proportional to counts/ μGy. Therefore, dividing the EI by 100μGy^{-1} is related to the measured dose at the detector [21]. The detector sensitivity has a correction factor that can be adjusted by service personnel during service calls, and therefore should be checked to ensure proper reporting of the Exposure Index for imaging procedures.

The exposure index calibration check for the GE Discovery XR656 radiographic system is performed according to the manufacturer

20

recommendations [21]. The check entails placing the digital detector on the table top, with an SID of 100 cm. No additional filtration, no grid are used. A 20 mm Aluminum block provided by the manufacturer is placed on the face of the collimator, which is fully open. Exposures at 80 kV and varying mAs stations are performed. The digital detector is then replaced with the Radcal-Accugold+ detector and in the same geometry and filter setup. Exposure measurements are repeated for each mAs station. The response of EI should be linear in relation to the air kerma measurements at each mAs station.
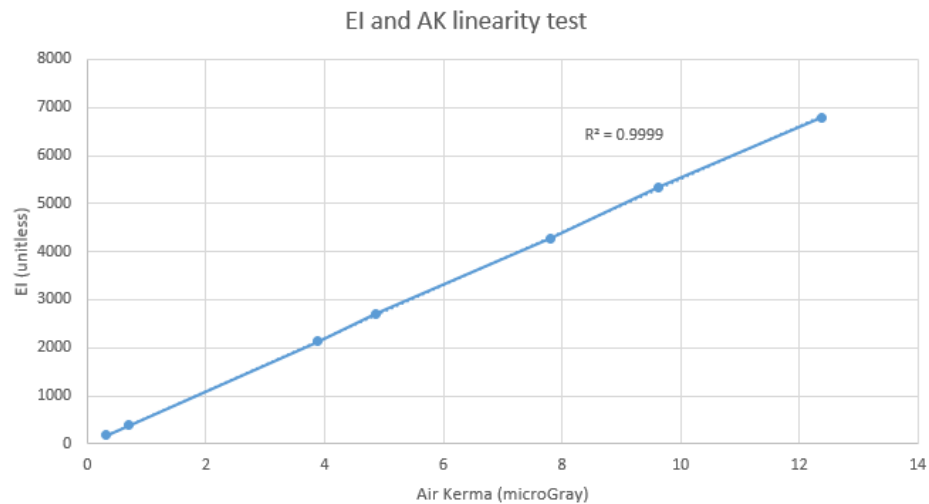
Figure 2-5: Exposure Index and air kerma linearity check.

According to the manufacturer, the relationship between the air kerma and EI/100 when measured at calibration conditions should be 1 to 1 with an allowable accuracy limit of 20% [21]. All recorded EI/100 to air kerma measurements show accuracy to within 5%.

21

3 nanoDot Calibration Methods

In order to validate the accuracy of the new dosimetry algorithm good source of measured data for comparison was required. Monte Carlo modeling has long been used to improve the accuracy of patient dose calculations, so it was determined that Monte Carlo simulations would suffice in providing the necessary data for validation of the new dosimetry algorithm. In order to accurately simulate the dosimetry data, it was necessary to have a pool of measured data that could be compared to the Monte Carlo simulation for accuracy and validity of the code.

Optically stimulated luminescent dosimeters (OSLD), specifically nanoDots by Landauer, were the best choice to provide dose measurement data due to their lower cost, re-usability, accuracy, stability and ease of use [47]–[49].

3.1 nanoDot Calibration

nanoDots are small disks (Diameter 5mm, 0.3mm thickness) of aluminum oxide doped with carbon (Al_2O_3:C) in a dielectric crystalline structure, housed in a thin 10mm x 10mm x 2mm plastic container.
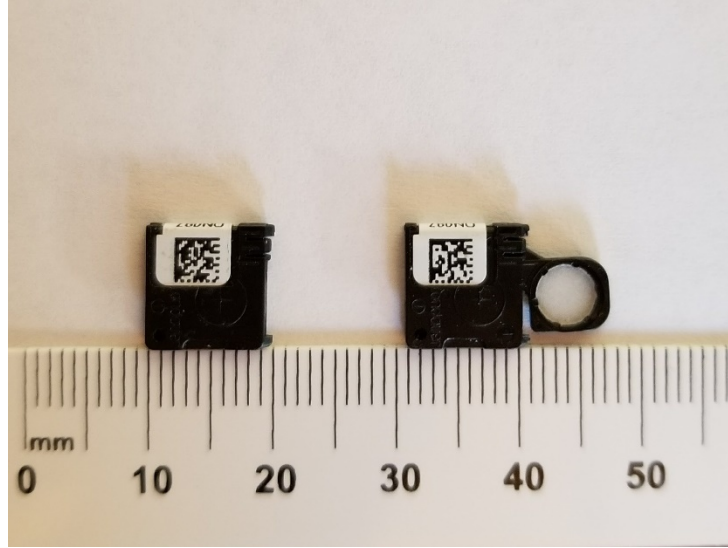
Figure 3-1: Landauer nanoDot optically stimulated luminescent dosimeter (OSLD)

The crystalline structure contains crystal-lattice imperfections that function as electron or hole traps. When the nanoDots are exposed to ionizing radiation, some electrons may gain enough energy to move to generate free electrons at a higher energy level (towards the conduction band) and holes in an amount that is proportional to the exposure, and are stored in the crystalline structure (figure 3-2). When the OSLD is exposed to light, the electrons will gain enough energy in order to escape the trap and recombine with the hole. Since the electrons need to move from a higher energy level to a lower level in order to recombine with the hole, they must give off energy. The energy is emitted in the form of light at a known wavelength (λ = 420nm) as the crystalline structure luminesces [48], [50].

23
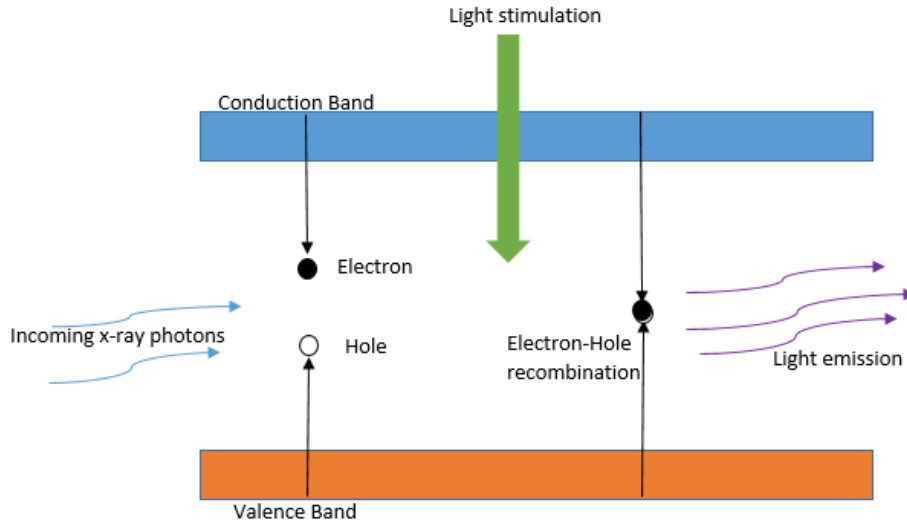
Figure 3-2: Diagram of OSLD. Incoming x-ray photons interact in with the crystalline structure to create an electron-hole pair. Subsequent stimulation by light will allow the electron-hole pair to recombine giving off energy as visible light.

The intensity of the detected luminescence is proportional to the absorbed ionizing radiation dose [48], [51] and a proportionality constant based upon the characteristics of the particular reader and the nanoDots. Therefore, it is necessary to calibrate the microSTAR ii (Landauer) reader for the particular energy range of interest.

The microSTAR ii reader used for this project was in clinical use at the University of New Mexico Cancer Center, it was calibrated for MeV energies in use at the Cancer Center. Therefore, upon receipt of the nanoDot dosimeters, the reader needed to be calibrated for the diagnostic energy range of interest for the measurements in this project. The calibration was performed under the guidance

24

of Angelo Bergamo, PhD. who is responsible for the microSTAR ii system at the UNM Cancer Center, and is familiar with the calibration process.

In order to perform the calibration, a diagnostic energy calibration kit was purchased from Landauer. The calibration kit consists of six calibration nanoDot OSLDs (QC dosimeters) that are exposed to doses ranging from 0 to 100,000 mrad (0 – 100cGy) obtained by the manufacturer at an energy of 80kV and HVL of 2.9 mmAl. Following the instructions included with the microSTAR ii system [52], a linear calibration curve is created for using the calibration nanoDots. The process for creating the curve is as follows:

1. Place the 100,000 mrad QC dosimeter in the microSTARii reader and analyze it ten times. It is required to remove the dosimeter between each reading in order to account for any mechanical variations in positioning or functioning of the reader drawer.

2. Records the counts as displayed for each reading.

3. Compute the coefficient of variation (CV = standard deviation/average reading) for the data set. Ensure that the result is less than 2% per manufacturer requirements. The resultant CV was 1.4%.

4. Next, analyze each QC dosimeter under the "Calibration" tab of the microSTARii reader software under the corresponding calibration selection (High-Dose or Low-Dose) as specified by the manufacturer based on the known dose of each calibration dosimeter.

25

5. After placing the calibration dosimeter in the tray, enter the known dose for each dosimeter in the appropriate box and select "Read". The system will read the dosimeter three times and give the average dose.

6. Each dosimeter should be analyzed three times for a total of nine readings at each dose level.

7. Once all dosimeters have been analyzed three times, click "Accept" to end and store the calibration.

The calibration curve was then tested, as per the instructions, by reading each QC dosimeter 4 times and taking the average of the 12 results. According to the manufacturer, the average of the 4 readings of the QC dosimeters should be within 2% of the known dose; which it was. This calibration process allows the system to accurately create a linear calibration curve for doses less than 300 cGy [51], [53] in the energy range of which is more than adequate for the diagnostic imaging doses expected from this research.

In order to further test the accuracy of the microSTARii and nanoDot system, the nanoDots were taken to an x-ray room along with 20.8 cm of polystyrene blocks. Readings were taken using a 0.6cc calibrated ion chamber used with the Radcal Accu-Gold system placed at the surface of the polystyrene blocks as shown in figure 3-3. The ion chamber comparison is typical in the field of medical physics to check the response and accuracy of new dosimeters.

Figure 3-3: 0.6cc ion chamber placed on surface of polystyrene blocks.

The source to surface distance (SSD) from the focal spot of the x-ray tube to the entrance of the polystyrene blocks was set to 101.6 cm. The x-ray field was collimated to a 5x5cm square around the ion chamber. The ion chamber was then irradiated with an 80kV beam at 2, 4, 8, 16 and 20 mAs. Dose was recorded at each mAs station.

Next, the ion chamber was replaced with a nanoDot keeping the rest of the configuration the same (figure 3-4).

Figure 3-4: nanoDot placement on polystyrene blocks. The rest of the configuration matches the ion chamber setup.

Fifteen different nanoDots were irradiated in this fashion. This experiment was not only used to test the accuracy of the nanoDots and microSTAR ii system,

28

but also to test the sensitivity of the nanoDots themselves. Therefore, fifteen nanoDots were irradiated as shown in the following table.

Table 3-1 nanoDot readouts at varying mAs station and number of exposures.

nanoDot#	mAs	# of exposures	Dose readout (mrad)	Average Dose corrected for number of exposures (mGy)
1	2	1	18.465	0.185
2	2	2	32.019	0.160
3	2	3	48.471	0.162
4	4	1	33.862	0.339
5	4	2	59.895	0.299
6	4	3	88.642	0.295
7	8	1	59.447	0.594
8	8	2	126.964	0.635
9	8	3	178.985	0.597
10	16	1	122.181	1.222
11	16	2	235.829	1.179
12	16	3	344.793	1.149
13	20	1	163.547	1.635
14	20	2	302.027	1.510
15	20	3	459.973	1.533

The readings in table 3-1 were corrected by subtracting the initial readout (pre-exposure) from the post-exposure readout before converting to milligray

29

doses based on the number of associated exposures. This corrected data was then graphed as shown in figure 3-5.
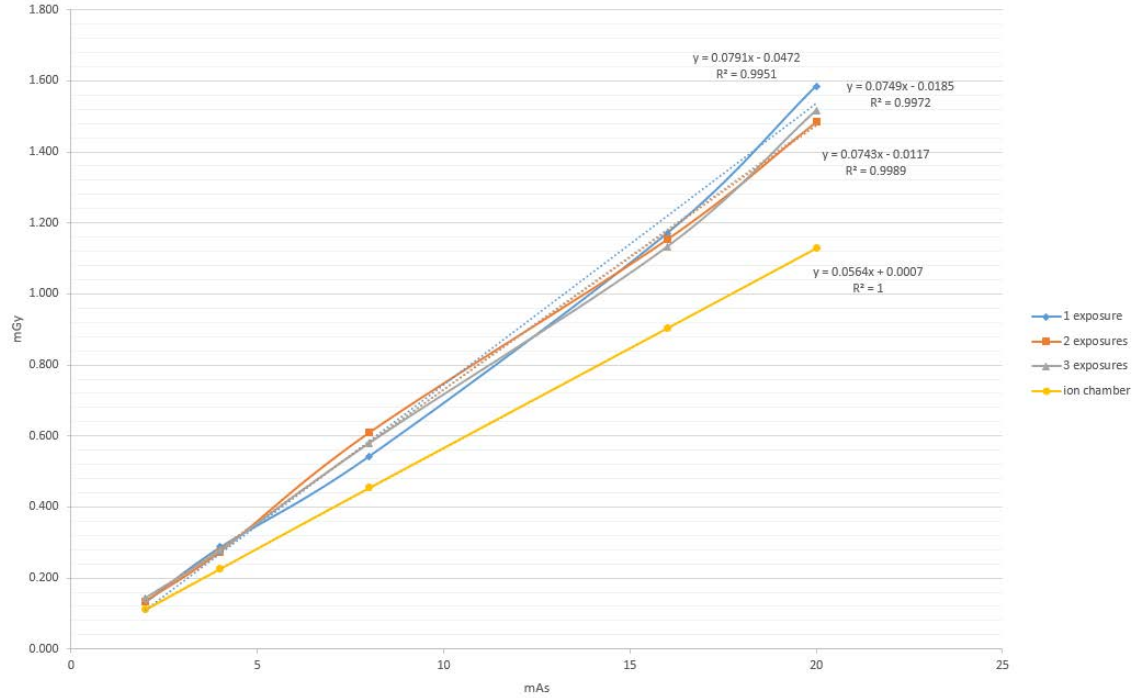
Figure 3-5: Graph comparing Ion chamber measurements on 20.8cm of polystyrene blocks to nanoDots. nanoDots were exposed to 1, 2, or 3 exposures and then corrected and converted to mGy doses for comparison.

From the graph in figure 3-5, the nanoDots have a response similar to that of the air filled ion chamber, although they appear to not respond linearly. It was also determined that exposing the nanoDot dosimeters multiple times improved the accuracy of the measurement. Therefore, all subsequent measurements were performed by exposing the nanoDots more than once for each measurement. The number of exposures used were noted for each experiment for later correction.

To explore the behavior of the nanoDots further, additional measurements were made using higher mAs exposures. The nanoDots were cleared for a period of 22 hours, and then read out again in order to obtain a pre-exposure correction factor. The setup was the same as in Figure 3-5 above. The data from the second experiment are shown in table 3-2.

Table 3-2: second experiment comparing readings from ion chamber and nanoDots.

mAs	Ion chamber (mGy)	nanoDot (mGy)
2	0.13	0.14
4	0.26	0.28
8	0.5	0.6
16	1.0	1.1
20	1.3	1.4
40	2.4	2.8
80	4.8	5.4
100	6.0	7.0
160	9.5	11.1
200	11.9	13.4

The accompanying graph shows similar results as in figure 3-5, where the nanoDots behave similarly to the ion chamber, however not entirely linear.

31
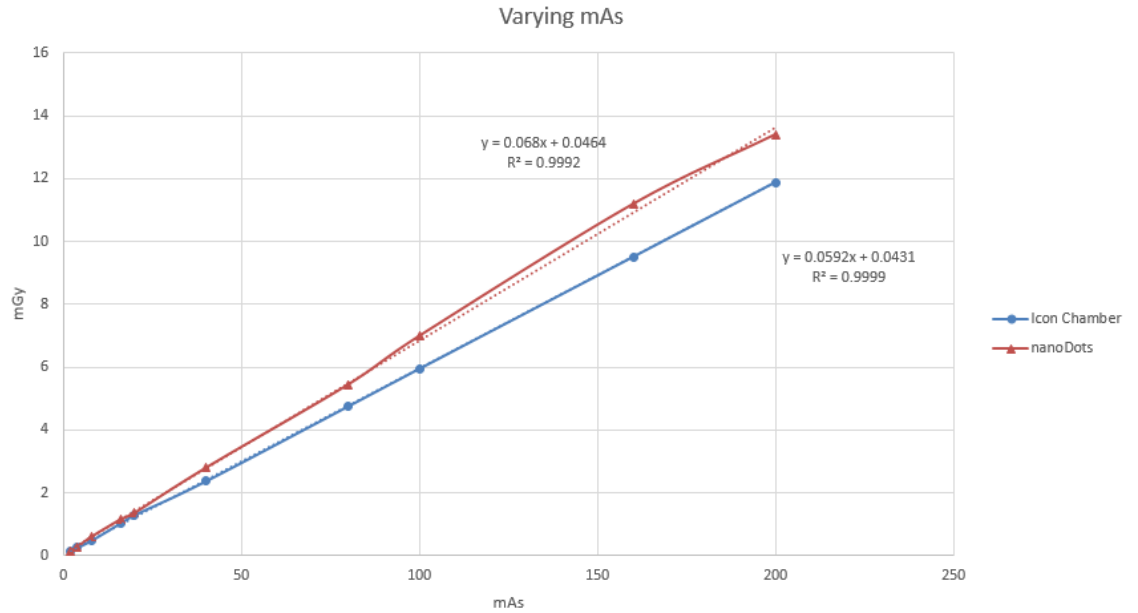
Figure 3-6: nanoDot and ion chamber comparison at 80kV and 2 - 200mAs exposures.

However, when comparing the response of the nanoDots as the mAs (and therefore the dose) increases compared to the ion chamber, by normalizing to the maximum dose for both, the agreement is much closer. Normalized doses for both the ion chamber and the nanoDots are given in table 3-3 and graph of the results in figure 3-7.

32

Table 3-3 Comparison of dose response to increasing mAs for ion chamber and nanoDot dosimeters

Set mAs	Ion chamber normalized dose	nanoDot normalized dose
2	0.01	0.01
4	0.02	0.02
8	0.04	0.04
16	0.08	0.08
20	0.11	0.10
40	0.20	0.21
80	0.40	0.40
100	0.50	0.52
160	0.80	0.84
200	1.00	1.00

33
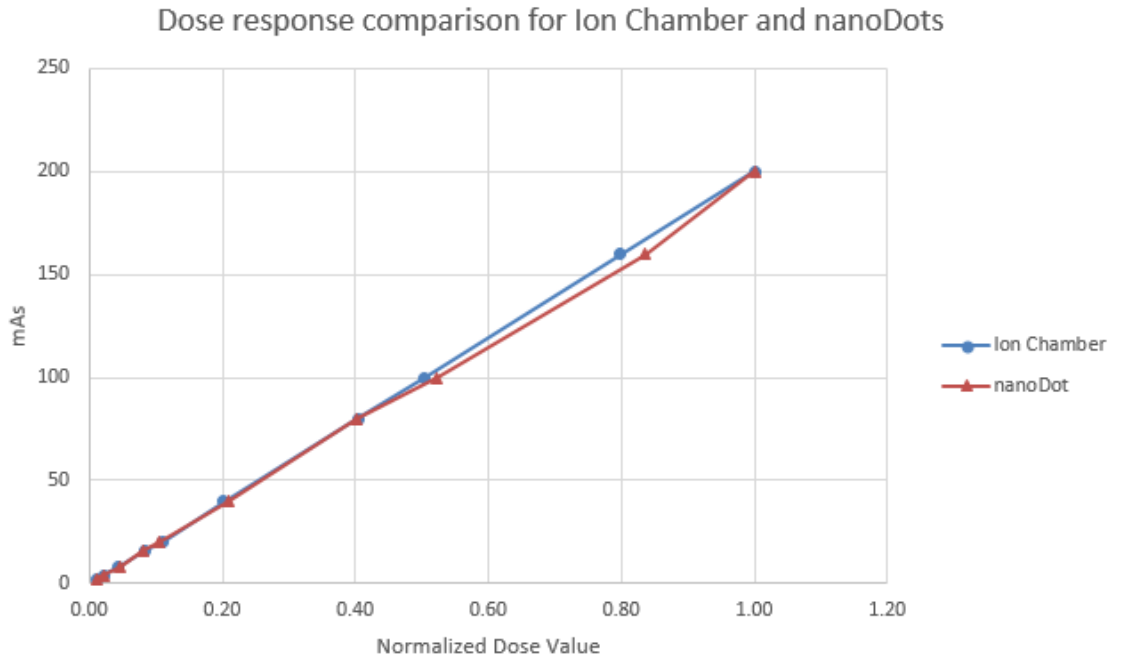
Figure 3-7 Comparison graph of data in Table 3-3

Response to changes of kV were also measured using the same setup as in Figure 3-3. Clinically relevant kV stations were chosen at 60, 80, 100, 120 kV for both ion chamber and nanoDot measurements and exposures were made at 4 mAs. Figure 3-8 shows the graph of the results of the varying kV measurements. nanoDot measurements were performed again using 2 exposures per nanoDot at the same kV and mAs setting. The nanoDot measurements were then corrected for number of exposures and converted to milligray. As shown in the graph in Figure 3-8 response of the nanoDots and the ion chamber are nearly identical.
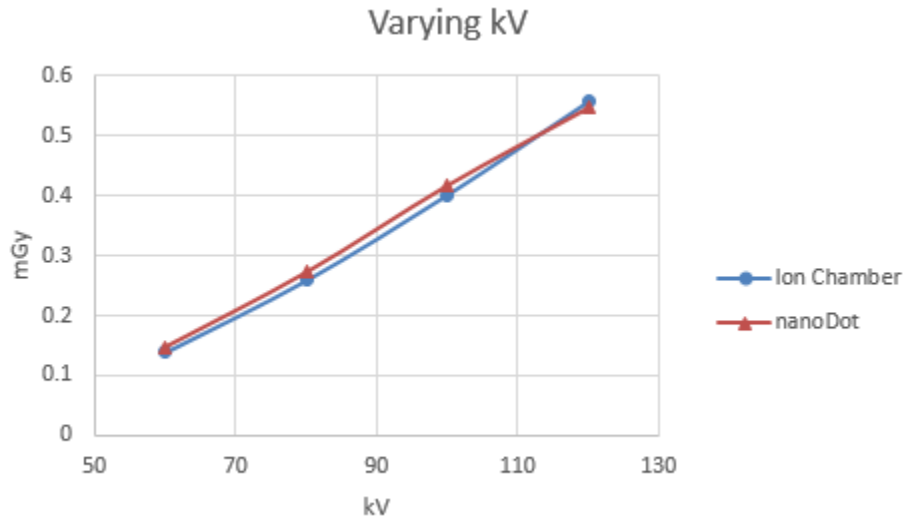
Figure 3-8: comparison of dose measurements using constant mAs and varying kV.

Varying the filtration of the x-ray beam can shift the beam spectrum and also affect the response of certain detectors. Therefore, measurements were made comparing the nanoDots to the ion chamber using a constant kV and mAs with a changing amount of filtration. Table 3-4 lists the various filter combinations available on the radiographic unit, along with the subsequent dose readings for the ion chamber and the nanoDots.

35

Table 3-4 Comparison of ion chamber and nanoDot response with changing filtration

Filter number	Filter Combination	Dose ion chamber (mGy)	Dose nanoDot (mGy)
1	No added filtration	0.65	0.68
2	0.1mmCu + 1mmAl	0.29	0.29
3	0.2mmCu + 1mmAl	0.2	0.2
4	2mmAl	0.4	0.42
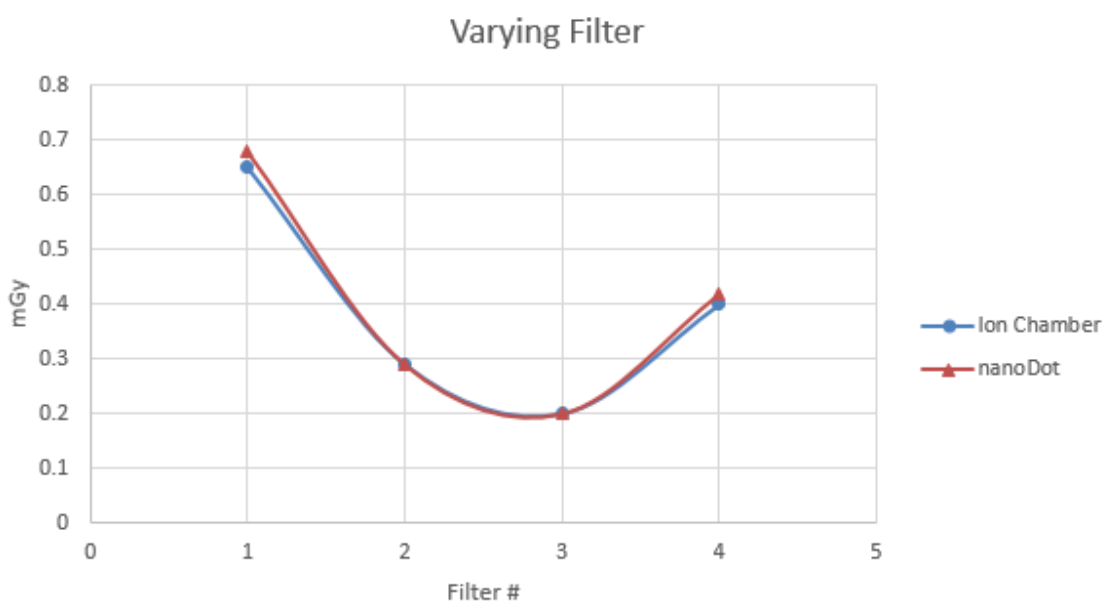
Figure 3-9 comparison of ion chamber and nanoDot response with changing filtration

In order to test the inter-variability of the nanoDots themselves, all nanoDots were placed on a radiology light box for clearing. The radiology light box has an average luminance of 1848 cd/m^2, and all nanoDots were placed uniformly on the illuminated surface for approximately 48 hours. 35 nanoDots were randomly chosen and placed in the marked containers. An initial "zero" reading was taken of

36

the 35 nanoDots on the microSTAR ii system. The setup for the exposures was the same as in figure 3-3 above. Each nanoDot was individually irradiated at 80kV, 4mAs large focal spot, 3 exposures, and returned to its respective container. On the Philips Digital Diagnost x-ray unit located at the UNM Outpatient Surgery and Imaging Services clinic, an exposure at 80 kV with 4 mAs using the large focal spot at the same distance the nanoDots are placed gives a dose reading of 0.273 mGy.

The nanoDots were stored for 18 hours in a locked file cabinet before final readout. Although it is considered good practice that the nanoDots be read out within 4 hours of exposure, the manufacturer allows for much later readout given that they are stored in a location where they will not be exposed to bright light, sunlight or additional radiation [51]. After 18 hours, the nanoDots were read out 4 times and converted to mrad dose as per usual with the microSTAR ii system. The initial readings from pre-irradiation were subtracted and the results were then divided by 3 (due to the 3 exposures). The final corrected readings, converted to mGy, are given in table 3-5.

www.manaraa.com

Table 3-5: nanoDot variance readings.

nanoDot	Pre-exposure reading (mrad)	18 hours Post-exposure read (mrad)	Corrected reading (mrad)	mGy
1	0.788	87.48	28.90	0.289
2	0.806	82.58	27.26	0.273
3	0.699	85.52	28.27	0.283
4	0.691	85.92	28.41	0.284
5	0.797	82.90	27.37	0.274
6	0.771	82.81	27.35	0.273
7	0.788	80.84	26.68	0.267
8	1.061	83.70	27.55	0.275
9	1.497	91.80	30.10	0.301
10	1.366	83.92	27.52	0.275
11	0.466	85.17	28.24	0.282
12	0.911	82.55	27.21	0.272
13	0.835	85.17	28.11	0.281
14	0.825	86.18	28.45	0.285
15	0.825	91.25	30.14	0.301
16	0.921	86.27	28.45	0.284
17	0.683	82.78	27.37	0.274
18	0.716	84.94	28.07	0.281
19	0.683	86.43	28.58	0.286
20	0.806	84.54	27.91	0.279
21	0.779	87.62	28.95	0.289
22	0.707	84.41	27.90	0.279
23	0.932	84.47	27.85	0.278
24	0.691	84.77	28.03	0.280
25	0.683	83.47	27.59	0.276
26	0.707	85.23	28.18	0.282
27	0.676	84.44	27.92	0.279
28	0.788	83.43	27.55	0.275
29	0.966	92.60	30.54	0.305
30	0.576	87.54	28.99	0.290
31	0.699	84.13	27.81	0.278
32	0.583	85.29	28.24	0.282
33	0.699	85.99	28.43	0.284
34	0.461	81.20	26.91	0.269
35	0.724	84.63	27.97	0.280

38

The coefficient of variation for the nanoDots was approximately 3.01%, and the accuracy of the average dose was 3.02%, which is in agreement with manufacturer specifications and results found in the literature of the nanoDots having a dose accuracy within 5% [49], [54].

3.2 Polystyrene block testing

The purpose of this experiment was to obtain data for comparison to the Monte Carlo simulation performed in GATE. Therefore, five nanoDots were used at each measuring point (entrance, midline, and exit) and their readings were then averaged in order to simplify any influence due to heel effect or other beam anomalies.

For this test, a stack of uniform polystyrene blocks were used along with the previously calibrated nanoDots. The individual blocks are 25.5 cm x 25.5 cm square of various thicknesses. The polystyrene blocks were stacked 20.8 cm high directly on the digital detector of the GE Optima radiographic unit. The x-ray tube was placed at 100 cm source-to image-distance (SID). X-ray field size was adjusted to 32 cm x 32 cm at detector face. A total of fifteen nanoDots were placed on the phantom, 5 at the entrance, 5 midline at 10.4 cm and 5 at the exit of the polystyrene stack. See figure 3-10 for phantom setup and position of the nanoDots. The nanoDots were placed as close to in-line with each other at each depth as possible. 4.5 mm copper BB's were placed at the entrance side of the phantom near the nanoDots for later identification in the x-ray images.

www.manaraa.com
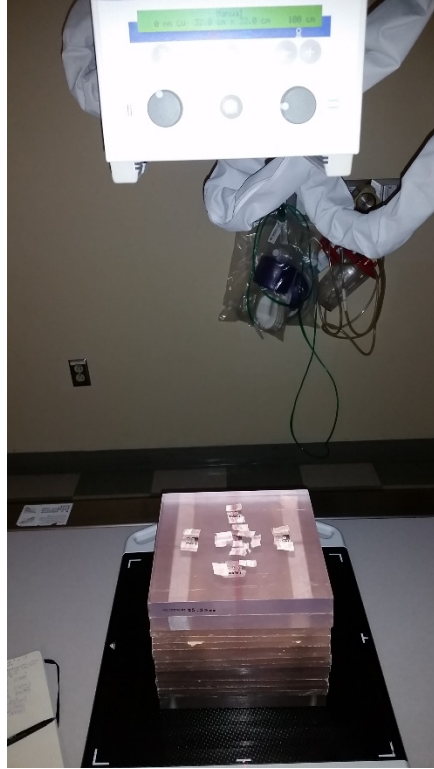
Figure 3-10: Polystyrene phantom setup with nanoDot dosimeter placement.

Three exposures were made using 80 kV and 4 mAs. It was determined in the prior nanoDot calibration testing that performing three exposures on the nanoDots, and calculating the average dose, helped to ensure that enough radiation dose was detected in the nanoDot for a more accurate readout. As with all nanoDot measurements, an initial reading was performed on the nanoDots in order to correct the measured dose with any remnant reading still present on any of the nanoDots. This pre-reading was then subtracted from the final reading after the exposures were made. A similar setup was used in order to obtain dosimetry readings for a lateral radiograph on the same polystyrene phantom, see figure 3-11. Five nanoDots were used at the lateral entrance and exit of the polystyrene

40

phantom. Due to the geometry setup, and the fact that the polystyrene blocks would now be parallel to the x-ray beam, only one nanoDot was placed at midline in the phantom.
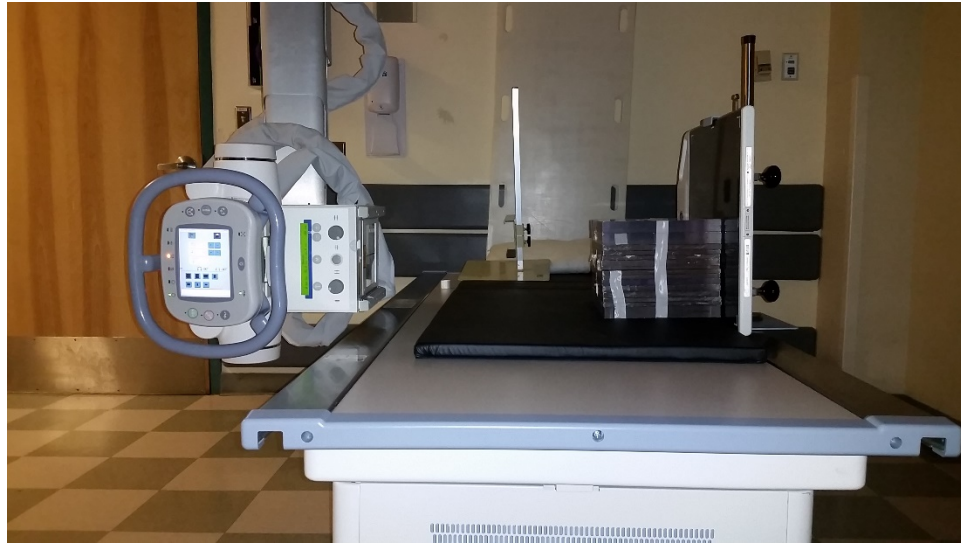
Figure 3-11: Lateral setup for nanoDot measurement on polystyrene phantom.

Again, the system was setup for a 100 cm SID, and 3 exposures were made at 80kV and 4mAs. 4.5 mm copper BB's were placed on the entrance side only to help with location of the nanoDots on the radiographs. One additional copper BB was placed on the "head" side of the polystyrene phantom entrance in order to help with position location since the uniformity of the phantom created some initial confusion with placement in the images.

Table 3-6: Dose readings from nanoDots taken at 80kV and 4mAs using polystyrene block phantom for Lateral and AP projections.

Position	Lateral Average Dose (mGy)	AP Average Dose (mGy)
Entrance	0.539	0.506
Midline	0.177	0.162
Exit	0.022	0.027

Since the phantom setup was essentially a uniform cube, it is not surprising that the dose readout for the AP and lateral radiographs were nearly identical. Any difference in readout from the exposures is most likely due to small variations in the placement of the dosimeters since the lateral side of the phantom was not completely flat, as can be seen above in figure 3-11. Of particular interest was the midline dose from both the AP and lateral exposures. For the AP exposure, the midline nanoDots were placed perpendicular to the beam axis, whereas in the lateral setup, the midline nanoDot was placed parallel to the beam axis.

This setup change could not be avoided since the nanoDots were placed within the stack of polystyrene blocks. If the polystyrene blocks were rotated to allow for the nanoDots to be place perpendicular to the beam axis, then there would have been no change in the AP and lateral exposure tests. Having the nanoDots placed parallel to the beam axis in the for the lateral test presents the "worst case scenario" as described by Okazaki et al. where the greatest effect of angle on was seen at 90 and 270 degrees [47]. With an 8.8% difference between

42

these two measurements, these results agree with those found in the literature, however, to minimize the effect of the exposure angle on the any readings, care will be taken to place the nanoDots at angles as close to 0 degrees as possible [47], [49], [51], [55].

3.3 Super-Flex Bolus Depth dose

Depth dose measurements allow the physicists to know how the x-ray beam will attenuate and change as it travels through the medium. As stated previously, all radiographic equipment tends to vary slightly even within the same manufacturer and model. Therefore, when considering dosimetry from radiographic units, it is necessary to determine how the individual x-ray beam will interact with tissue. Medical physicists routinely determine dose deposition as a function of depth using either a water tank or solid phantom to perform depth dose measurements [27], [56], [57].

For this project, there was a need to perform measurements and calculations on a range of patient (or phantom) sizes. One way to utilize the current standard-man-size anthropomorphic phantom for multiple measurements and calculations is to increase the body habitus by using Super-Flex. Super-Flex Bolus (Action Products Inc., Hagerstown, MD) is a flexible soft tissue and water equivalent material commonly used in radiation therapy applications [58]. With its density of 1.03 g/cm^3 Super-flex is also an ideal material to use for diagnostic x-ray imaging when a tissue equivalent material compensator is needed, with the range of human soft tissue densities being 0.95g/cm^3 (adipose ICRU-44) – 1.06

43

g/cm^3 (soft tissue ICRU-44) [59]. Using Super-Flex the patient size could be modified using a single phantom.

Before using the Super-Flex in conjunction with the anthropomorphic phantom, it was necessary to determine the response and accuracy of the nanoDots at depth in "tissue". This would ensure that the response of the nanoDots with tissue phantom would be consistent to the results observed during the tests with polystyrene blocks. This experiment was performed by placing nine nanoDots at various depths within a 12 cm stack of 1 cm pieces of Super-flex. The nanoDots were arranged at 0 cm (surface), 5 cm, and 10 cm depths, placed 4 cm apart, as shown in figure 3-12.

The configuration of the nanoDots was chosen as such to obtain depth dose data both perpendicular and parallel to the tube axis. This technique will compare the off-axis depth doses ensure that the variations in x-ray beam intensity due to heal effect are adequately determined and can be accounted for in later experiments and calculations as necessary. Off-axis in this case referring to the placement of dosimeters at positions other than just on the central axis, or beam center, of the phantom.
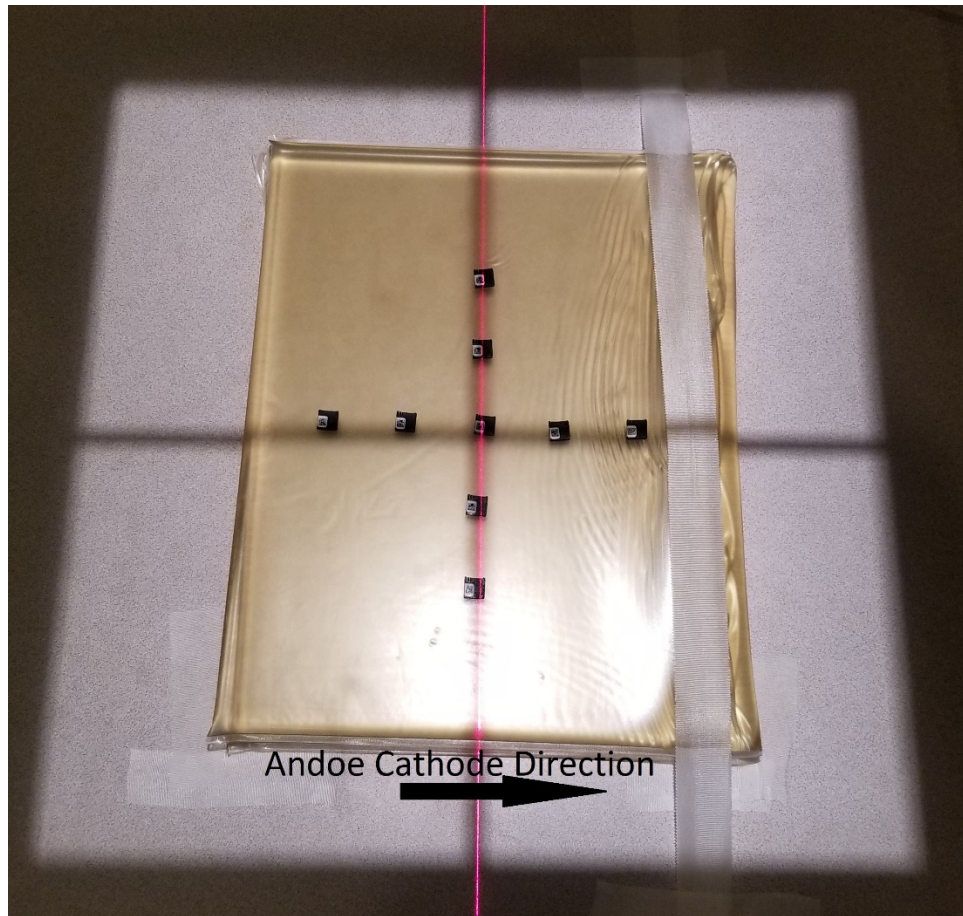
Figure 3-12: Placement of nanoDots on Super-flex phantom. nanoDots were placed parallel and perpendicular to tube axis at the surface, 5cm, and 10cm depth. This figure shows the nanoDots placed at what will be 10cm depth, with subsequent layers of Super-flex to be placed on top.

The positions of the nanoDots are labeled as in figure 3-13.
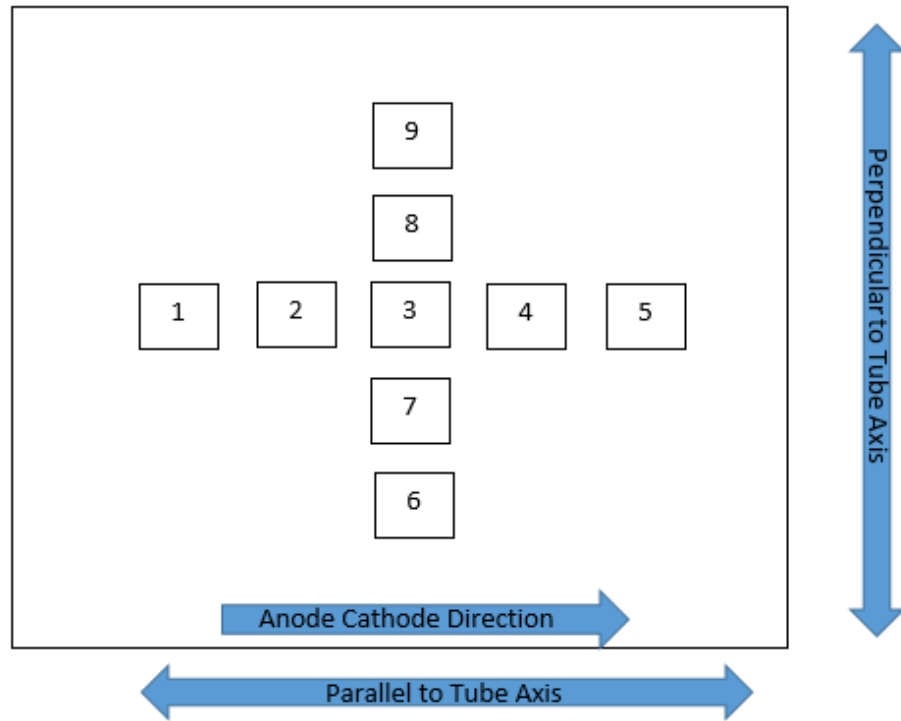
Figure 3-13: Layout of nanoDots for off-axis depth dose measurement, with 1 being on the anode side of the tube and 5 being on the cathode side.

The Super-flex stack was placed directly on the table top, with the imaging detector in the holder underneath the table. Exposures were made at 80, 100, and 125 kV and 12.5 mAs.

Figures 3-14 – 3-16 show the depth dose data collected for 80 kV, 100 kV and 125 kV energies.
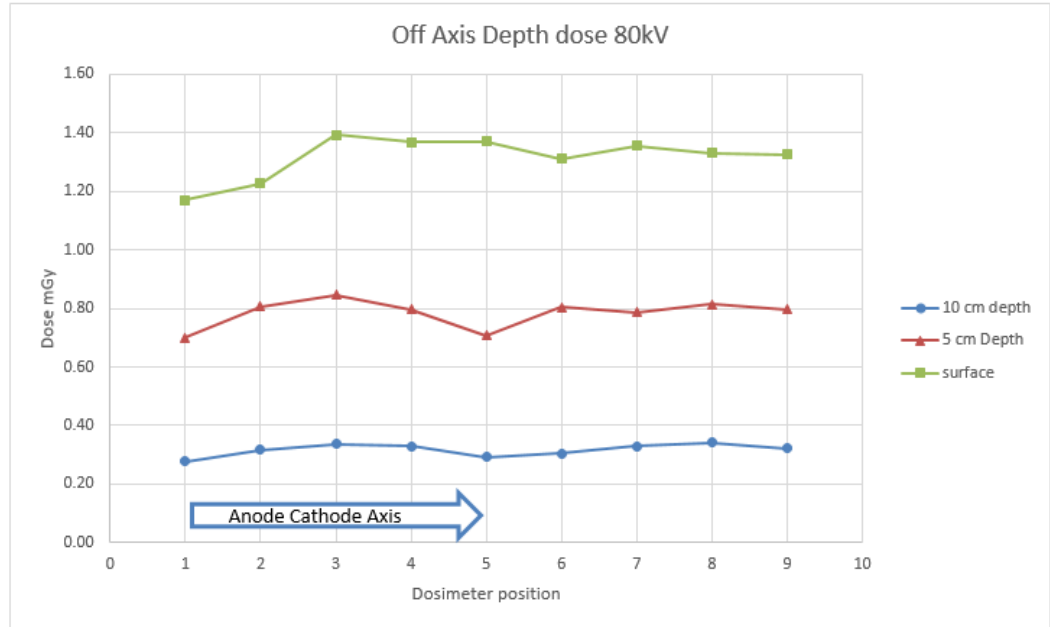
Figure 3-14: off axis depth dose data for 80 kV. Anode Cathode axis is in the direction from position 1 – 5.
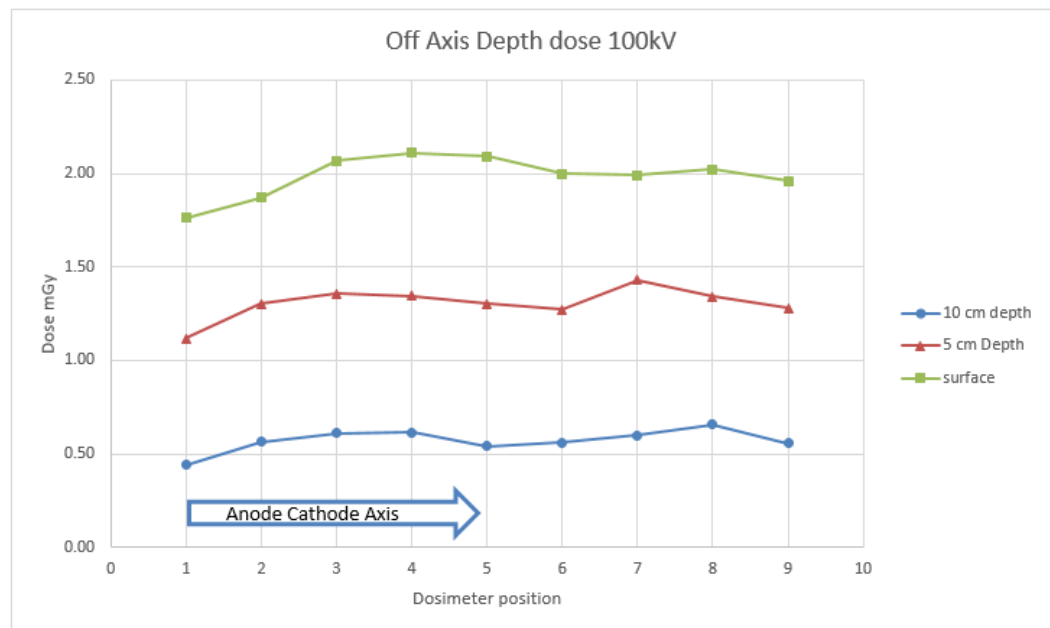
Figure 3-15: off axis depth dose data for 100 kV. Anode Cathode axis is in the direction from position 1 – 5.

47
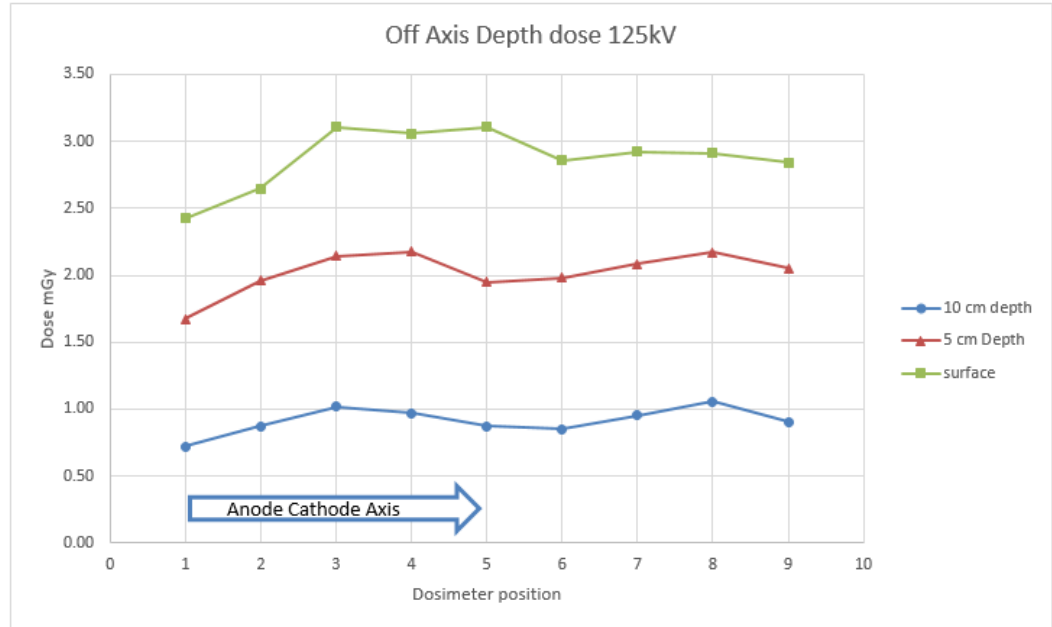
Figure 3-16: off axis depth dose for 125 kV. Anode Cathode axis is in the direction from position 1 – 5.

These graphs of the off axis depth dose show the slight heel effect as expected in the anode – cathode direction, as well as a relatively flat response in the direction perpendicular to the tube axis, at depth for each of the energies.

48

4 Monte Carlo testing and validation

1. Programming and testing of Monte Carlo program to use for data validation and algorithm development.

2. Monte Carlo modeling

    a. Using the AK reference point data, the beam characteristic data, and CT image data sets to perform Monte Carlo simulations.

    b. Use GATE to perform simulations using the CT images and projection radiography data collected on the anthropomorphic and planar phantoms. GATE is an open-source software developed using the Geant4 Monte Carlo code dedicated to numerical simulations in medical imaging and radiotherapy [60].

Monte Carlo simulations have become an essential tool in the design, optimization and dosimetry in medical physics [60]. Various Monte Carlo calculation methods have been in use for solving radiation transport problems with some being developed to simulate photon-electron transport through matter at energy ranges suitable for medical physics applications [61]. For this project MCNPX [62], PENELOPE [63], and GEANT4 [64] were considered since they have been used in diagnostic medical physics applications.

The need was for a Monte Carlo code that would be fairly straightforward to use and able to utilize an imported CT scan data set as a voxelized phantom. MCNPX is a very powerful and infinitely customizable program. However, the programming associated with this code is cumbersome and not entirely utilizable for diagnostic imaging applications.

49

A course entitled "Monte Carlo simulation of x-ray imaging and dosimetry" held by the European Training and Education for Medical Physics Experts in Radiology (EUTEMPE-RX) was offered on the use of PENELOPE. This course was an advanced-introductory course on PENELOPE its theory and uses. PENELOPE is an excellent Monte Carlo code, highly customizable and fairly straightforward to use. Unfortunately, there is no readily available way to import CT data sets into the PENELOPE code.

Lastly, there is the Monte Carlo code GATE (http://www.opengatecollaboration.org/#). Programming the code in GATE is similar to that of PENELOPE, which allowed the utilization of the knowledge gained at the EUTEMPE-RX course towards the self-start guide for the program. Additionally, there is a fairly straightforward method to import CT DICOM data sets into GATE. After a review of the associated literature, and determining it to be a tested and approved code for medical physics applications GATE was chosen as the Monte Carlo code to use for this project. One of the main benefits to using GATE is the ability of the user to import a DICOM CT image dataset by converting it to an .mhd file using readily available open source image tool kits such as ImageJ [65] and VV image viewer [66].

4.1 Monte Carlo code

GATE 7.2 was installed in a 64-bit Ubuntu Linux operating system. The Ubuntu operating system was created in an Oracle virtual machine environment run on a 64-bit Windows 10 operating system. The Windows 10 operating system

50

was installed on an Intel ® Core ™ i5-5300U CPU system with 4 processing cores and 8.00GB of RAM. The Virtual machine was allotted 2 of the processing cores and 5.00 GB of RAM.

The main components of the GATE input file are similar to other Monte Carlo simulation programs in that the user is able to define all aspects of the simulation, including the radiation source, target, world, and which interactions are allowed. GATE provides a macro known as the "DoseActor" which stores the absorbed dose from the simulation in a 3D matrix of the programmers choosing. The DoseActor can be customized in size and position and attached to any phantom within the simulation, and allows for the collection of deposited energy (MeV), absorbed Dose (Gy), the number of hits, and the local statistical uncertainty [67]. In order to cut down on the simulation time, the DoseActor was modified with the proven track length estimator (TLE) method available in GATE [67]–[69].

4.2 Accuracy test of Monte Carlo code

In order to test the accuracy of the GATE Monte Carlo software it was necessary to perform a simulation that could be readily compared to a manual calculation with a known and accepted value. Given a known problem with a reference table answer and comparing it to the GATE simulation result will validate the basic functioning of the Monte Carlo code [60]. The problem chosen for this test was based on one of the examples found in the text book "The Physics of Radiology" [42] as follows: "Calculate the exposure per dose for an 80 keV mono-energetic x-ray point source to a point in air".

The solution to this problem relies on the relation between the energy fluence,Ψ, through an area and the exposure X at a point P in the center of the area. The energy absorbed by a small mass of air at point P is

$$\Psi \left(\frac{\mu_{ab}}{\rho}\right)_{air}$$

4-1

Since

$$1\ Roengten = 0.00873\ \frac{J}{kg_{air}} = \left(0.00873\ \frac{J}{kg}R\right)X$$

4-2

Then the energy fluence per Roentgen is

$$\frac{\Psi}{X} = 0.00873\ \frac{J}{\left(\frac{\mu_{ab}}{\rho}\right)_{air}}\ kgR$$

4-3

For

$$hv = 80\ keV = 0.08\ MeV$$

4-4

and

$$\left(\frac{\mu_{ab}}{\rho}\right)_{air} = 0.0236\ \frac{cm^2}{g} = 0.00236\ \frac{m^2}{kg}$$

4-5

52

the energy fluence is then

$$\frac{\Psi}{X} = \frac{0.00873J}{0.00236\left(\frac{m^2}{kg}\right)kgR} = 3.6992\frac{J}{m^2R}$$

4-6

Photon fluence is then

$$\frac{\Phi}{X} = \frac{\frac{\Psi}{X}}{h\upsilon}$$

4-7

and

$$h\upsilon = 80\ keV = 1.2816 \times 10^{-14}J$$

4-8

Therefore

$$\frac{\Phi}{X} = \frac{3.6992J}{1.2816 \times 10^{-14}Jm^2R} = 2.886 \times 10^{14}\frac{photons}{m^2R}$$

4-9

The solution is, one needs to have an energy fluence of $3.6992\frac{J}{m^2}$ for 80 keV photons of photon fluence $2.886 \times 10^{14}\frac{photons}{m^2}$ to register an exposure of 1 Roentgen at a point, P, in space.

For the GATE simulation, a point source of 80 keV photons was placed at a distance of 1 meter from the origin. A 1m x 1m x 1cm rectangular prism (slab) made of dry air was centered at the origin, see figure 4-1.
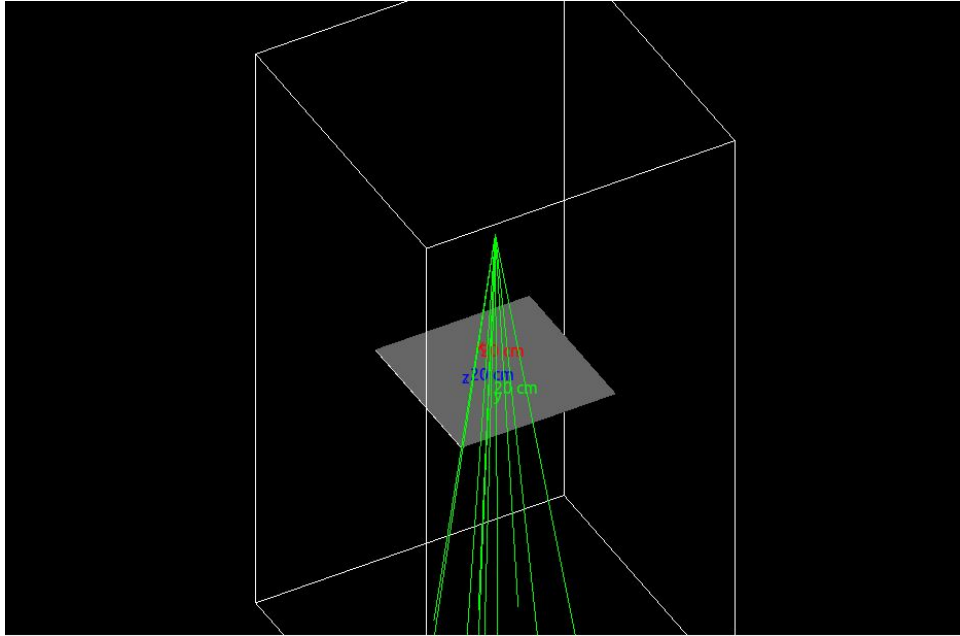
Figure 4-1 GATE simulation depicting air slab with point source of 80keV photons
depicted as green lines.

In order to compare the calculation to the results of the simulation, the total photon fluence at the air slab would need to be simulated. This would entail performing the GATE simulation for 2.886×10^{14} photons. This amount of histories would obviously be time prohibitive and not possible on readily available current computer systems. Therefore, as is common practice in Monte Carlo simulations, a smaller number of histories was performed with a factor applied to make up for the total number of photons required.

10 million histories were simulated and the total dose deposited in the air slab was tallied. The simulation was performed three different times and an average dose deposited to the $1m^2$ air slab was 3.07×10^{-10} Gy, with an uncertainty of 0.026. For 1×10^7 histories, this gives a dose per photon of $3.07 \times 10^{-17} \frac{Gy}{photon}$ in

54

the simulation. With a photon fluence of 2.89x10^{14} $\frac{photons}{m^2 R}$, the total dose deposited in the slab can be calculated as follows:

$$\left(3.07 \times 10^{-17} \frac{Gy}{photon}\right) \times \left(2.89 \times 10^{14} \frac{Photons}{m^2 R}\right) \times 1m^2 = 0.00886 \frac{Gy}{R} \qquad \text{4-10}$$

Per definition, one Roentgen of air kerma deposits 0.00877 Gy in dry air. The percent difference between this simulation using the GATE code and the known quantity of Roentgen to gray conversion, was 1.02%.

In addition to this problem, the examples available to all GATE users via the OpenGATE collaboration website were completed and compared to the results given by others. These additional examples will not be covered here, but they serve as a starting point for GATE users to ensure their code is working correctly.

4.3 Super-flex phantom depth dose measurements

In order to ensure the GATE Monte Carlo code would give similar results as real world measurements, it was necessary to recreate the depth dose experiment (see chapter 3) in silico. With the nanoDot measurements as reference, and the physical properties of the Super-Flex well known, the following two experiments were performed for validation of the GATE Monte Carlo code using a planar homogeneous phantom setup.

The first experiment was to mock up the entire experiment in GATE by creating a geometric phantom with the same properties as the Super-flex. This was accomplished by creating a rectangular prism measuring 25 cm (width) x 30

55

cm (length) by 12 cm (height), and giving it the GATE material property of AT_AG_SI5_14, which has the same material make up and density of the Super-Flex. The source, in this case a point source, was placed at the same SID as used for the depth dose measurements in the clinic. The source itself posed an issue in completing this simulation. As with all diagnostic imaging equipment, the x-rays produced in the clinic are not monoenergetic, but rather, a spectrum of energies based on the peak energy set on the unit. The general spectrum is the filtered bremsstrahlung with characteristic peak energies for tungsten as shown in figure 4-2.
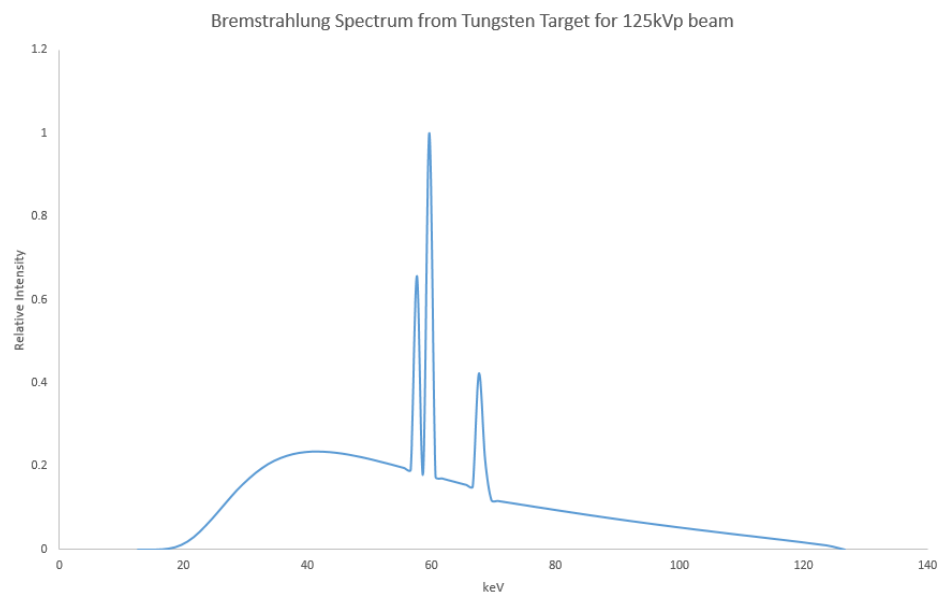
Figure 4-2: Filtered bremsstrahlung spectrum with characteristic radiation peaks for 125kVp beam

In order to incorporate the bremsstrahlung spectrum into the Monte Carlo calculation, the programmer must be able to generate a table that has energy bins and probability of those energies listed so that the program may produce photon

56

histories estimating the x-ray spectrum. Since there is still no practical way to measure the spectrum in the clinic [39], [61], [70], the spectrum must be generated via a third party program such as SpekCalc [71]. SpekCalc allows the user to generate a spectrum for any kVp based on certain details of the x-ray tube, such as anode angle and various filtration thicknesses.

Since all of the required information may not be available to the physicist to generate a spectrum in this way, it was necessary to develop a useful method to model the x-ray beam for future calculations. For this dissertation I chose to use the equivalent energy, or effective energy, of the x-ray tube for calculation purposes. The equivalent energy is a way to estimate the quality of a polyenergetic beam as though it were a monoenergetic beam [42], [45]. The procedure for determining the equivalent energy is as follows:

The half value layer of the x-ray beam was determined above to be 3.55mmAl. Therefore

$$HVL = \frac{0.693}{\mu} = 3.55 \ mmAl \ @ \ 80kV \qquad\qquad 4\text{-}11$$

Where μ is the linear attenuation coefficient of aluminum which is

$$\mu = \frac{0.693}{3.55 \ mm} = 0.1952 \ mm^{-1} \qquad\qquad 4\text{-}12$$

With the density of aluminum being

$$\rho_{Al} = 2.699 \frac{g}{cm^3} \qquad \text{4-13}$$

The mass attenuation coefficient for this 80kVp beam for aluminum is

$$\frac{\mu}{\rho_{Al}} = \frac{(0.1952 \, mm^{-1}) \times (10 \frac{mm}{cm})}{2.699 \frac{g}{cm^3}} = \frac{1.952 \, cm^{-1}}{2.699 \frac{g}{cm^3}} = 0.7232 \frac{cm^2}{g} \qquad \text{4-14}$$

We can then use table A-4e in Johns & Cunningham to see that this value falls between

$$30 \, keV : \frac{\mu}{\rho} = 1.101 \frac{g}{cm^2} \qquad \text{4-15}$$

and

$$40 \, keV : \frac{\mu}{\rho} = 0.5571 \frac{g}{cm^2} \qquad \text{4-16}$$

Using linear interpolation, the result is an equivalent energy of 36.945 keV for the 80kVp beam with a HVL of 3.55mmAl. Since the HVL can vary over time due to normal clinical use, the HVL will be measured before each experiment in the room and a new equivalent energy calculation performed for each Monte Carlo simulation as needed.

Now that an equivalent energy has been determined, it is necessary to determine if simulations performed with equivalent energy beams interact in a

58

similar manner as the associated spectrum in the Monte Carlo calculation. The geometric Super-flex phantom simulation was run with both polyenergetic beams at 80, 100, and 125kVp beams, and the monoenergetic equivalent for each 36.94, 39.51, and 44.39 keV respectively. Depth dose data was taken at 0, 2.5, 4.5, 5.5, 6.5, 8.5, 9.5, and 11.5 cm. The comparison of depth dose ratios are shown in the following graphs.
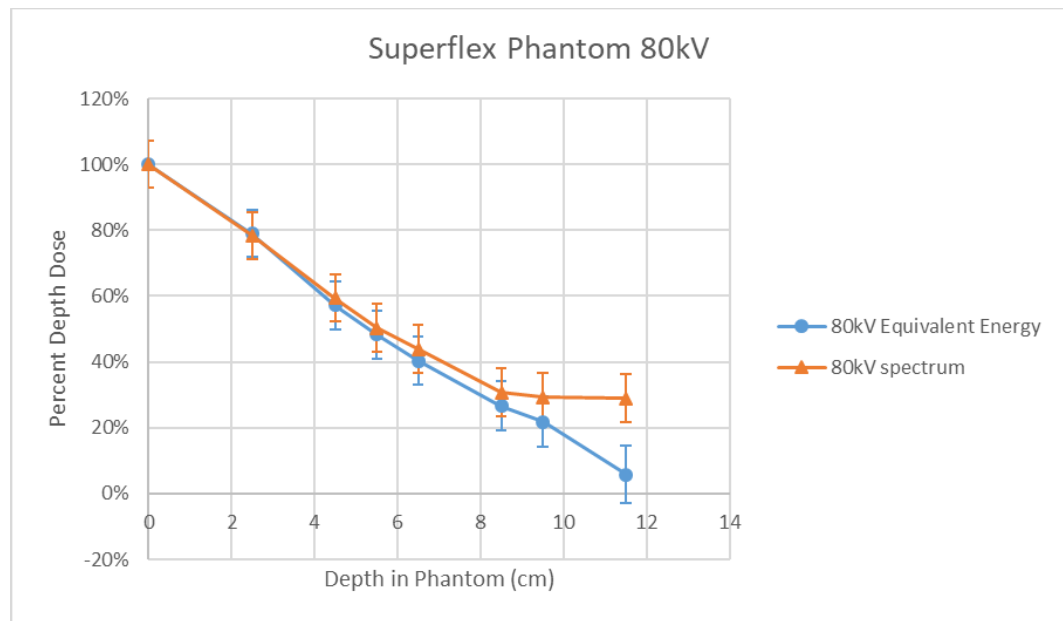
Figure 4-3: Monte Carlo depth dose comparison of spectrum and equivalent energy beam at 80kV.
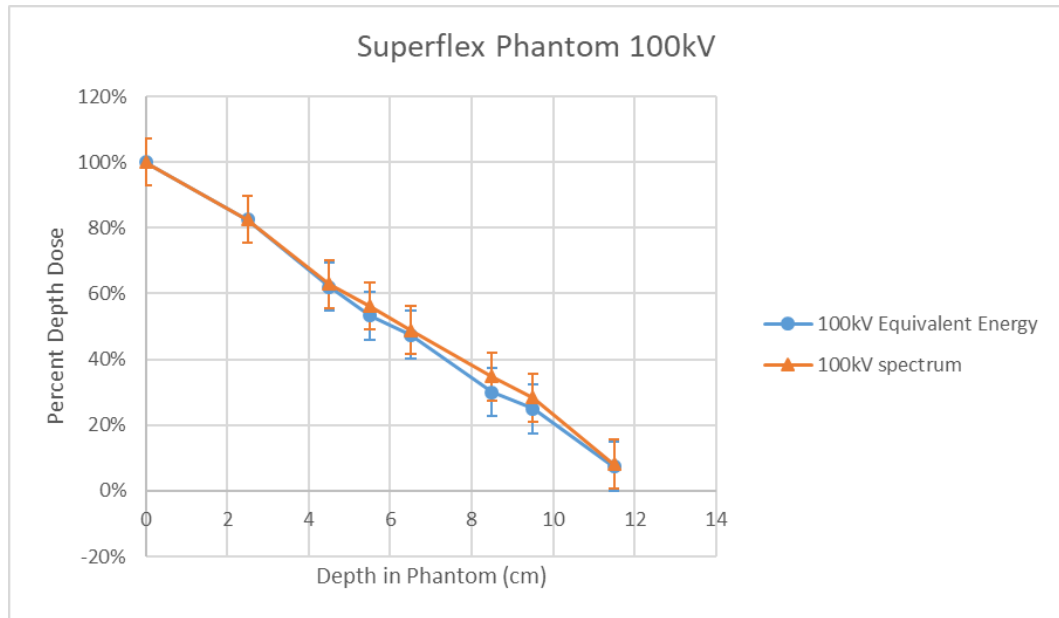
Figure 4-4: Monte Carlo depth dose comparison of spectrum and equivalent energy beam at 100kV.
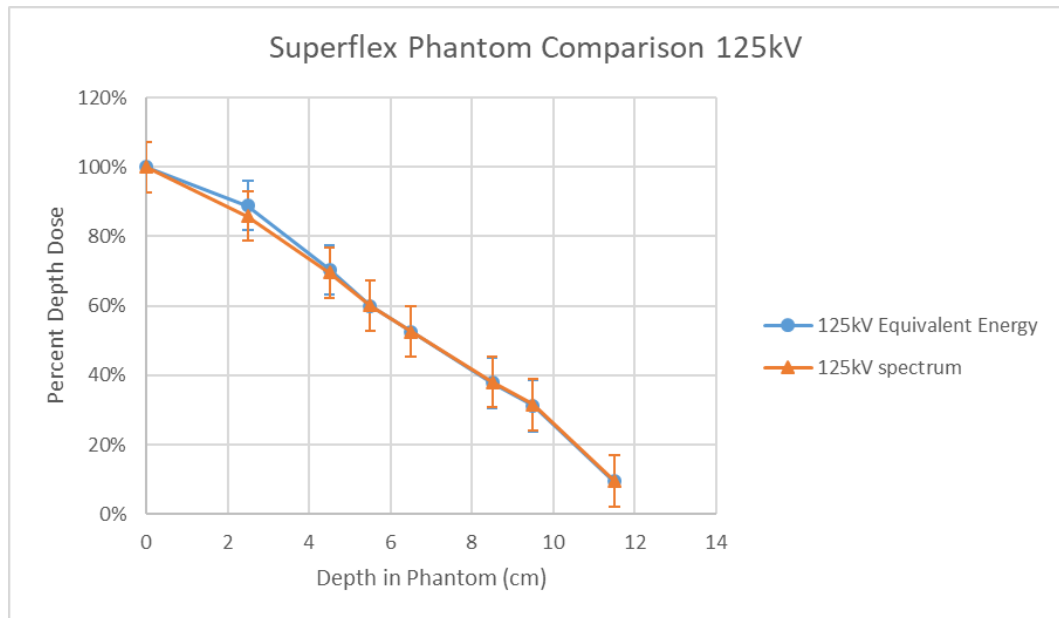
Figure 4-5: Monte Carlo depth dose comparison of spectrum and equivalent energy beam at 125kV.

As can be determined from figures 4-3 – 4-5 above, the equivalent energy simulation and the spectrum simulation are nearly identical for all energies. It is interesting to note the deviation observed with the 80kV spectrum at depth greater than 10 cm. Upon further review of the data generated by SpekCalc for the 80kV beam, it appears that SpekCalc may have had a rounding error at the high end of the energy spectrum that caused the simulation to have issues at depth. Additional spectrum generations for the 80kV beam gave similar results. Given this anomaly, the fact that the equivalent energy simulation gives nearly identical results, and the fact that less programming will be needed, thus cutting down on the simulation run time, all further Monte Carlo calculations for this project will use an equivalent energy beam for all sources, unless otherwise stated.

The second experiment was to compare the measured doses from the Super-Flex phantom to calculated doses from GATE simulation using imported CT scan images of the Super-Flex phantom. The purpose of this experiment was to ensure that the GATE Monte Carlo software was capable of producing results that match real-world measurements.

Rather than creating a geometric phantom within GATE for this experiment, CT images of the Super-Flex phantom were imported into the software using VV. VV allows utilization of actual subject images in GATE simulations by converting DICOM data into .mhd image files. DICOM CT images of the Super-Flex phantom discussed in chapter 2 were obtained on the Siemens Definition AS CT scanner located at the University of New Mexico Hospital in the advanced imaging suite.

61
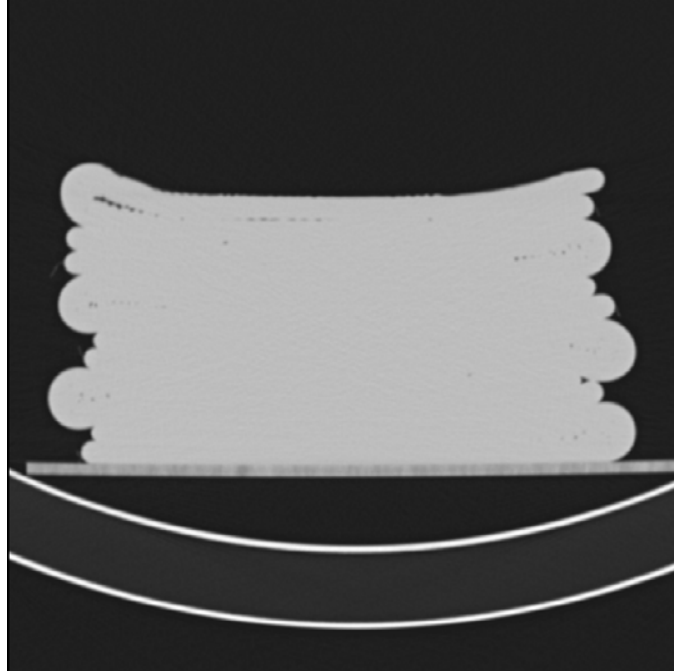
Figure 4-6: Axial CT image of Super-Flex phantom for use in GATE simulation.

The rest of the GATE simulation recreated lab conditions as accurately as possible. Equivalent energy monoenergetic x-rays were used in place of spectrum data, for reasons discussed previously. Depth dose data was collected by placing a calculation point voxel that encompasses the same volume as the nanoDot dosimeters, with dimensions 4.43x4.43x0.3 mm. GATE simulated data was then compared to measured data as depicted in the following graphs.

Super-Flex Phantom 80kV

Super-Flex Phantom 100kV
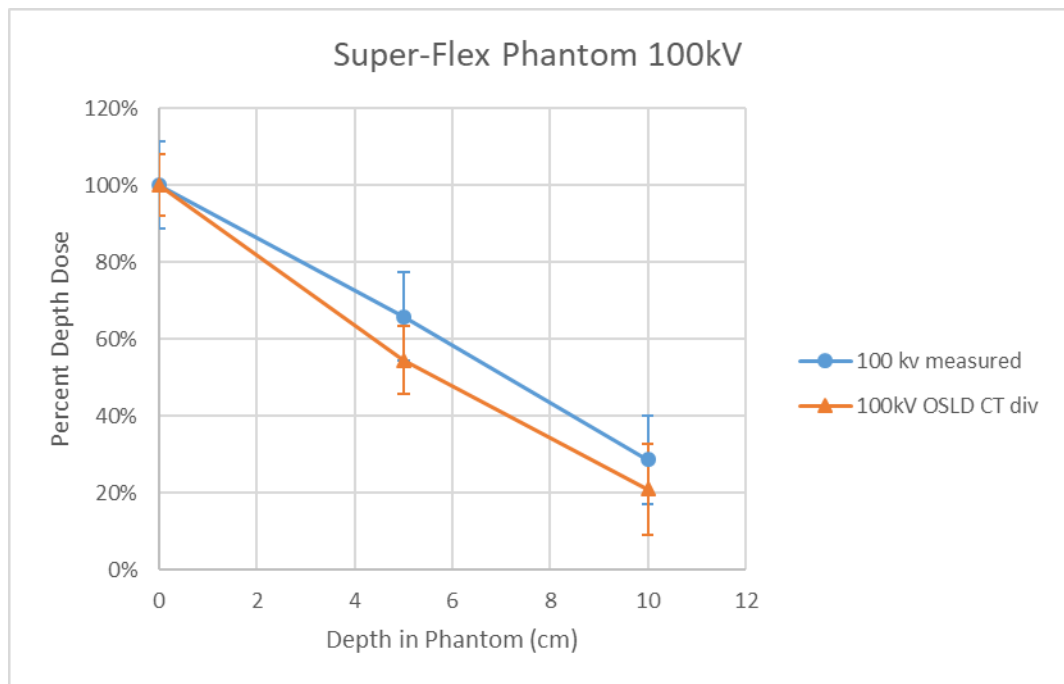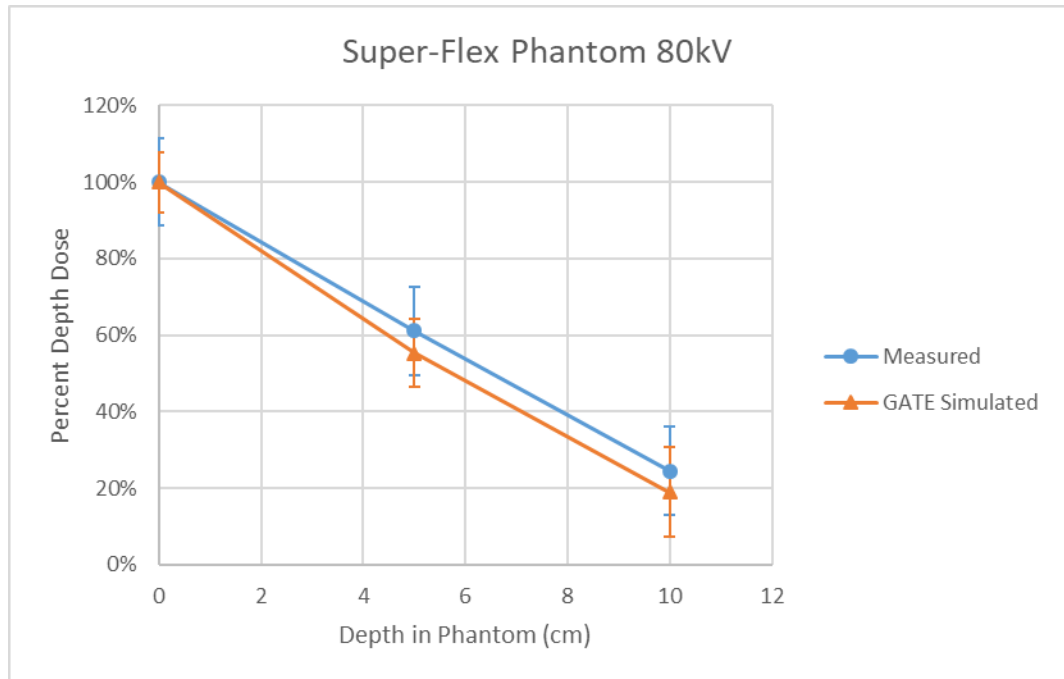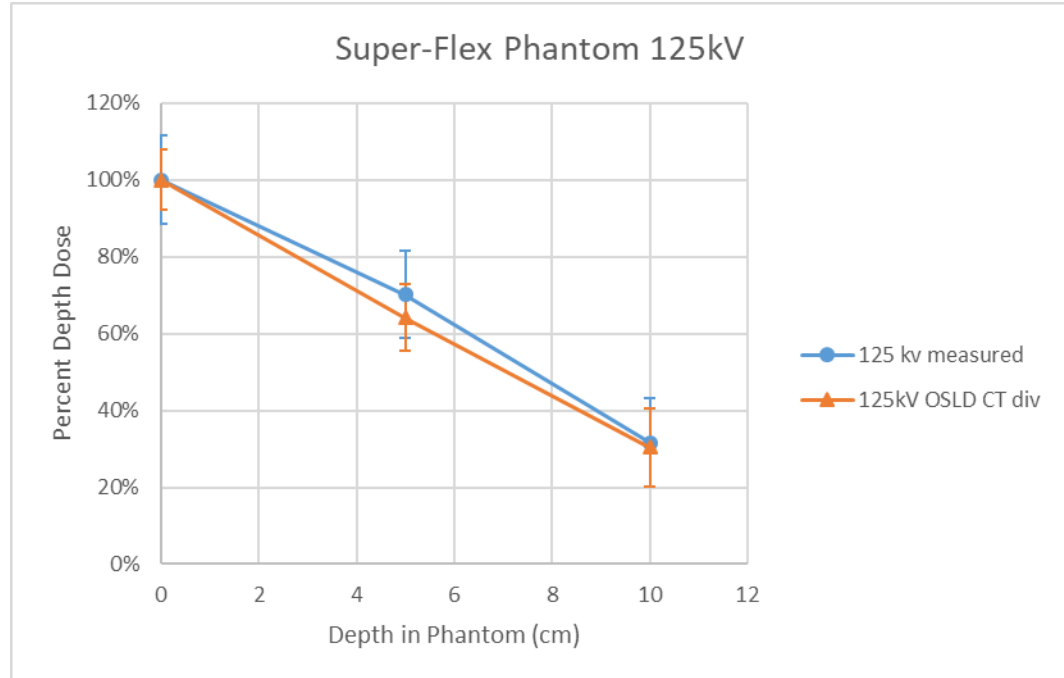
Figure 4-7 a-c: Depth dose comparison between measured and GATE simulation homogeneous Super-Flex phantom. Measured and simulated doses were normalized to maximum dose, which was at the surface of the phantom.

The agreement (all results within the average 12% uncertainty of the nanoDot measurements) between the GATE simulated depth dose data and the nanoDot measured data indicates that GATE will be a good surrogate for dose measurements in homogenous material.

4.4 Inhomogeneous planar phantom testing

After completing the depth dose measurements and simulations, it was necessary to determine if the Monte Carlo code would perform as accurately when faced with an inhomogeneous phantom. An inhomogeneous phantom was created by stacking polystyrene (density of 1.04 g/cm^3) and Styrofoam blocks (density of

64

0.05 g/cm^3) in a planar phantom. Two phantoms were created: A "large" and "small" inhomogeneous phantom of polystyrene and Styrofoam. The large phantom consisted of a total of 16 cm of Styrofoam blocks stacked between two 4 cm stacks of polystyrene with a total height of 24 cm. The "small" phantom consisted of 8 cm of Styrofoam blocks between two 8 cm stacks of polystyrene for a total height of 24 cm. See figure 4-8 for both phantoms.
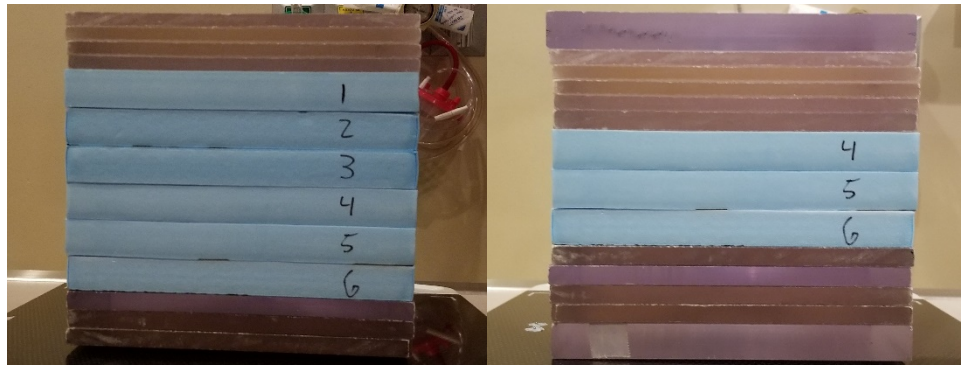
Figure 4-8: Inhomogeneous phantom setup. "Large" phantom on the left consists of 16 cm of Styrofoam (blue blocks) and 8 cm of polystyrene (clear blocks). "Small" phantom on the right consists of 8 cm of Styrofoam and 16 cm of polystyrene.

For both phantoms nanoDot dosimeters were placed at the entrance (top) to the phantom directly on the first set of polystyrene blocks, then at each Styrofoam surface interface, and finally at the exit (bottom). A total of nine nanoDot dosimeters were used for the large phantom, and 6 for the small phantom. This allowed for the collection of depth dose data in a non-homogeneous phantom. Dose data was collected for 80, 100, 120kV beams. Additionally, CT scans were

65

performed of each phantom and the subsequent images were imported into the GATE simulation.
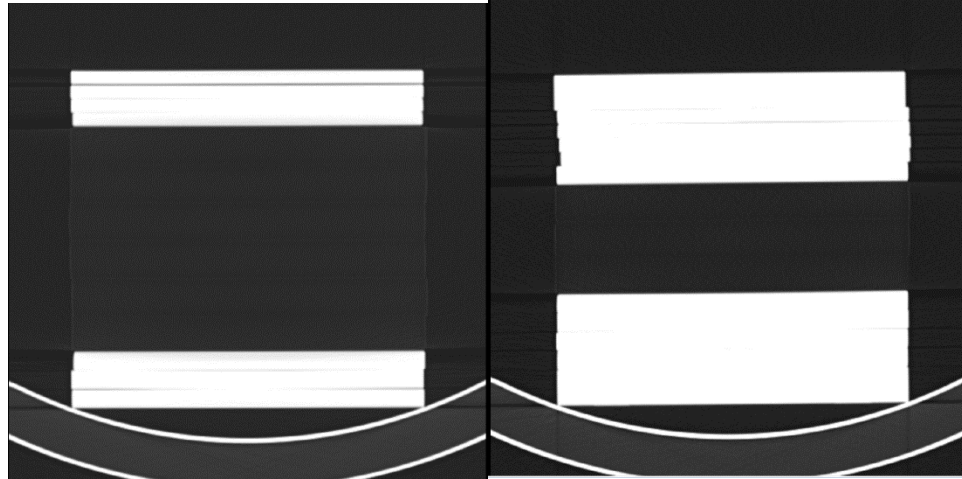
Figure 4-9: Axial CT images of "Large" (left) and "small" (Right) polystyrene and Styrofoam phantom. Large and small referring to the amount of Styrofoam present per phantom.

GATE simulations were run for each of the phantoms at each equivalent energy (36.56, 39.54, 43.51 keV respectively) at each measured depth. Comparison of depth dose data for each energy are shown below.

66

Large Inhomogeneous Phantom 80kV

Large Inhomogeneous Phantom 100kV

Large Inhomogeneous Phantom 120kV

Small Inhomogeneous Phantom 80kV
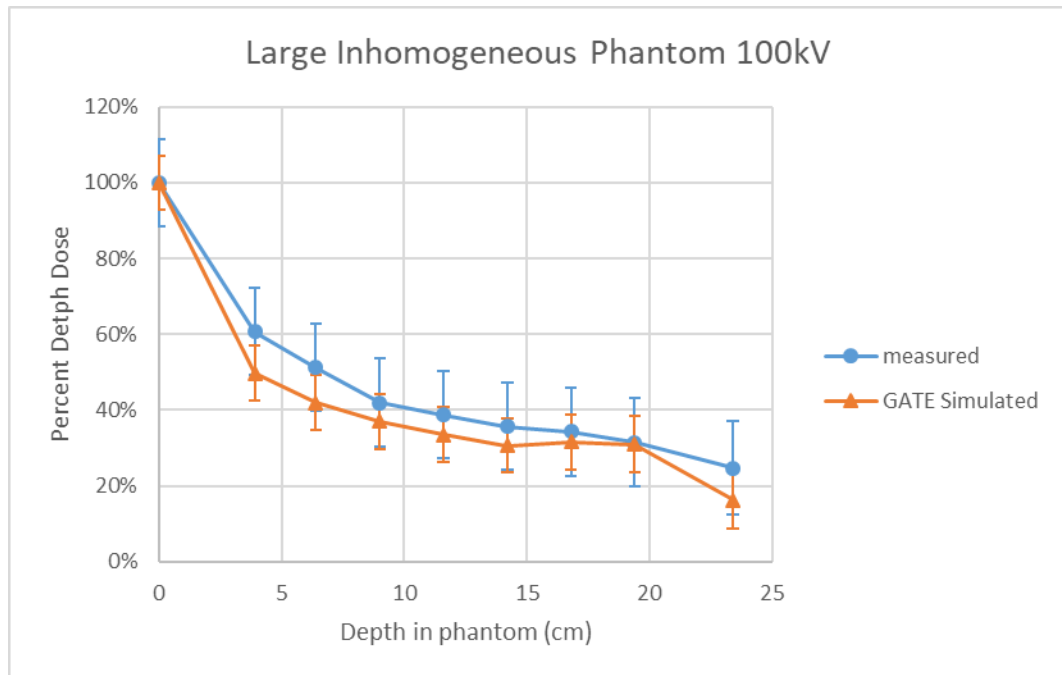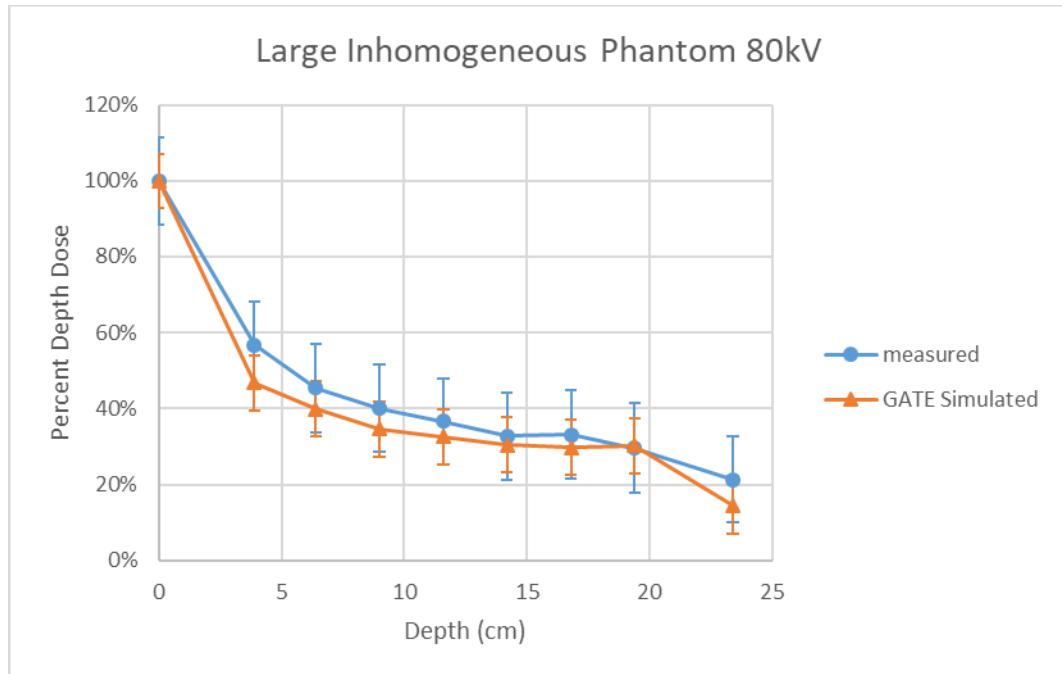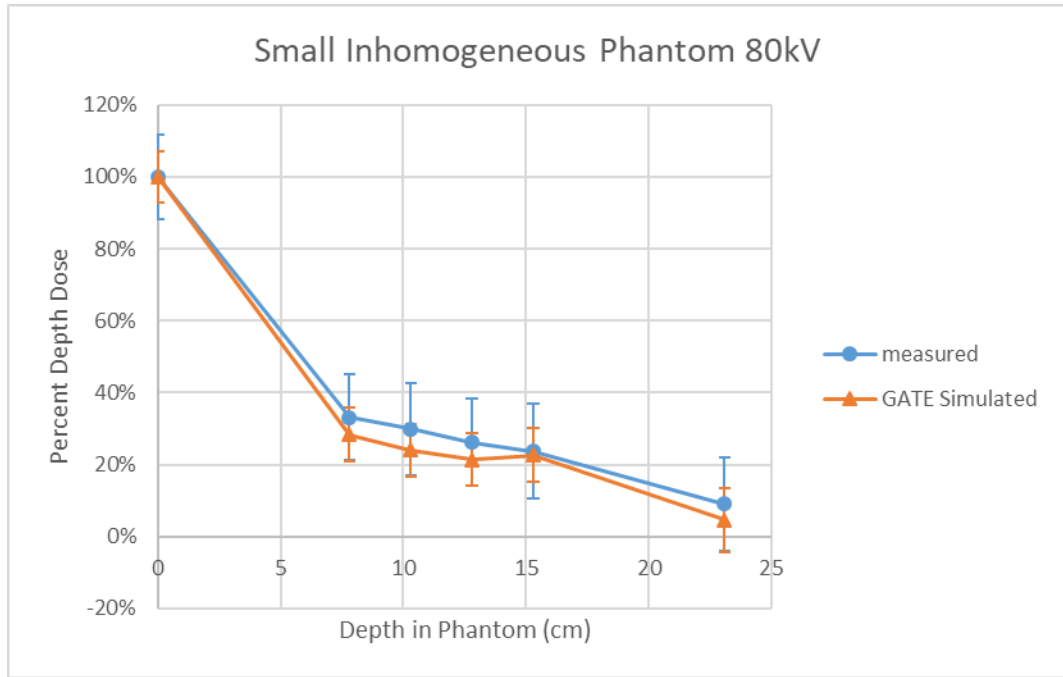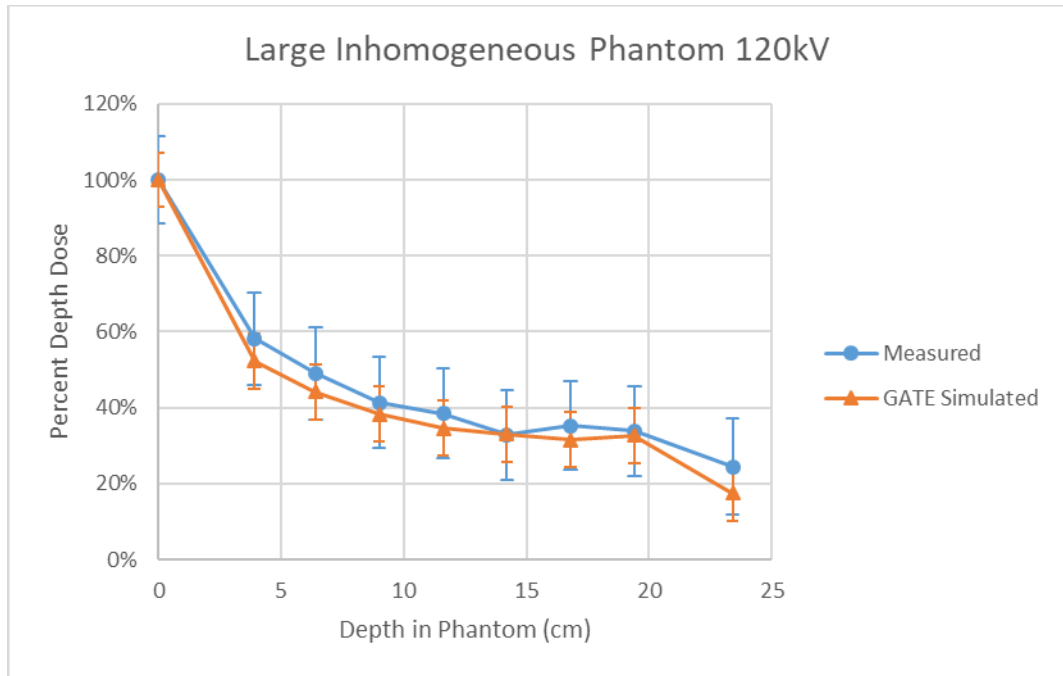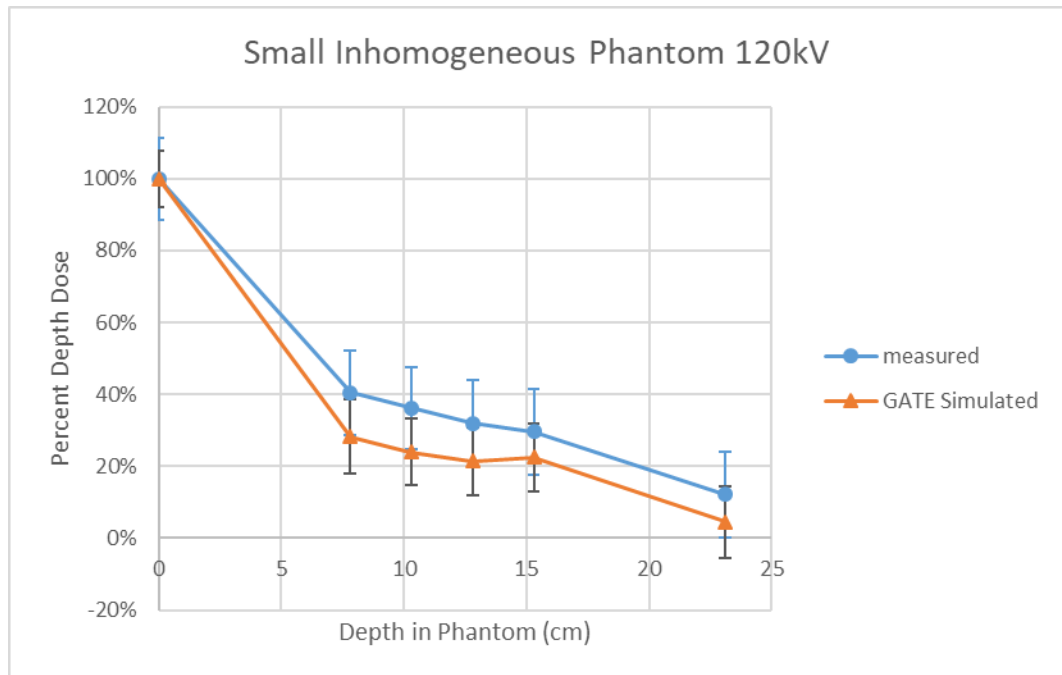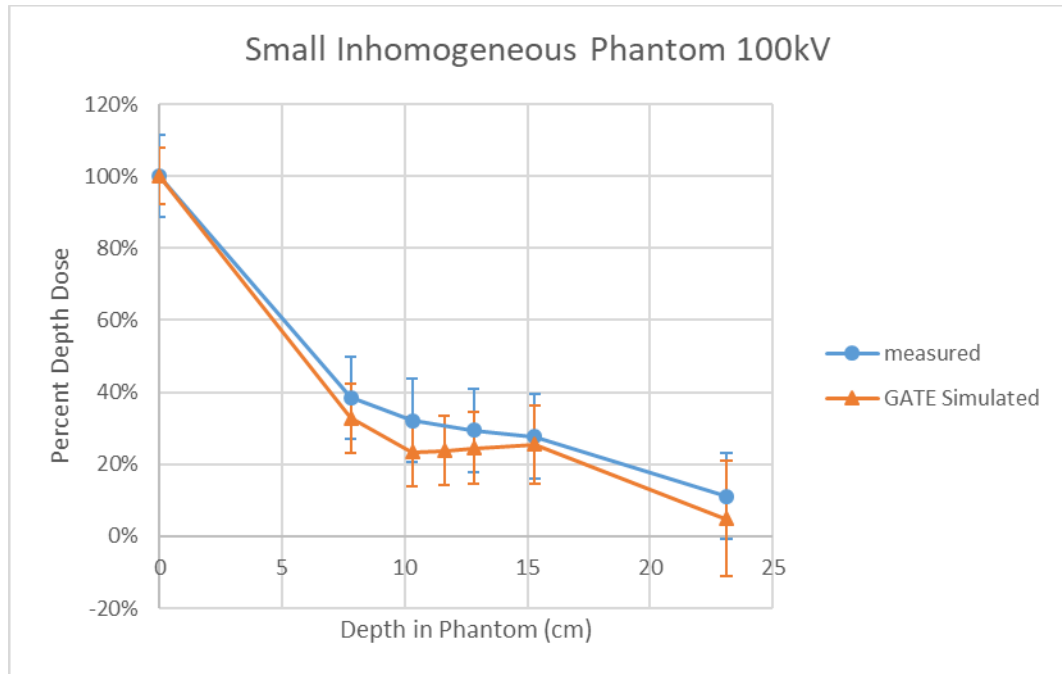
Figure 4-10a-f: Depth dose comparison between measured and GATE simulation in the Large and Small inhomogeneous phantom. Measured and simulated doses were normalized to max dose which was at the surface of the phantom.

69

Simulated versus measured doses show very good (all results within the average 12% uncertainty of the nanoDot measurements) agreement for this inhomogeneous phantom at each energy tested.

The next type of inhomogeneous planar phantom tested incorporated aluminum plates in addition to the Styrofoam and polystyrene blocks. Two phantoms were created using 1 mm aluminum plates. The first inhomogeneous phantom was created by stacking polystyrene and Styrofoam blocks in a planar phantom, with one of two 1 mm aluminum plates each located between the Styrofoam and polystyrene blocks. The second phantom was created by using the same setup as the first with the exception of removing all Styrofoam and replacing with polystyrene. See figure below for setup.

70
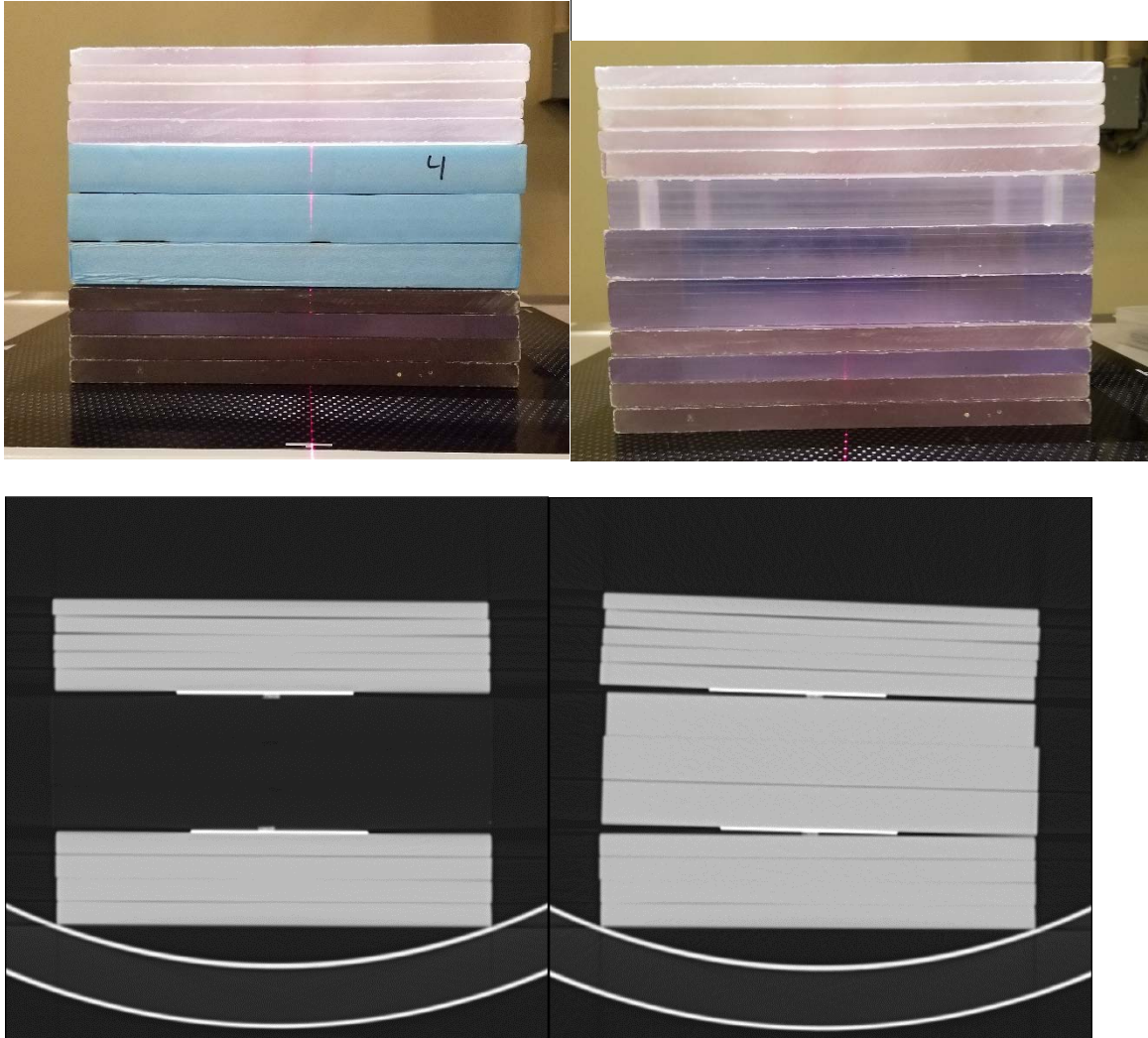
Figure 4-11: Inhomogeneous phantom incorporating aluminum plates with polystyrene and Styrofoam (left), or just polystyrene (right). Their associated CT scans are shown below the images respectively.

Dose measurements for both of these phantoms were taken at the entrance (top) of the polystyrene, after the first aluminum plate, before the second aluminum plate, and at the exit (bottom) of the phantom. See figure 4-11 for CT scans depicting the phantom setup. GATE simulations were run using at equivalent

المنارة للاستشارات   www.manaraa.com

energies for 80, 100 and 120kV as with the previous phantom. Graphs of the results are shown below.

Polystyrene Aluminum Styrofoam 80kV

Polystyrene Aluminum Styrofoam 100kV

Polystyrene Aluminum Styrofoam 120kV

Polystyrene & Aluminum Inhomogeneous 80kV
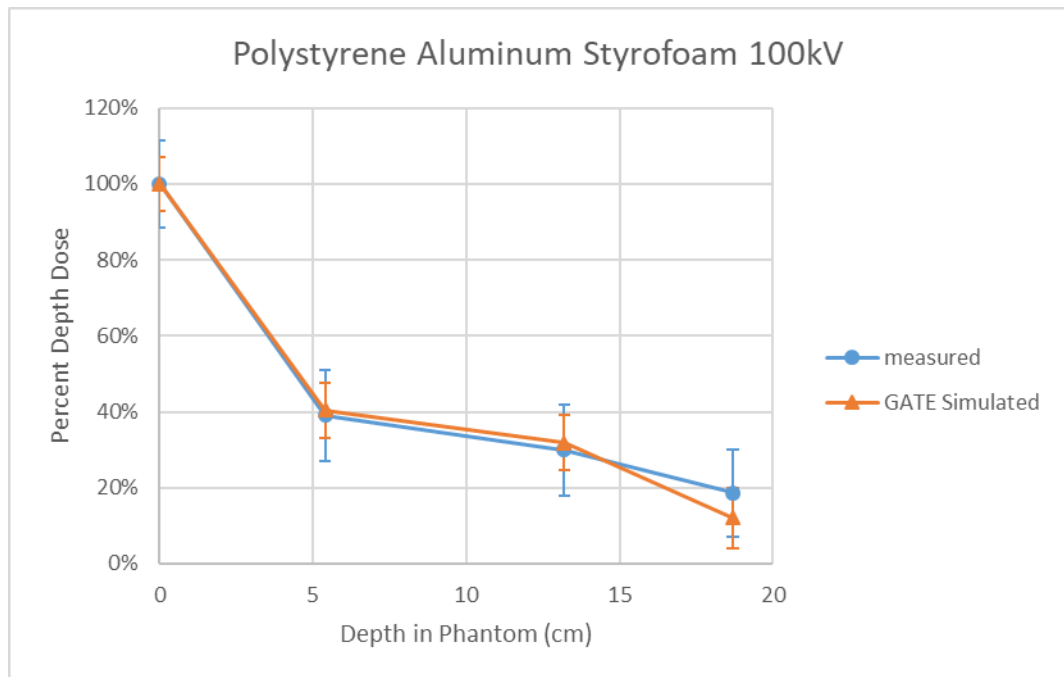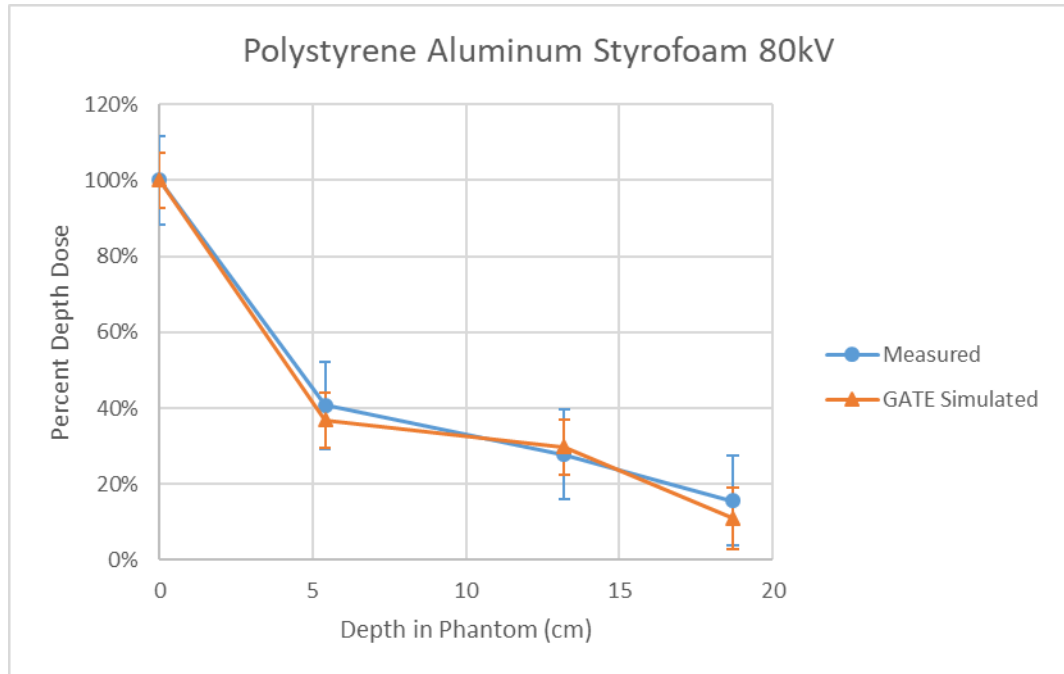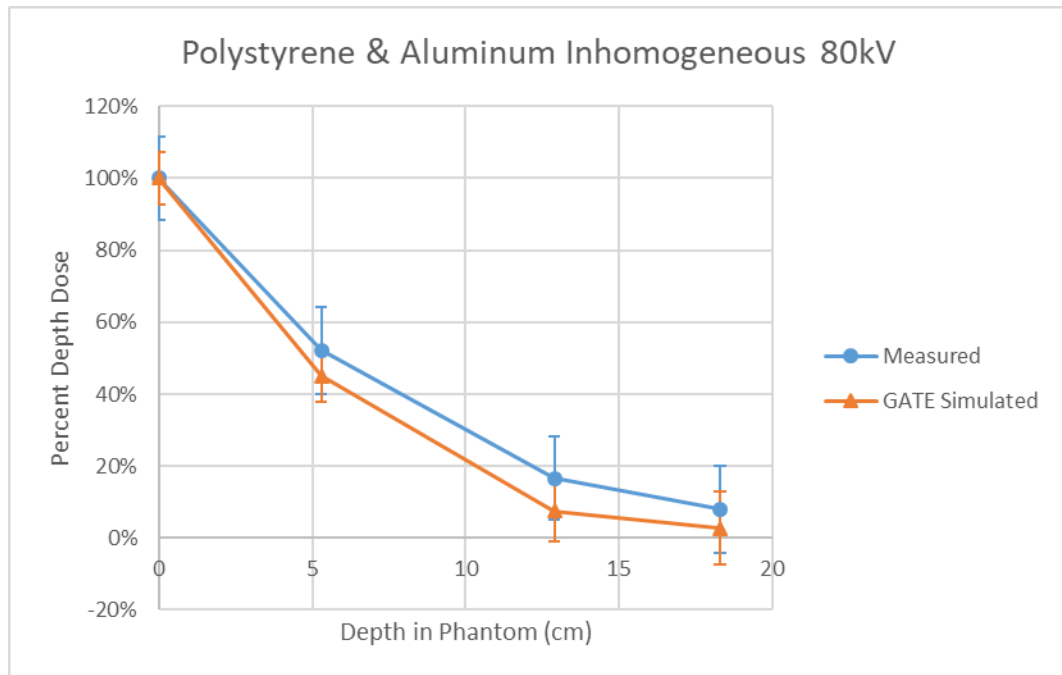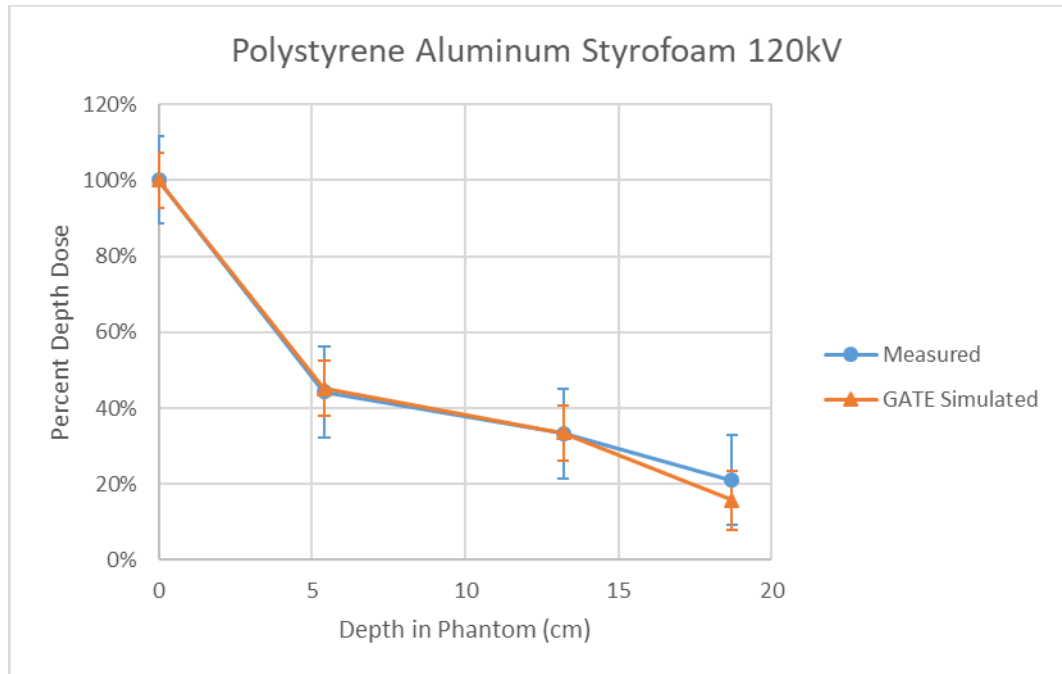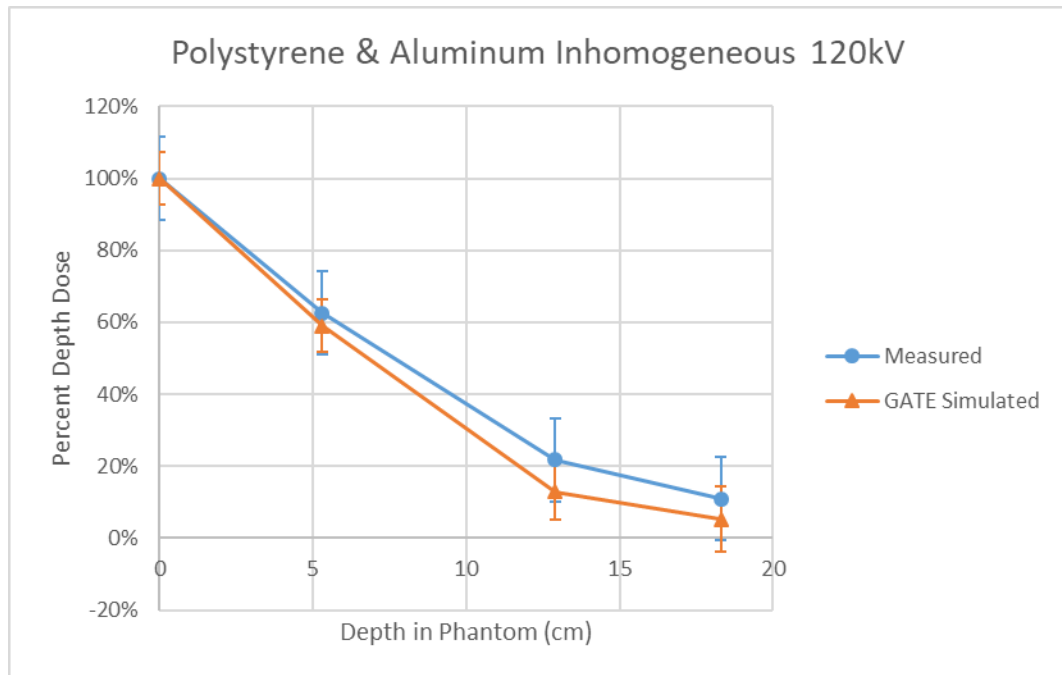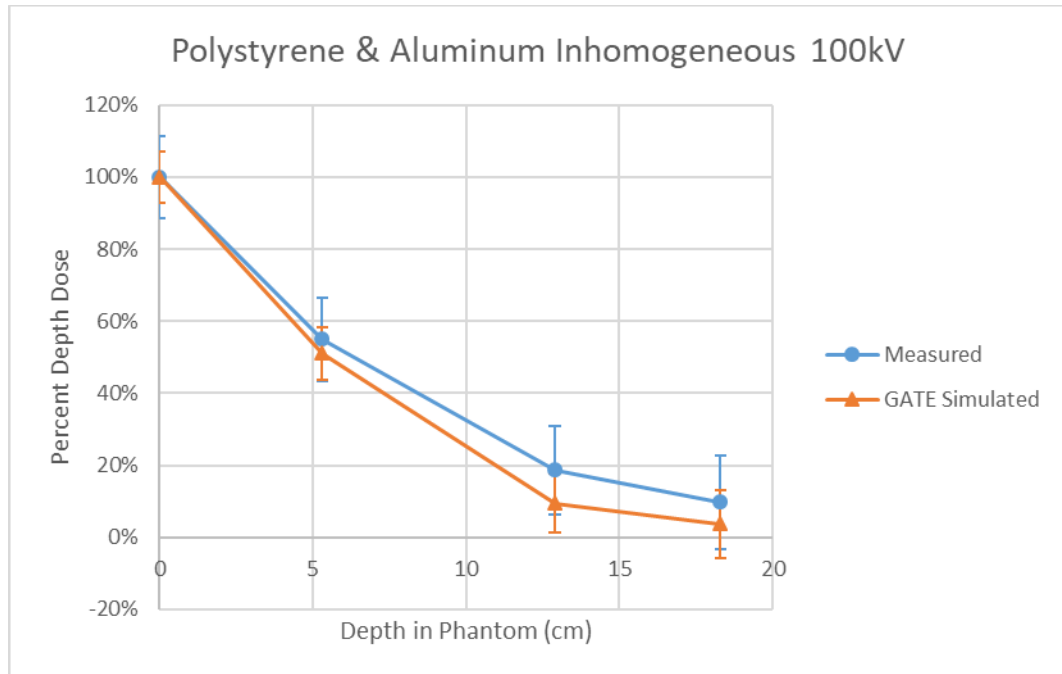
Figure 4-12 a-f: Depth dose comparison between measured and GATE simulation in the Inhomogeneous phantom containing polystyrene, Styrofoam and aluminum, or just polystyrene and aluminum. Measured and simulated doses were normalized to maximum dose which was at the surface of the phantom.

74

The results obtained from the homogeneous and inhomogeneous phantoms in the above experiments prove the validity of using GATE Monte Carlo code as a surrogate to measured data for the rest of this project. This will allow for the calculation of dose points in both phantoms and decedent subjects without having to implant dosimeters.

5   In situ measurements

1. Dosimetry measurements with nanoDots and anthropomorphic phantom to compile a standard data set for use in algorithm development and validation.

2. Dose measurements on decedents during PA and Lateral chest radiographs using nanoDots at the New Mexico Office of the Medical Investigator (OMI). Obtain radiographs and CT image data sets for use in algorithm development and Monte Carlo simulations.

3. Perform Monte Carlo simulations for validation of algorithm on varying body habitus and body weight and height.

4. Compare results from measured phantom data to Monte Carlo simulations in order to use Monte Carlo simulation data for future validation of algorithm without having to perform additional measurements

Most validations of mathematical algorithms or Monte Carlo simulations are based on dosimetry measurements using anthropomorphic phantoms. Although convenient, most anthropomorphic phantoms are created to represent the standard man size (73.2 kg and 178.6cm) which cannot account for variations in size and body habitus encountered in the clinic. It is imperative that the various Monte Carlo codes and calculation methods be validated on subjects that are bigger and smaller than standard man size. Varying body habitus can greatly affect

patient absorbed dose, and can be detrimental to standard calculation methods [15], [18].

However, it is not practical to verify dosimetry calculations via measurements on living patients. In order to ensure accuracy and reproducibility, measurements should be performed multiple times per patient per imaging procedure. This would entail exposing multiple patients to unnecessary radiation. A unique opportunity presents itself at the University of New Mexico Office of the Medical Investigator (OMI). With approval of the OMI Research Review Committee, it was possible to perform dosimetry measurements on the decedents undergoing post mortem examination [72]. Recently, many research projects have begun using post-mortem subjects for dosimetry studies. The use of cadavers or decedents allows the researcher to obtain multiple dose measurements on a single subject without the danger of causing harmful radiation effects [73]–[76]. This proven in situ dosimetry method allows for validation of Monte Carlo calculations using non-standard man size subjects, as well as, the new patient specific dosimetry algorithm proposed by this dissertation.

5.1 Anthropomorphic Phantom Dose Measurements

For the initial phantom portion of this project, radiographs and CT scans were performed on the Alderson Lung/chest Phantom. The phantom is an anthropomorphic phantom representing the torso of a male subject that is approximately 5 feet 9 inches (175 cm) tall and weighing 162 lbs. (73.5 kg). The materials making up the phantom are equivalent to natural bone and soft tissues [77]. The intent of this phantom imaging was to give a standard data set in order

to perform preliminary calculations in a controlled setting. A total of 14 nanoDot dosimeters were placed on the phantom on the anterior, posterior, right and left sides as shown in figure 5-1. nanoDot dosimeters were placed as follows: Anterior – level of thyroid, left, right and center chest. Posterior – back of neck at level of thyroid, left, right, center of back at level of anterior nanoDots. Left and right lateral sides – level of axilla, then equidistant center of chest and lower level of chest.

The nanoDot dosimeters were present only for their respective images (either Anterior-Posterior or Lateral) in order to accurately measure entrance and exit exposure from both the anterior-posterior and lateral radiographs.

Figure 5-1: Placement of the nanoDot dosimeters on the Alderson chest phantom. 4 nanoDots placed on the anterior and posterior surfaces, 3 nanoDots placed on lateral surfaces.

Due to the radio-transparency of the nanoDot dosimeters, a 0.177 caliber (4.5 mm) copper coated steel BB was placed in vicinity of the nanoDot. The BB will allow for the identification of the placement of the nanoDots on the radiographs.

78

All positioning and anatomical radiographs were performed by an ASRT certified and registered radiologic technologist to maintain consistency with clinical techniques and imaging. The Alderson phantom was positioned as would be done clinically for an AP supine chest radiograph, and a lateral-supine-cross table radiograph. The radiographs were performed in this manner to maintain consistency for the decedent radiographs performed at the OMI. Figure 5-2 shows the positioning for the both the anterior-posterior and lateral radiographs, respectively.
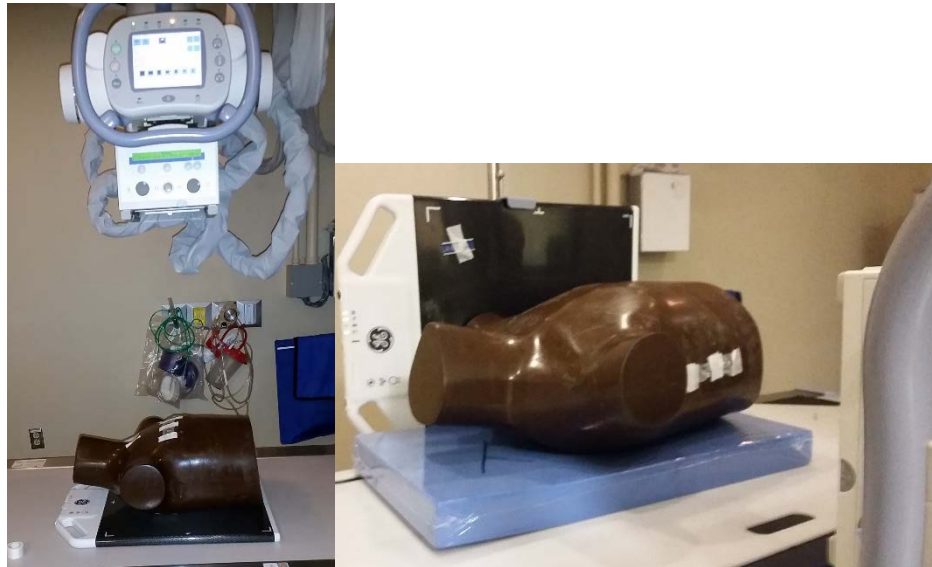
Figure 5-2: Clinical setup of the Alderson chest phantom for AP and Lateral radiographs. For the lateral radiograph, a radio transparent pad was placed underneath the phantom in order to lift it off the table and prevent any table artifacts in the image.

Both AP and lateral radiographs were performed at the University of New Mexico Hospital x-ray room 1, using a GE Discovery XR656 digital radiographic

system. The image technique used was 80 kVp and 4 mAs, large focal spot, with the x-ray tube positioned at 40 inch source-to-image-distance.

The radiographic AP and lateral images are shown in figure 5-3. Due to geometric magnification, the BB's placed on the beam entrance side of the phantom appear slightly larger than those on the beam exit side of the phantom.
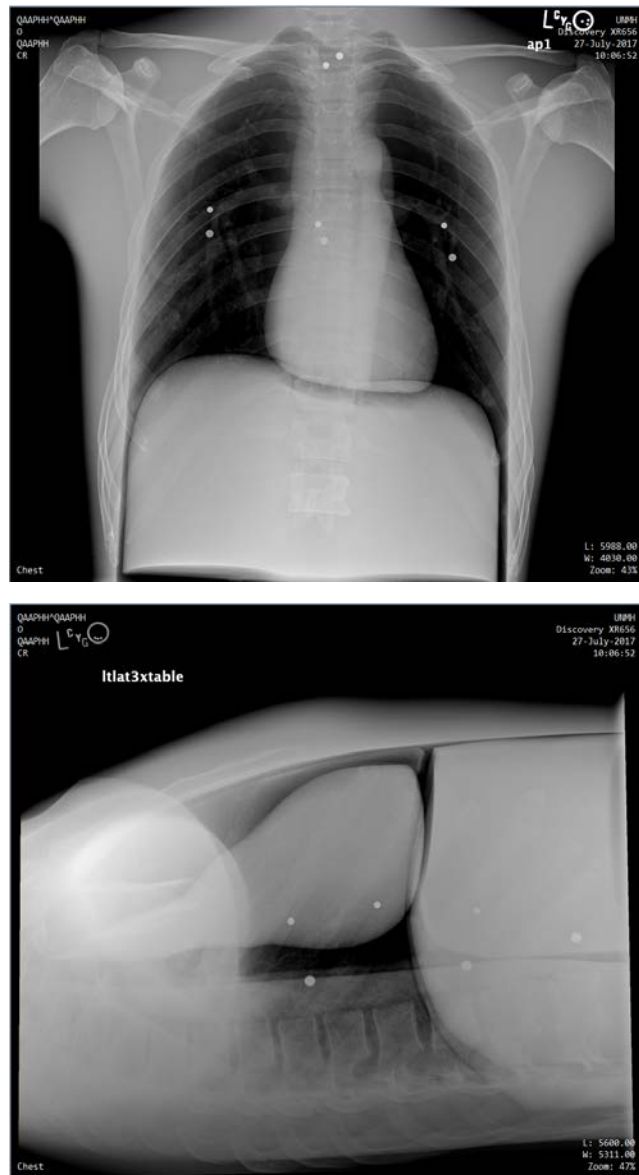
Figure 5-3: AP and lateral radiographs of the Alderson chest phantom. Presence of the 4.5mm BB's shows the general position of the nanoDot dosimeters.

The collected doses from each point were corrected for number of exposures and are shown in table 5-1.

Table 5-1: Measured doses at specified positions for both AP and Lateral radiographs.

Position	Dose (mGy)
Thyroid	0.262
Left chest	0.425
Right chest	0.424
Center chest	0.440
Neck back	0.017
Left back	0.047
Right back	0.046
Center back	0.018
Right side top	2.691
Right side middle	2.364
Right side bottom	1.531
Left side top	0.041
Left side middle	0.051
Left side bottom	0.026

The collected doses follow expectations for heal effect as well as attenuation through the phantom.

5.2 Large Anthropomorphic Phantom (Phantom +5 cm Super-Flex)

In order to ensure that a larger size "patient" data set was available, it was necessary to create a larger anthropomorphic phantom. This was accomplished by adding 5 cm of Super-flex bolus to the outside of the Alderson Lung/Chest phantom. As stated above, Super-flex bolus is a soft tissue equivalent material that is commonly used for both radiation oncology and diagnostic imaging studies when additional soft tissue equivalent material compensation is necessary. The larger phantom setup is shown in figure 5-4

Figure 5-4: Anthropomorphic phantom with 5cm of Super-flex added, and nanoDot dosimeters in place.

One of the benefits to creating a larger phantom this way was that nanoDot dosimeters were also able to be placed at depth; in this case 5 cm below the surface, in addition to the entrance and exit of the phantom. Again, both AP and lateral radiographs were performed at the University of New Mexico Hospital x-ray room 1, using a GE Discovery XR656 digital radiographic system. The image technique for the AP radiographs was 125 kVp and 6.3 mAs, large focal spot, with the x-ray tube positioned at 40 inch source-to-image-distance. The lateral radiographs were performed at 125 kVp and 12.5 mAs. The imaging technique was adjusted to account for the larger size of the subject, in order to obtain readable clinical images.

83
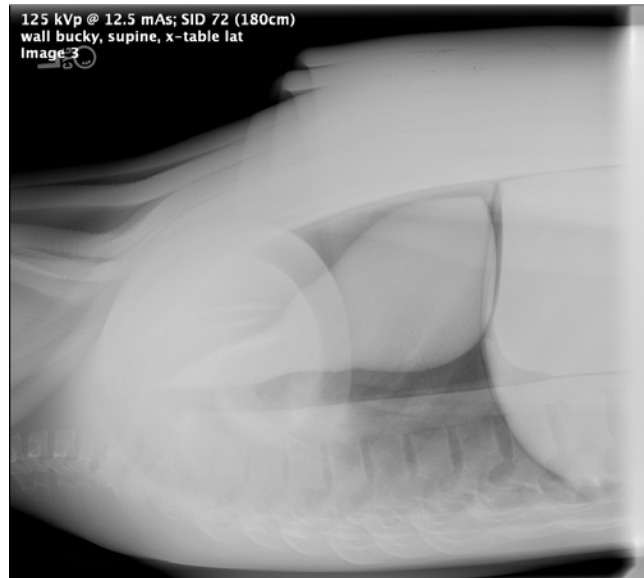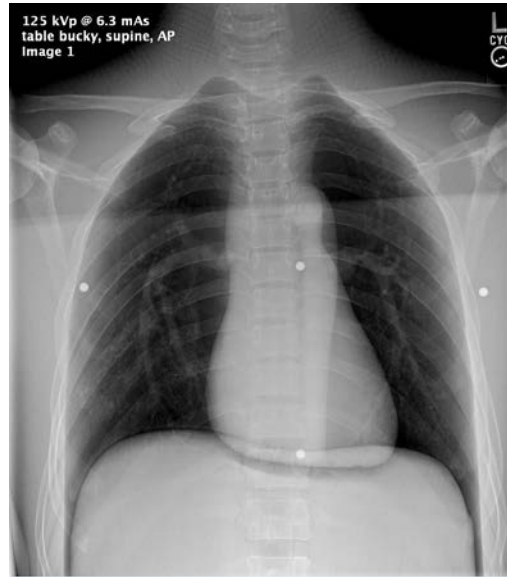
Figure 5-5: AP and Lateral radiographs of the anthropomorphic phantom with 5cm of Super-flex added.

Collected doses from the nanoDot dosimeters are shown below in table 5-2.

Table 5-2: nanoDot Dose readouts from anthropomorphic phantom with additional 5cm of Super-flex material.

Position	Dose (mGy)
Thyroid Entrance	0.312
Left Chest Entrance	2.198
Center Chest Entrance	2.436
Right Chest Entrance	2.317
Abdomen Entrance	2.761
Thyroid 5cm depth	0.974
Left Chest 5cm Depth	1.520
Center Chest 5cm Depth	1.657
Right Chest 5cm Depth	1.503
Abdomen 5cm Depth	1.686
Neck Back	0.052
Left Center Back	0.088
Center Back	0.049
Right Center Back	0.100

The measured doses for this phantom are higher as expected based on the increase in kV and mAs from the standard size phantom. Also, the doses collected from this experiment follow what is expected as far as attenuation through the subject if the general estimate of tissue having a half value layer of 4 cm at diagnostic energies, and the AP thickness of the phantom being 28 cm. The estimate would be for the exit dose to be approximately 0.01 times the entrance dose. This is a "rule of thumb" estimate only, as it neglects scatter contributions and other effects of the x-ray beam.

5.3 Decedent Measurements at the New Mexico Office of the Medical Investigator

All dosimetry measurements on decedent subjects were performed at the University of New Mexico Office of the Medical Investigator (OMI). Permission to perform dosimetry measurements at the OMI was obtained by submission of a "Request for Review of Research Involving OMI Resources" to Dr. Sarah Lathrop and the OMI research review committee. After review and acceptance by the committee, a presentation regarding the research and data collection process was presented at an OMI Operational Needs Meeting. The purpose of the Operational Needs meeting presentation was to allow the faculty and staff of the OMI to ask questions and obtain clarification of the data collection process and the reasons behind the research. The project was accepted unanimously by both the research review committee and operational needs meeting attendees.

Before data collection could begin, physics measurements were performed on the GE AMX-4+ Mobile Radiographic unit available in the forensic pathology lab of the OMI. The beam characterization measurements were performed as outlined in section 2.3.1-2.3.2. At 80kVp the half value layer of the GE AMX-4+ was determined to be 3.13 mmAl, and the output was 5.94mR/mAs at 40" SID.

Decedent dosimetry measurements were performed as closely as possible as described for the anthropomorphic phantom, with the exception of steps taken for contamination control. There are two modes of operation for the forensic pathology lab: "Stand Down" and "Autopsy". During Stand Down, the lab is considered to be at a level where there is minimal risk of contamination, and

personal protective equipment (PPE) requirements are at a minimum, consisting mainly of shoe covers and gloves. All physics measurements of the GE AMX-4+ were performed during Stand Down, and all equipment was decontaminated with wipes and cleaning solutions available before removing them from the lab.

During Autopsy, the lab is treated as a Biosafety Level 3 (BSL-3) facility. This includes additional training on PPE (i.e., N-95 mask and respirator fit training), the use of protective clothing that must not leave the lab, and vaccination requirements for personnel who will enter the lab during Autopsy [78]. All dosimetry measurements were performed either directly prior to, or during, Autopsy. Therefore, BSL-3 safety precautions needed to be observed, which included considerations to minimize contamination of the nanoDots which needed to be taken into and out of the lab after being placed on the decedents.

In order to minimize contamination to the nanoDots, they were first wrapped in Glad Press'n Seal ™, an airtight, liquid tight self-adhesive plastic wrap before taken into the lab. The nanoDots where then placed on the decedent subject in the same manner as they were on the anthropomorphic phantom for anterior-posterior and lateral on entrance and exit surfaces. See figure 5-6 for right lateral entrance placement of nanoDot dosimeters.

Figure 5-6: Showing placement of Press'n Seal ™ wrapped nanoDots for right lateral entrance on decedent at OMI.

Exposures were performed in accordance with the size of the decedent and techniques were determined by the forensic radiographer. For example, the AP Chest technique for the decedent in figure 5-7 below was 80kv and 12.5 mAs, whereas the AP chest technique for the decedent in figure 5-8 was 80kV and 3.2 mAs.

Figure 5-7: Large decedent, DJS009, male 162.2 cm 97 kg

Figure 5-8: Small decedent, DJS008, female 151.0 cm, 33.2 kg.

After exposures and radiographic images were complete, the nanoDots were taken out of the imaging room, where the wrapped dosimeter was cleaned with disinfecting wipes before the Press'n Seal ™ was removed and the nanoDots placed in a transport container for removal from the forensic lab. This process was repeated for all dosimetry measurements performed at the OMI. Once measurements were completed, anonymized radiographs and CT scans were collected for use in this project.

CT scans of the relevant anatomy for each decedent were imported into GATE for dose simulation, see figure 5-9 below. The radiographic unit available at the OMI is a GE AMX-4 Plus mobile radiographic unit. Physics testing as described in Chapter 2 was performed on this unit in order to accurately model the x-ray unit in GATE. Results listed in table 5-3 show decent agreement between the measured doses and GATE simulations. Accuracy of GATE simulations can be improved by increasing the number of histories run (10 million histories were run for this test). Some uncertainty related to positioning of the decedents in the OMI lab may also contribute to the uncertainty in GATE as the dose point position relies on recognizable landmarks. These landmarks may not be remain consistent between radiographic and CT images due to the difficulty associated in positioning decedent subjects.

90

Table 5-3: Comparison of results from decedent measurements and GATE simulations on associated CT scans.

Decedent	Position	Measured Dose (mGy)	Unc.	GATE dose (mGy)	Unc.	% difference
DJS008	Entrance	0.319	0.116	0.362	0.081	
DJS008	Exit	0.028	0.127	0.027	0.073	
DJS008	Total deposited	0.437	0.172	0.507	0.109	**14.8%**
DJS009	Entrance	1.395	0.114	1.267	0.082	
DJS009	Exit	0.024	0.149	0.040	0.268	
DJS009	Total Deposited	0.906	0.187	0.793	0.280	**13.3%**

91
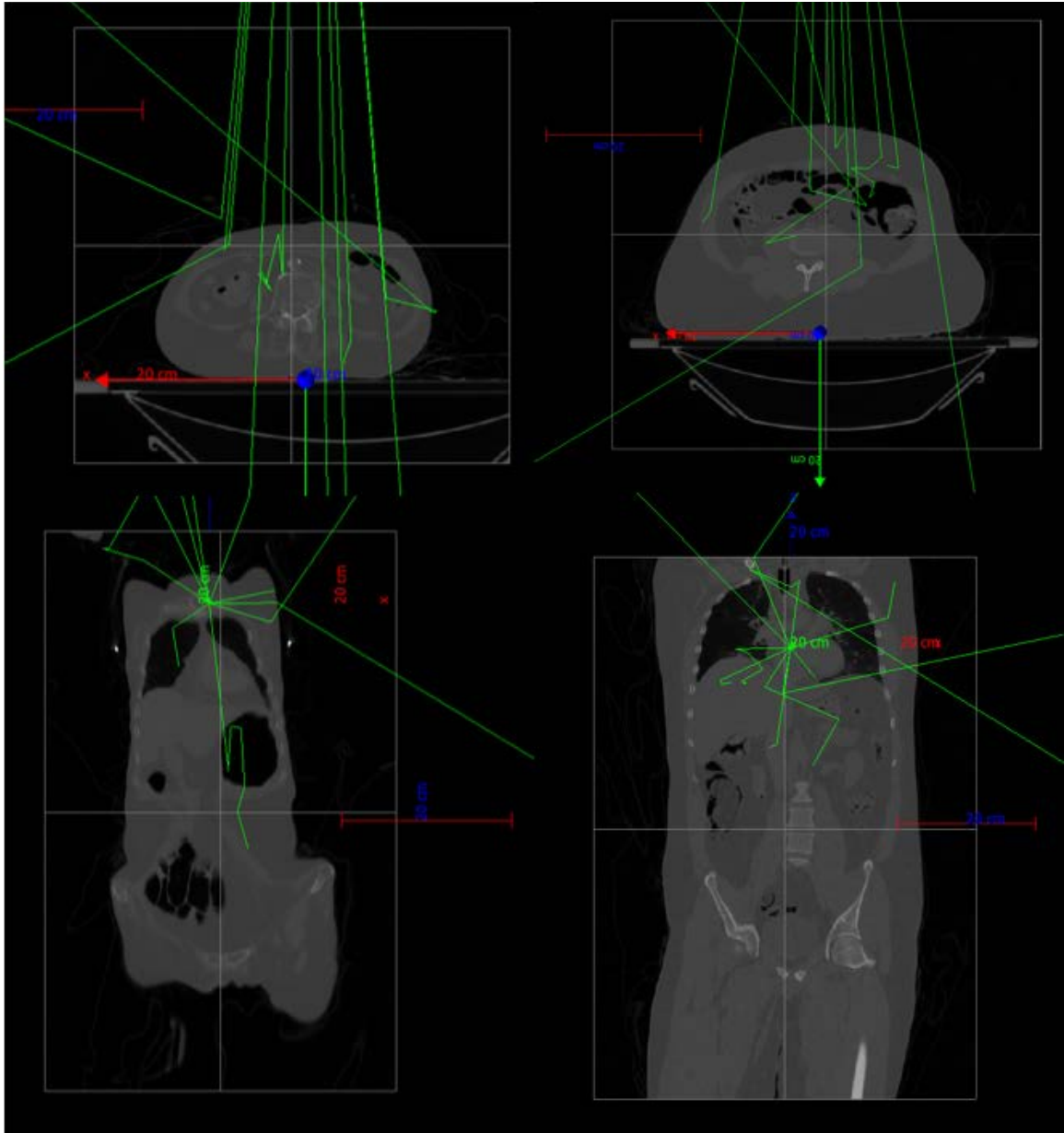
Figure 5-9: Clockwise from top left, small decedent axial image, large decedent axial image, large decedent coronal image, small decedent coronal image as depicted in GATE. Note the white box surrounding all images has the same dimensions (1x1x2m).

6 Algorithm

Developed in this work is an algorithm to estimate the total absorbed dose to a subject utilizing image data captured at the time of the exam. The algorithm steps are as follows:

1. Calculation of the entrance skin dose utilizing the dose correction factor, which developed and discussed in this chapter.

2. Calculation of the exit skin dose which is an adaptation of the entrance skin dose formula described above.

3. Calculation of the energy imparted from the entrance and exit skin dose utilizing the saturated-scatter method.

4. Finally, calculation of the total absorbed dose by combining an estimation of the subject mass and the energy imparted as described above.

6.1 Information available with newer Digital Radiography systems

Recall that the purpose of this project is to provide a relatively straightforward, accurate way of providing a patient specific dose estimate based on physics measurements in the clinic and information available from patient images. This goal is facilitated on newer radiographic systems where the useful information is provided by the imaging system. Specifically, new digital radiography systems provide information related to exposure techniques and other factors that contribute to patient dose. This information, such as kV, mAs, field size, Exposure Index, and Dose Area Product can greatly improve the accuracy of dose

93

calculations by improving on current calculation methods. Of particular use to the development of this algorithm were the Exposure Index (EI) and Dose Area Product (DAP).

GE x-ray systems also report the DAP in dGy-cm^2 for each exposure. What is referred to as dose in this system is really the air kerma integrated over the exposure field in the plane perpendicular to the beam axis [79]. The air kerma is the kinetic energy released per unit mass as x-ray photons interact with the air. Because of beam divergence (field size increasing at distance from source), and the inverse square law (intensity decreasing at distance from source), the DAP will remain constant throughout the beam path. As defined, the DAP is the dose in air without backscatter [80] and therefore must be converted from dose in air to dose in tissue, which will account for the absorbed dose from primary radiation at the entrance of the subject

6.2 Dose Equation for Calculating Entrance Dose

When accounting for the entrance skin dose, the calculation is greatly simplified by the availability of the Dose Area Product. Recall that ESD is calculated by determining the exposure, in air, at the entrance to the patient. The exposure at this point is determined by knowing the typical output of the x-ray unit (in mR/mAs) at a specified point. When multiplied by the mAs set on the unit, and applying the exposure to dose conversion factor, the AK at the entrance of the subject can be calculated. On units that provide a DAP, all of these factors are taken into account and the AK at any point along the beam path can be determined

94

once the field size at distance is known. Once the data is gathered, the entrance dose calculation is performed by the following formula

$$ESD = \left(\frac{DAP\ mGy\ cm^2}{field\ size\ at\ entrance\ cm^2}\right) * \left(\frac{\mu_{ab}}{\rho}\right)_{air}^{tissue} * (1 + dose\ correction\ factor) \qquad \text{6-1}$$

Where $\left(\frac{\mu_{ab}}{\rho}\right)_{air}^{tissue}$ is the ratio of mass energy absorption coefficients for tissue to air in order to convert the absorbed dose in air to that in tissue based on the effective energy of the x-ray beam [42]. All mass energy absorption coefficients are interpolated from NIST available data [59] based on the effective energy of the x-ray beam as calculated from the measured HVL. The field size at the entrance of the phantom was calculated by taking the set field size at SID and correcting back to the entrance of the phantom by using the method of similar triangles. The *dose correction factor* is the ratio of the EI and average grayscale value in the region of interest of the resultant image (equation 6-2).

$$Dose\ Correction\ Factor = \frac{Exposure\ Index}{Average\ Grayscale\ in\ ROI} \qquad \text{6-2}$$

6.3 Dose Equation for Calculating Exit Dose

The exit dose is calculated in a similar manner using elements of the ESD algorithm. Similar to the entrance skin dose calculation with the added consideration of subject thickness. The exit dose is described by the equation

95

$$exit\ dose = \left(\frac{DAP\ mGy\ cm^2}{field\ size\ at\ exit\ cm^2} \right) * \left(\frac{\mu_{ab}}{\rho} \right)_{air}^{tissue} * (1 + dose\ correction\ factor) * e^{-\bar{\mu}d} \qquad 6\text{-}3$$

Additional factors to the entrance skin dose algorithm are d, the total subject thickness, and $\bar{\mu}$ the average linear attenuation coefficient along the beam path. The linear attenuation coefficient is calculated from mass energy absorption data and material density data available from NIST [59]. The field size at the exit of the subject was determined by position of the subject and set field size at SID. For the 12cm Super-Flex (homogeneous) stack, Large Inhomogeneous, Small Inhomogeneous, the exit field size was equal to the field size at SID since these phantoms were placed directly on the imaging detector. The same was true for the Anterior-Posterior image of the anthropomorphic chest phantom. For the lateral image of the Anthropomorphic Chest, as well as, the AP and lateral image of the Anthropomorphic Chest with 5cm Super-Flex the exit to detector distance varied and therefore a similar triangle calculation was performed to account for the differing exit field sizes.

6.4 Total dose deposited

As discussed in chapter 1, the most common way to perform a dose calculation for patients of diagnostic radiographic exams is by performing the entrance skin dose (ESD) calculation, as shown in equation 1-1.

96

$$ESD \ = \ \frac{X * mAs * D^2}{[SID - (t + b)]^2} * BSF \qquad \qquad 1\text{-}1$$

Once the entrance skin dose is calculated, various weighting factors can be applied in order to obtain an estimate of whole body effective dose [24]. It is also well known that in the diagnostic energy range (20keV − 150keV), the peak skin dose (PSD) occurs at the entrance to the subject [57], [81], [82]. Therefore, it is common for any dose calculation to end with equation 1-1 as a measure of the highest dose delivered to the patient.

Although the entrance skin dose may be the peak dose received by the patient, it is important to note that the underlying organ doses, and therefore whole body effective dose, are not readily determined from the ESD[83]. It is therefore acceptable to look for the integral dose, or total energy imparted, in order to gain a better understanding of the possible effects of the radiation dose on the individual. The integral dose, ∑, is typically expressed as

$$\Sigma = \ \rho \int_0^d D(x)A(x)dx \qquad \qquad 6\text{-}4$$

Where *x* is the depth in the phantom along the central beam axis, *D(x)* is dose at depth, and *A(x)* is the area of the radiation field at depth. At diagnostic energies, electronic equilibrium can be assumed, and absorbed dose at depth *x* in the phantom for a monoenergetic beam can be described by

97

$$D(x) = \psi \frac{\mu_{ab}}{\rho} = Ne^{(-\mu x)} h\upsilon \frac{\mu_{ab}}{\rho}$$

6-5

Where ψ is the energy fluence, which is the product of the total number of photons at depth, $Ne^{(-\mu x)}$, and the photon energy $h\upsilon$, μ and $\frac{\mu_{ab}}{\rho}$ are the linear attenuation coefficient and the mass-energy absorption coefficient of the target material resepectively. Substituting equation 6-4 into 6-3 will give

$$\Sigma = \rho \int_0^d Ne^{(-\mu x)} h\upsilon \frac{\mu_{ab}}{\rho} A(x) dx$$

6-6

Which is the integral dose from primary radiation for a monoenergetic beam in a phantom of thickness d [42].

The International Council on Radiation Units and measurements (ICRU) helped to facilitate the calculation of the integral dose by defining it in terms of the energy imparted:

$$\varepsilon = R_{in} - R_{out} + \sum_n Q_n$$

6-7

Where R_{in} is the entrance energy, R_{out} is the energy that leaves the subject, and $\sum Q_n$ is equal to the total release of energies from nuclear transformations [84]. In the diagnostic energy range, $\sum Q_n$ is effectively equal to zero [85]. If the energy imparted and the irradiated mass of the subject are known then the integral dose is forthcoming.

It is also possible to calculate the energy imparted when an entrance and exit dose are known. The saturated scatter-method [86] facilitates the calculation of energy imparted when exit and entrance dose are known and under electronic

98

equilibrium conditions of diagnostic imaging. The energy imparted can be calculated by

$$\varepsilon = \rho A_0 \int_0^d D(x) \left(\frac{SSD + x}{SSD}\right)^2 dx \qquad \text{6-8}$$

Where ρ is the density of the subject, A_0 is the area of the x-ray field at the entrance, $D(x)$ is the dose at depth, and d is the total thickness of the subject [83], [87].

Evaluating this integral gives

$$\varepsilon = \rho A_0 \left(\frac{D(0) * (SSD)^3}{3(SSD)^2} - \frac{D(d) * (SSD + d)^3}{3(SSD)^2}\right) \qquad \text{6-9}$$

Equation 6-9 will give the energy imparted when the entrance and exit dose are known. To calculate the total absorbed dose, it is necessary to divide equation 6-9 by the total mass of the subject in the radiation field. The total mass can be calculated by determining the volume of material in the beam and multiplying by the density of the material. Since the x-ray beam is divergent with a square base, the volume can be calculated by using equation 6-10 for a truncated pyramid as shown in figure 6-1, where a is the length of the side of the entrance field, b is the length of the side of the exit field, and h is the thickness of the subject.

$$V = \frac{1}{3}(a^2 + ab + b^2) * h \qquad \text{6-10}$$

99
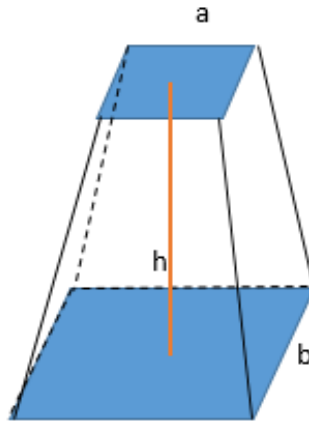
Figure 6-1: Diagram of truncated pyramid.

Once these values are known, the integral dose can be calculated by dividing the
energy imparted by the product of the volume and density of the material.

$$\Sigma = \frac{\varepsilon}{V * \rho} \qquad\qquad 6\text{-}11$$

100

6.5 Examples

Information needed for this calculation is listed in table 6-1 below.

Table 6-1: Factors needed for calculation.

Factor	Collected from
DAP	DICOM data
Field size at SID	DICOM data
SID	DICOM data
Exposure Index (EI)	DICOM data
Detector configuration (table top, chest board, etc.)	Technologist
Patient thickness	Images and/or technologist
HVL	Physicist
Patient exit to detector distance	Physicist
Average grayscale over region of interest	Physicist determination from resultant image

Information collected by physicist is collected and verified upon acceptance testing of the unit, at annual physics surveys, or when appropriate after service calls. Therefore, this information is collected and updated on an interval consistent with medical physics quality control procedures. The majority of the information needed is collected from the DICOM metadata that is part of the final image.

101

Five phantoms were imaged on the GE Discovery XR656 digital radiographic system using a combination of techniques to give data for the eleven examples discussed here. The phantoms used were the 12cm Super-Flex (homogeneous) stack, Large Inhomogeneous, Small Inhomogeneous, Anthropomorphic Chest, and Anthropomorphic Chest with 5cm Super-Flex phantoms as described in chapters 4 and 5. The 12cm Super-Flex stack, Large Inhomogeneous, and Small Inhomogeneous phantoms were imaged using multiple techniques in attempt to test the adaptability of the algorithm to various technique changes. The Anthropomorphic Chest and Anthropomorphic Chest with 5cm Super-Flex phantoms were imaged by an ASRT certified and registered radiologic technologist in order to accurately simulate clinical patient image acquisition.

Each phantom imaging study was performed by measuring the entrance and exit doses with nanoDot dosimeters. The total absorbed dose according to nanoDot measurements was then determined by equation 6-10 as described above. All data as required in table 6-1 above was collected at the time of each phantom test. The HVL for each set kV of interest was collected initially during physics testing as described in chapter 3, and tested before each phantom test to ensure accuracy and continuity of the beam quality of the system. All relevant distances (SID, patient exit to detector configuration, etc.) were measured at time of each phantom test to ensure accuracy of the calculation. All images were annotated with pertinent information and downloaded from PACS as soon as the imaging test was complete.

6.6 Results

Results from measurements, "traditional" dose calculations, and new dose algorithm calculations are listed in the following tables along with associated uncertainties, and percent differences between each calculation technique when compared to measured data. To note, there is no measured nanoDot data available for the Lateral Anthropomorphic Chest with 5cm Super-Flex phantom even though radiographic images were taken. However, as shown in chapters 4 and 5, it is possible to perform a GATE simulation on Computed tomography images of the subject and obtain accurate dose data that can be used in place of measurements. Therefore, the Anthropomorphic Chest with 5cm Super-Flex phantom images were imported into GATE, and a simulation dose data was used for comparison to traditional and new calculation methods.

Table 6-2: Comparison of Measured dose to traditional calculation to new Algorithm calculation for 12cm Super-Flex phantom at multiple kV settings with constant mAs. Also included are associated uncertainty with each value along with the percent difference from each calculation method compared to the measured dose.

Phantom	Position	Measured Dose (mGy)	Unc.	GATE (mGy)	Unc.	%diff	Trad. Calc. (mGy)	Unc.	% diff	Algorithm (mGy)	Unc.	% diff
12cm Super-Flex 80kV	Entrance	0.059	0.12	0.053	0.079		0.039	0.122		0.037	0.073	
12cm Super-Flex 80kV	Exit	0.014	0.166	0.010	0.117		0.012	0.122		0.009	0.073	
12cm Super-Flex 80kV	Dose Deposited	0.084	0.205	0.083	0.141	0.7%	0.047	0.173	56.6%	0.052	0.104	47.2%
12cm Super-Flex 100kV	Entrance	0.082	0.122	0.083	0.080		0.063	0.122		0.063	0.073	
12cm Super-Flex 100kV	Exit	0.024	0.161	0.017	0.117		0.026	0.122		0.020	0.073	
12cm Super-Flex 100kV	Dose Deposited	0.104	0.202	0.125	0.142	19.0%	0.056	0.173	59.2%	0.074	0.104	33.2%
12cm Super-Flex 120kV	Entrance	0.122	0.116	0.124	0.079		0.091	0.122		0.099	0.073	
12cm Super-Flex 120kV	Exit	0.031	0.119	0.038	0.101		0.044	0.122		0.037	0.073	
12cm Super-Flex 120kV	Dose Deposited	0.166	0.166	0.151	0.129	9.5%	0.060	0.173	94.3%	0.098	0.104	51.4%

Table 6-3: Comparison of Measured dose to traditional calculation to new Algorithm calculation for Large and Small Inhomogeneous phantom at multiple kV settings with constant mAs. Also included are associated uncertainty with each value along with the percent difference from each calculation method compared to the measured dose.

Phantom	Position	Measured Dose (mGy)	Unc.	GATE (mGy)	Unc.	% diff	Trad. Calc. (mGy)	Unc.	% diff	Algorithm (mGy)	Unc.	% diff
Large Inhom. 80kV	Entrance	0.071	0.116	0.060			0.056	0.122		0.053	0.073	
Large Inhom. 80kV	Exit	0.016	0.129	0.009			0.014	0.122		0.008	0.073	
Large Inhom. 80kV	Dose Deposited	0.029	0.174	0.033	0.104	13.2%	0.020	0.173	34.9%	0.029	0.104	1.1%
Large Inhom. 100kV	Entrance	0.104	0.149	0.102			0.090	0.122		0.091	0.073	
Large Inhom. 100kV	Exit	0.030	0.134	0.017			0.029	0.122		0.017	0.073	
Large Inhom. 100kV	Dose Deposited	0.030	0.200	0.053	0.104	54.3%	0.020	0.173	41.5%	0.042	0.104	32.7%
Small Inhom. 80kV	Entrance	0.074	0.123	0.058			0.056	0.122		0.050	0.073	
Small Inhom. 80kV	Exit	0.011	0.236	0.003			0.014	0.122		0.007	0.073	
Small Inhom. 80kV	Dose Deposited	0.041	0.266	0.043	0.114	4.6%	0.020	0.173	67.3%	0.027	0.104	38.9%
Small Inhom. 100kV	Entrance	0.113	0.12	0.104			0.090	0.122		0.081	0.073	
Small Inhom. 100kV	Exit	0.017	0.114	0.005			0.029	0.122		0.015	0.073	
Small Inhom. 100kV	Dose Deposited	0.063	0.166	0.076	0.178	18.8%	0.020	0.173	103.1%	0.038	0.104	49.5%

Table 6-4: Comparison of Measured dose to traditional calculation to new Algorithm calculation for Anthropomorphic Chest and Anthropomorphic Chest with 5cm Super-Flex. Also included are associated uncertainty with each value along with the percent difference from each calculation method compared to the measured dose. *No measured data was taken for the lateral view of the Antrhopomorphic Chest with 5cm Super-Flex phantom, GATE simulation data was used instead.

Phantom	Position	Measured Dose (mGy)	Unc.	GATE dose (mGy)	Unc.	% diff	Trad. Calc. (mGy)	Unc.	% diff	Algorithm (mGy)	Unc.	% diff
Chest AP 80kV	Entrance	0.446	0.114	0.480	0.072		0.410	0.122		0.433	0.073	
Chest AP 80kV	Exit	0.019	0.138	0.009	0.134		0.027	0.122		0.028	0.073	
Chest AP 80kV	Dose Deposited	0.349	0.179	0.397	0.152	**12.9%**	0.272	0.173	**24.9%**	0.322	0.104	**8.1%**
Chest Lat 80kV	Entrance	2.364	0.114	2.216	0.073		2.068	0.122		2.358	0.073	
Chest Lat 80kV	Exit	0.051	0.120	0.056	0.124		0.102	0.122		0.052	0.073	
Chest Lat 80kV	Dose Deposited	0.925	0.166	0.855	0.144	**7.8%**	0.727	0.173	**23.9%**	0.921	0.104	**0.4%**
Chest 5cm AP 125 kV	Entrance	2.436	0.115	2.394	0.071		2.492	0.122		2.304	0.073	
Chest 5cm AP 125 kV	Exit	0.049	0.155	0.031	0.118		0.478	0.122		0.216	0.073	
Chest 5cm AP 125 kV	Dose Deposited	1.189	0.193	1.193	0.138	**0.4%**	0.566	0.173	**70.9%**	1.020	0.104	**15.2%**
Chest 5cm LAT 125 kV*	Entrance	*	*	3.600	0.073		1.132	0.122		3.361	0.073	
Chest 5cm LAT 125 kV*	Exit	*	*	0.160	0.133		0.182	0.122		0.35	0.073	
Chest 5cm LAT 125 kV*	Dose Deposited	*	*	3.880	0.152	*	0.934	0.173	**122.4%**	3.262	0.104	**17.3%**

Since all organ doses for these experiments are considered to be low, the constraint for accuracy of the calculated dose as determined by the International Commission on Radiation Units and Measurements is that an accuracy of 30-50% is acceptable [88]. As the above tables demonstrate, the new algorithm consistently provides more accurate total absorbed dose for each phantom model with less uncertainty than the traditional method for dose calculations. In the case of the standard man size, and larger man size (Chest phantom plus 5cm Super-Flex) anthropomorphic phantoms the accuracy of the new algorithm exceeds the expected accuracy.

For the planar phantoms, the discrepancy between the algorithm and measured doses was to be expected. As discussed below, the greater inaccuracy seen with the non-anatomical phantoms is largely due to the fact that there is no anatomy present, and therefore the processing algorithm contributes a greater error the EI, which in turn, will add to the uncertainty in the algorithm.

This leads to the conclusion that although the dose calculation algorithm presented here has improved the accuracy for patient dose calculations, it should not be used with non-anthropomorphic phantoms due to the greater uncertainty associated with an incorrectly calculated EI.

6.7 Theory

When performing a dose calculation there are three things to consider as the x-ray beam traverses the subject: beam hardening, attenuation, and scatter contributions. Each of these considerations will affect the total dose deposited by either increasing or decreasing the end result [89].

107

Beam hardening occurs when a polyenergetic x-ray beam interacts in a medium, the lower energy x-rays are more readily attenuated, leaving the higher energy x-rays to continue on. This will result in an overall higher average energy for the x-ray beam as it traverses the subject [45], [90]. Beam hardening is accounted for in this algorithm by means of using the equivalent energy for the specific x-ray unit. As shown in chapter 4, considering the equivalent or effective energy based on the half value layer of this unit, it is possible to perform these accurate calculations by accounting for beam hardening prior to the calculation by using the half value layer to calculate the effective energy of the x-ray beam.

Attenuation is the fractional change in the intensity of the x-ray beam by a relatively few, but large energy-loss interactions with the subject [33]. For a typical broad-beam geometry as is present in diagnostic imaging, the attenuation happens via the exponential equation

$$I = I_0 e^{-\mu d} \hspace{3cm} \text{6-12}$$

Where d is the thickness of material, and μ is the attenuation coefficient for the material based on material properties and the energy of the incoming x-ray photons. For diagnostic energies electronic equilibrium is assumed and the mass energy-absorption coefficient, $\left(\frac{\mu_{ab}}{\rho}\right)$, is used to calculate the linear attenuation coefficient.

The grayscale of the image is a visual representation based on the number of photons detected after they have passed through the patient. The differential

108

attenuation from the differing tissues help make up the image on the detector and is dependent on the subject contrast. Subject contrast is based on the fundamental interactions between the x-ray photons and the object being imaged. Grayscale mapping occurs based on the number of photons detected in a region after differential attenuation through the object due to the subject contrast present. Digital radiography grayscale is displayed as the inverse of the number of photons detected [45]. That is, the higher the number of photons detected, the lower the grayscale value, meaning that no detected photons would map to white (high average grayscale value) and many photons would be black (0 average grayscale value).

The exposure index (EI) is proportional to detector entrance exposure, and is typically, depending on manufacturer, a measure of detector entrance dose. For the GE XR626, dividing the EI by 100 will give the detector entrance dose in microgray. The EI is calculated by the system and is based on x-ray imaging techniques, collimation (physical or software), the raw image data, anatomy segmentation, and calibration of the system. The GE XR626 system performs the EI calculation based on the "original data" which is the raw data (pixel values read directly after analogue to digital conversion) with minimal corrections applied. The corrections applied to the original data image are those for bad pixels, gain offset, and geometrical distortions. Therefore, no additional image processing is applied to the image before the EI is calculated. Also, the EI is limited to the value, or region, of interest which is limited by segmentation to the anatomy of the image,

109

and therefore any empty background of the detector (black space) will not affect the EI.

The average grayscale value and the EI are related to the absorbed dose in the region of interest which includes scatter and primary beam components. The average grayscale for the region of interest is determined by analyzing the image in a software program, such as ImageJ [65], [91]. As stated, the region of interest for the image is determined by the proprietary processing algorithms of the vendor, however, it is possible to hypothesize where the region of interest will be based on the processing algorithm chosen by the technologist. In the case of figure 6-2 below, the technologist has chosen an AP chest processing algorithm, therefore the region of interest can generally be described by the yellow box as depicted.
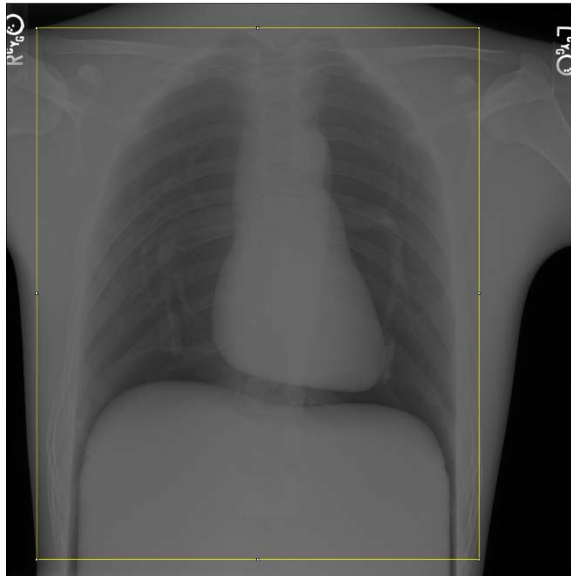
Figure 6-2: Chest AP phantom image. Yellow outline depicts the selected region of interest for average grayscale value.

110

Using these values in equation 6-1 will yield the entrance skin dose in mGy for the patient based on the selected image.

The region of interest for each processing algorithm is determined by a proprietary method that is vendor specific. For the GE Discovery XR656 radiographic system used for this project, the region of interest is identified through image processing techniques that segment out relevant anatomic data based on the processing algorithm and view chosen. For example, in figure 6-2 since an AP Chest processing algorithm was chosen the image processing will apply an anatomy segmentation algorithm to look for key anatomical landmarks (i.e., lungs, heart etc.) and then determine the EI based on the underlying detector exposure [21]. This method of determining the EI also explains why the homogeneous and inhomogeneous planar phantoms had less accuracy when using the EI/Grayscale correction factor. Since the phantoms had no relevant anatomy, but were still processed under the AP Chest algorithm, the EI was most likely miscalculated and therefore skewed the resulting dose calculations.

111

6.8 Steps to complete the algorithm for calculation of total absorbed dose

In order to calculate the total absorbed dose to a patient using radiographic images, the following steps are performed:

1. Calculation of the entrance dose by applying the ESD formula from this dissertation as displayed below.

$$ESD = \left(\frac{DAP\ mGy\ cm^2}{field\ size\ at\ entrance\ cm^2}\right) * \left(\frac{\mu_{ab}}{\rho}\right)_{air}^{tissue} * (1 + dose\ correction\ factor) \qquad \text{6-1}$$

This also requires calculation of the *dose correction factor* developed in this work by using the exposure index and average grayscale in the formula provided in 6-2

$$Dose\ Correction\ Factor = \frac{Exposure\ Index}{Average\ Grayscale\ in\ ROI} \qquad \text{6-2}$$

2. Calculation of the exit dose by use of equation 6-3 below

$$exit\ dose = \left(\frac{DAP\ mGy\ cm^2}{field\ size\ at\ exit\ cm^2}\right) * \left(\frac{\mu_{ab}}{\rho}\right)_{air}^{tissue} * (1 + dose\ correction\ factor) * e^{-\bar{\mu}d} \qquad \text{6-3}$$

Where $\left(\frac{\mu_{ab}}{\rho}\right)_{air}^{tissue}$ and $\bar{\mu}$ are determined from NIST attenuation tables and evaluation of the equivalent energy of the x-ray beam used.

3. Determination of the energy imparted by using the saturated-scatter method and the entrance and exit doses using equation 6-9

112

$$\varepsilon = \rho A_0 \left(\frac{D(0) * (SSD)^3}{3(SSD)^2} - \frac{D(d) * (SSD + d)^3}{3(SSD)^2} \right)$$

6-9

4. Calculate the total dose deposited by dividing the energy imparted by the mass irradiated.

7 Future work

This dissertation developed a method for performing patient specific dose calculations that incorporates data provided by the digital images. Future work for this project should include testing the dose calculation algorithm using additional anatomical regions, such as pelvis, abdomen, and skull. This project focused on AP and Lateral chest processing algorithms whereas there are multiple processing algorithms for each anatomical location. More importantly, application to pediatric studies should be investigated as pediatric patients have a greater risk associated with imaging studies.

Additionally, this project focused on one particular model of Digital Radiographic unit when there are multiple vendors with various processing methods that should all be tested. More importantly, this research lays the foundation for an automated process that could take patient images and automatically calculate patient specific absorbed doses.

Appendices

Appendix A

Sources of uncertainty in measurements and calculations

Uncertainties for all measurements and calculations were determined by listing all relevant uncertainties for each measurement or calculation and adding in quadrature in order to give a total uncertainty as listed in tables and graphs.

Uncertainties associated with nanoDot dosimeters

Coefficient of Variation from readout – specific to each nanoDot readout. Each nanoDot is read four times to give the final average reading. The CV is reported as the mean divided by the standard deviation for each nanoDot.

- Stationary Repeatability – Determined by the manufacturer as 0.0086
- Accuracy of measurement – Determined by manufacturer and verified as 0.05
- Energy dependence – Determined by manufacturer 0.1
- MicroStar ii Reader PMT – Determined by manufacturer 0.008
- MicroStar ii Reader Photodiode – Determined by manufacturer 0.013

Uncertainties associated with GATE simulation

Reported uncertainty – Specific to each run. Given as an output file for each calculated dose point. This uncertainty is calculated as described by Chetty et al.[92] using the history-by-history method for estimating the statistical uncertainty.

- Radcal System HVL accuracy – Determined by manufacturer as 0.05

- Radcal system Energy Dependence – Determined by manufacturer as 0.05

Uncertainties associated with traditional calculation

- Radcal System HVL accuracy – Determined by manufacturer as 0.05

- Radcal system Energy Dependence – Determined by manufacturer as 0.05

- Backscatter factor tables – depending on the source, can have differences of up to 10% between materials [27]–[29].

Uncertainties associated with Algorithm

- Radcal System HVL accuracy – Determined by manufacturer as 0.05

- Radcal system Energy Dependence – Determined by manufacturer as 0.05

- GE XR656 Exposure Index Accuracy – 0.05

117

Appendix B

Sample GATE .mac file for determination of dose at a point at the surface of a geometric phantom simulating a 30x12x25cm block of tissue equivalent material. This .mac file was adapted from examples provided by OpenGATE collaboration [93].

```
#=======================================================

# Adapted from opengate collaboration by Daniel Sandoval

# for dissertation March 2018

#=======================================================



#=======================================================

# VERBOSITY

#=======================================================



/control/execute mac/verbose.mac



#=======================================================

# VISUALISATION

#=======================================================
```

118

```
/control/execute mac/visu.mac


#=======================================================

# GEOMETRY

#=======================================================


/gate/geometry/setMaterialDatabase data/GateMaterials.db


# World

/gate/world/setMaterial            Air

/gate/world/geometry/setXLength    2.0 m

/gate/world/geometry/setYLength    4.0 m

/gate/world/geometry/setZLength    2.0 m

/vis/scene/add/axes

/vis/scene/add/scale


# Superflex phantom non-imported images
```

119

```
/gate/world/daughters/name          superflexphant

/gate/world/daughters/insert        box

/gate/superflexphant/geometry/setXLength  30. cm

/gate/superflexphant/geometry/setYLength  12. cm

/gate/superflexphant/geometry/setZLength  25. cm

/gate/superflexphant/placement/setTranslation 0 -6 0 cm

/gate/superflexphant/setMaterial    AT_AG_SI4_14

/gate/superflexphant/vis/setVisible     1

/gate/superflexphant/vis/setColor       white




#=========================================================

# PHYSICS

#=========================================================



/gate/physics/addPhysicsList QGSP_BERT_HP

/gate/physics/addAtomDeexcitation

/gate/physics/addProcess                PhotoElectric

/gate/physics/addProcess                Compton
```

/gate/physics/addProcess   RayleighScattering gamma

/gate/physics/processes/PhotoElectric/setModel   PenelopeModel

/gate/physics/processes/Compton/setModel   PenelopeModel

/gate/physics/processes/RayleighScattering/setModel PenelopeModel

/gate/physics/Gamma/SetCutInRegion   superflexphant 1.0 mm

/gate/physics/Electron/SetCutInRegion   superflexphant 1.0 mm

/gate/physics/Positron/SetCutInRegion   superflexphant 1.0 mm

/gate/physics/ActivateSpecialCuts e-

#===

DETECTORS

#===

--

the following actor regularly store the current number of

event/track/step in a file

121

```
/gate/actor/addActor          SimulationStatisticActor stat

/gate/actor/stat/saveEveryNSeconds 600



/gate/actor/addActor          TLEDoseActor  1tle

/gate/actor/1tle/attachTo      superflexphant

/gate/actor/1tle/stepHitType     random

/gate/actor/1tle/setSize       4.43 0.3 4.43 mm

/gate/actor/1tle/setVoxelSize     4.43 0.3 4.43 mm

/gate/actor/1tle/setPosition     0 -5.985 0 cm

/gate/actor/1tle/enableDose      true

/gate/actor/1tle/enableUncertaintyDose true

/gate/actor/1tle/enableEdep      true

/gate/actor/1tle/enableUncertaintyEdep true

/gate/actor/1tle/save          output/1TLE-dose.txt



# Set the names of the outputs

/gate/actor/stat/save output/stat.txt
```

```
#========================================================

# INITIALISATION

#========================================================


/gate/run/initialize



#========================================================

# BEAMS

#========================================================


/gate/source/addSource mybeam gps

/gate/source/mybeam/setIntensity 10.0

/gate/source/mybeam/gps/particle gamma

/gate/source/mybeam/gps/ene/mono 36.98 keV

/gate/source/mybeam/gps/centre      0 -1000 0 mm

/gate/source/mybeam/gps/direction    0 1 0

/gate/source/mybeam/gps/pos/type      Point
```

```
/gate/source/mybeam/gps/ang/type      iso

/gate/source/mybeam/gps/ang/mintheta   0. deg

/gate/source/mybeam/gps/ang/maxtheta   13.023 deg

/gate/source/mybeam/gps/ang/minphi    0. deg

/gate/source/mybeam/gps/ang/maxphi    360 deg

/gate/source/mybeam/gps/ang/rot1      1 0 0

/gate/source/mybeam/gps/ang/rot2      0 0 1

/gate/source/mybeam/gps/pos/rot1      1 0 0

/gate/source/mybeam/gps/pos/rot2      0 0 1

#========================================================

# START BEAMS

#========================================================

/gate/random/setEngineName MersenneTwister

/gate/random/setEngineSeed auto

/gate/application/setTotalNumberOfPrimaries 10

/gate/application/start
```

References

[1] M. Bhargavan and J. H. Sunshine, "Utilization of Radiology Services in the United States: Levels and Trends in Modalities, Regions, and Populations," *Radiology*, vol. 234, no. 3, pp. 824–832, Mar. 2005.

[2] R. Smith-Bindman *et al.*, "Use of Diagnostic Imaging Studies and Associated Radiation Exposure for Patients Enrolled in Large Integrated Health Care Systems, 1996-2010," *JAMA*, vol. 307, no. 22, pp. 1030–1037, Jun. 2012.

[3] R. S. of N. A. RSNA, "X-ray (Radiography) - Chest," *RadiologyInfo.org for patients*, 2016. [Online]. Available: http://www.radiologyinfo.org/en/info.cfm?pg=chestrad. [Accessed: 26-Jun-2016].

[4] N. E. M. A. NEMA, "Medical Imaging Modalities," *MITA - Medical Imaging Technology Alliance*, 2016. [Online]. Available: http://www.medicalimaging.org/about-mita/medical-imaging-primer/#x-ray. [Accessed: 26-Jun-2016].

[5] J. W. Gurney, M. DeVries, and C. Johnson, "Information for Patients," *Chest X-ray.com: The Art and Science of Thoracic imaging*. [Online]. Available: http://www.chestx-ray.com/index.php/education/informationforpatients. [Accessed: 22-Sep-2016].

[6] M. M. Rehani and W. Pavlicek, "Patient Radiation Exposure: Tracking Why Track Previous Exposures?," in *American Association of Physicists in Medicine Annual Meeting*, 2011.

[7] M. K. Yee, "Joint Commission releases requirements for imaging services," *website article*, 2015. [Online]. Available: http://www.auntminnie.com/index.aspx?sec=ser&sub=def&pag=dis&ItemID=109842. [Accessed: 26-Jun-2016].

[8] S. Don, "Radiosensitivity of children: potential for overexposure in CR and DR and magnitude of doses in ordinary radiographic examinations.," *Pediatr. Radiol.*, vol. 34 Suppl 3, pp. S167-72–41, Oct. 2004.

[9] S. Walker, D. Allen, C. Burnside, and L. Small, "Determining the between exposure factors, dose and exposure index value in digital radiographic imaging," *Synergy*, no. October, pp. 14–17, 2011.

[10] W. R. Hendee, M. K. O'Connor, and M. K. O'Connor, "Radiation Risks of Medical Imaging: Separating Fact from Fantasy," *Radiology*, vol. 264, no. 2, pp. 312–321, Aug. 2012.

[11] AAPM, "Position statement of the American Association of Physicists in Medicine, Radiation risks from medical imaging procedures.," 2011. [Online]. Available: http://www.aapm.org/org/policies/details.asp?id=318&type=PP. [Accessed: 10-Sep-2016].

[12]   Health Physics Society, "Position statement of the health physics Society, Radiation risk in perspective," 2016. [Online]. Available: http://hps.org/documents/risk_ps010-3.pdf. [Accessed: 10-Sep-2016].

[13]   E. C. Lin, "Radiation risk from medical imaging.," *Mayo Clin. Proc.*, vol. 85, no. 12, p. 1142–6; quiz 1146, Dec. 2010.

[14]   M. Tubiana, L. E. Feinendegen, C. Yang, and J. M. Kaminski, "Linear No-Threshold Relationship Is Inconsistent with Radiation Biologic and Experimental Data," *Radiology*, vol. 251, no. 1, pp. 13–22, Apr. 2009.

[15]   U. Mothiram, P. C. Brennan, S. J. Lewis, B. Moran, and J. Robinson, "Digital radiography exposure indices: A review.," *J. Med. Radiat. Sci.*, vol. 61, no. 2, pp. 112–8, Jun. 2014.

[16]   S. J. Shepard *et al.*, "An exposure indicator for digital radiography: AAPM Task Group 116 (executive summary).," *Med. Phys.*, vol. 36, no. 7, pp. 2898–914, Jul. 2009.

[17]   (IEC) International Electrotechnical Commission, "Medical electrical equipment—exposure index of digital X-ray imaging systems - Part 1: definitions and requirements for general radiography," Geneva, Switzerland, International Standard IEC 62494-1, 2008.

[18]   J. A. Seibert and R. L. Morin, "The standardized exposure index for digital radiography: an opportunity for optimization of radiation dose to the pediatric population.," *Pediatr. Radiol.*, vol. 41, no. 5, pp. 573–81, May 2011.

[19]   M. D. Cohen, M. L. Cooper, K. Piersall, and B. K. Apgar, "Quality assurance: Using the exposure index and the deviation index to monitor radiation exposure for portable chest radiographs in neonates," in *Pediatric Radiology*, 2011, vol. 41, no. 5, pp. 592–601.

[20]   IEC 62494-1, "Medical electrical equipment – Exposure Index of digital X-ray imaging systems – Part 1: Definitions and requirements for general radiography," 1.0, 2008.

[21]   S. Jeon, "DETECTOR EXPOSURE INDICATOR IN GE X-RAY SYSTEMS," Chalfont St. Giles, 2014.

[22]   T. R. Silva and E. M. Yoshimura, "Patient dose, gray level and exposure index with a computed radiography system," *Radiat. Phys. Chem.*, vol. 95, pp. 271–273, 2014.

[23]   J. Johnson, "A Dose Monitoring Program for Computed Radiography," Duke University, 2012.

[24]   D. K. Olivera Ciraj, Srpko Markovic, O. Ciraj-Bjelac, S. Markovic, and D. Kosutic, "Patient dosimetry in diagnostic radiology," *Nucl. Technol. Radiat. Prot.*, vol. 18, no. 1, p. 6, 2003.

[25]   M. T. Taha, F. H. Al-Ghorabie, R. A. Kutbi, and W. K. Saib, "Assessment of

126

entrance skin doses for patients undergoing diagnostic X-ray examinations in King Abdullah Medical City, Makkah, KSA," *J. Radiat. Res. Appl. Sci.*, vol. 8, no. 1, pp. 100–103, 2015.

[26] T. Kiljunen, A. Tietavainen, T. Parvianen, A. Viitala, and M. Kortesniemi, "Organ Doses and Effective Doses in Pediatric Radiography: Patient-Dose Survey in Finland," *Acta radiol.*, vol. 50, no. 1, pp. 114–124, 2009.

[27] R. M. Harrison, "Backscatter factors for diagnostic radiology (1-4 mm Al HVL)," *Phys. Med. Biol.*, vol. 27, no. 12, pp. 1465–1474, Dec. 1982.

[28] R. Sharma, S. D. Sharma, S. Pawar, A. Chaubey, S. Kantharia, and D. A. R. Babu, "Radiation dose to patients from X-ray radiographic examinations using computed radiography imaging system.," *J. Med. Phys.*, vol. 40, no. 1, pp. 29–37, 2015.

[29] N. Petoussi-Henss, M. Zankl, G. Drexler, W. Panzer, and D. Regulla, "Calculation of backscatter factors for diagnostic radiology using Monte Carlo methods.," *Phys. Med. Biol.*, vol. 43, no. 8, pp. 2237–50, Aug. 1998.

[30] L. Stanton, S. D. Brattelli, J. L. Day, R. E. Stanton, and T. Villafana, "Measurements of diagnostic x-ray backscatter by a novel ion chamber method," *Med. Phys.*, vol. 9, no. 1, pp. 121–130, Jan. 1982.

[31] B. Grosswendt, "Dependence of the photon backscatter factor for water on source-to-phantom distance and irradiation field size," *Phys. Med. Biol.*, vol. 35, no. 9, pp. 1233–1245, Sep. 1990.

[32] J. H. Hubbell, "Photon Mass Attenuation and Mass Energy-Absorption Coefficients for H, C, N, O, Ar, and Seven Mixtures from 0.1 keV to 20 MeV," *Radiat. Res.*, vol. 70, no. 1, p. 58, Apr. 1977.

[33] F. H. Attix, *Introduction to Radiological Physics and Radiation Dosimetry.* Wiley-VCH, 1991.

[34] M. Tapiovaara and T. Siiskonen, "PCXMC." Stuk, Helsinki, 2008.

[35] T. J. Wood, C. S. Moore, J. R. Saunderson, and A. W. Beavis, "Validation of a technique for estimating organ doses for kilovoltage cone-beam CT of the prostate using the PCXMC 2.0 patient dose calculator," *J. Radiol. Prot.*, vol. 35, no. 1, pp. 153–163, Mar. 2015.

[36] O. Rampado, F. R. Giglioli, V. Rossetti, C. Fiandra, R. Ragona, and R. Ropolo, "Evaluation of various approaches for assessing dose indicators and patient organ doses resulting from radiotherapy cone-beam CT," *Med. Phys.*, vol. 43, no. 5, pp. 2515–2526, May 2016.

[37] N. Khelassi-Toutaoui *et al.*, "Experimental evaluation of PCXMC and prepare codes used in conventional radiology.," *Radiat. Prot. Dosimetry*, vol. 131, no. 3, pp. 374–8, 2008.

[38] M. S. Jeff Shepard, C. Pei-Jan Paul Lin, C.-C. M. John Boone Dianna D

127

Cody Jane R Fisher G Donald Frey Hy Glasser, J. E. Gray Arthur G Haus Lance V Hefner Richard L Holmes, J. J. Robert Kobistek Frank N Ranallo Philip L Rauch Raymond P Rossi, and J. J. Anthony Seibert Keith Strauss Orhan H Suleiman Joel R Schenck Stephen K Thompson, "AAPM Report No. 74 QUALITY CONTROL IN DIAGNOSTIC RADIOLOGY Report of Task Group #12 Diagnostic X-ray Imaging Committee," College park, 2002.

[39] C.-M. Ma *et al.*, "AAPM protocol for 40–300 kV x-ray beam dosimetry in radiotherapy and radiobiology," *Med. Phys.*, vol. 28, no. 6, pp. 868–893, 2001.

[40] S. J. Shepard *et al.*, "Recommended Exposure Indicator for Digital Radiography ," *Rep. AAPM Task Gr. # 116*, no. 116, pp. 1–46, 2009.

[41] R. Y. L. Chu *et al.*, "STANDARDIZED METHODS FOR MEASURING DIAGNOSTIC X-RAY EXPOSURES REPORT OF TASK GROUP 8 DIAGNOSTIC X-RAY IMAGING COMMITTEE," New York, 1990.

[42] H. E. Johns and J. R. Cunningham, *The Physics of Radiology 4th Edition*. Springfield: Charles C Thomas Pub Ltd, 1983.

[43] L. F. Brateman and P. H. Heintz, "Meaningful Data or Just Measurements? Differences Between Ionization Chamber and Solid-State Detectors," *J. Am. Coll. Radiol.*, vol. 12, no. 9, pp. 951–953, 2015.

[44] D. W. Jordan, "Advanced Portable Radiation Instruments for Diagnostic Imaging QC," in *AAPM Annual Meeting*, 2011.

[45] J. T. Bushberg, J. A. Seibert, E. M. Leidholdt Jr., and J. M. Boone, *The Essential Physics of Medical Imaging*, 3rd ed. Philadelphia, PA: LWW, 2011.

[46] J. T. Bushberg, *The Essential physics of medical imaging*, 2nd ed. Baltimore: Williams & Wilkins, 2002.

[47] T. Okazaki *et al.*, "Fundamental Study of nanoDot OSL Dosimeters for Entrance Skin Dose Measurement in Diagnostic X-ray Examinations," *J. Radiat. Prot. Res.*, vol. 41, no. 3, pp. 229–236, Sep. 2016.

[48] P. A. Jursinic, "Characterization of optically stimulated luminescent dosimeters, OSLDs, for clinical dosimetric measurements," *Med. Phys.*, vol. 34, no. 12, pp. 1690–1699, 2007.

[49] J. Thistlethwaite, D. Johnson, and D. J. Valentino, "microSTARii - A new system for medical dosimetry: Part I: Technology & Initial Performance," 2013.

[50] Ž. Knežević, L. Stolarczyk, I. Bessieres, J. M. Bordy, S. Miljanić, and P. Olko, "Photon dosimetry methods outside the target volume in radiation therapy: Optically stimulated luminescence (OSL), thermoluminescence (TL) and radiophotoluminescence (RPL) dosimetry," *Radiat. Meas.*, vol. 57, pp. 9–18, Oct. 2013.

[51] Landauer, "nanoDot and microSTARii Frequently Asked Questions." 2014.

[52] C. J. Yahnke, "Calibrating the microStar," 2009.

[53] C. J. Yahnke and D. Ph, "Calibrating the microStar," *Energy*, pp. 1–22, 2010.

[54] C. S. Reft, "The energy dependence and dose response of a commercial optically stimulated luminescent detector for kilovoltage photon, megavoltage photon, and electron, proton, and carbon beams.," *Med. Phys.*, vol. 36, no. 5, pp. 1690–1699, 2009.

[55] Landauer, "InLight ® Complete Dosimetry System Solution: nanoDot Dosimeter," 2012.

[56] B. Grosswendt, "Backscatter factors for x-rays generated at voltages between 10 and 100 kV," *Phys. Med. Biol.*, vol. 29, no. 5, pp. 579–591, May 1984.

[57] R. M. Harrison *et al.*, "Central-axis depth-dose data for diagnostic radiology," *Phys. Med. Biol.*, vol. 26, no. 4, pp. 657–670, Jul. 1981.

[58] S.-Y. Park, C. H. Choi, J. M. Park, M. Chun, J. H. Han, and J. Kim, "A Patient-Specific Polylactic Acid Bolus Made by a 3D Printer for Breast Cancer Radiation Therapy," *PLoS One*, vol. 11, no. 12, p. e0168063, 2016.

[59] J. H. Hubbell and S. M. Seltzer, "Tables of X-Ray Mass Attenuation Coefficients and Mass Energy-Absorption Coefficients from 1 keV to 20 MeV for Elements Z = 1 to 92 and 48 Additional Substances of Dosimetric Interest," *NIST*, 1996. [Online]. Available: https://www.nist.gov/pml/x-ray-mass-attenuation-coefficients. [Accessed: 03-Jan-2018].

[60] S. Jan *et al.*, "GATE: a simulation toolkit for PET and SPECT," *Phys. Med. Biol*, vol. 49, pp. 4543–4561, 2004.

[61] R. Hill, B. Healy, L. Holloway, Z. Kuncic, D. Thwaites, and C. Baldock, "Advances in kilovoltage x-ray beam dosimetry," *Phys. Med. Biol.*, vol. 59, no. 6, p. R183, Mar. 2014.

[62] A. (Andreas) Kling, *Advanced Monte Carlo for radiation physics, particle transport simulation, and applications : proceedings of the Monte Carlo 2000 Conference, Lisbon, 23-26 October 2000*. Springer, 2001.

[63] J. Sempau, J. Fernandez-Varea, E. Acosta, and F. Salvat, "Experimental benchmarks of the Monte Carlo code PENELOPE," *Nucl. Instruments Methods Phys. Res.*, no. B 207, pp. 107–23, 2003.

[64] S. Agostinelli *et al.*, "Geant4—a simulation toolkit," *Nucl. Instruments Methods Phys. Res.*, no. A 506, pp. 250–303, 2003.

[65] C. A. Schneider, W. S. Rasband, and K. W. Eliceiri, "NIH Image to ImageJ: 25 years of image analysis," *Nat. Methods*, vol. 9, p. 671, Jun. 2012.

[66] P. Seroul and D. Sarrut, "VV - A viewer for the evaluation of 4D image

registration," *MIDAS J. (Medical Image …*, pp. 1–8, 2008.

[67]   D. Sarrut *et al.*, "A review of the use and potential of the GATE Monte Carlo simulation code for radiation therapy and dosimetry applications," *Med. Phys.*, vol. 41, no. 6, 2014.

[68]   F. Baldacci *et al.*, "A track length estimator method for dose calculations in low-energy X-ray irradiations: Implementation, properties and performance," *Z. Med. Phys.*, vol. 25, no. 1, pp. 36–47, 2015.

[69]   F. Verhaegen *et al.*, "Monte Carlo modelling of external radiotherapy photon beams," *Phys. Med. Biol.*, vol. 48, no. 21, pp. R107–R164, Nov. 2003.

[70]   J. Seuntjens, H. Thierens, A. Van der Plaetsen, and O. Segaert, "Conversion factor f for X-ray beam qualities, specified by peak tube potential and HVL value.," *Phys. Med. Biol.*, vol. 32, no. 5, pp. 595–603, May 1987.

[71]   G. Poludniowski, G. Landry, F. Deblois, P. M. Evans, and F. Verhaegen, "SpekCalc: a program to calculate photon spectra from tungsten anode x-ray tubes," *Phys. Med. Biol.*, vol. 54, no. N433, pp. 433–438, 2009.

[72]   D. Sandoval, G. Hatch, C. Gerrard, and P. Heintz, "Validation of a Novel CT Breast Dosimetry Method in Post Mortem, Unembalmed Female Subjects," *AAPM*, vol. 40, no. 6. Medical Physics, Indianapolis, IN, p. 458, 2013.

[73]   L. Sinclair *et al.*, "Determining Organ Doses from CT with Direct Measurements in Postmortem Subjects: Part 2-Correlations with Patient-specific Parameters.," *Radiology*, vol. 0, no. 0, p. 140971, 2015.

[74]   T. M. Griglock, L. Sinclair, A. Mench, and B. Cormack, "Determining Organ Doses from CT with Direct Measurements in Methodology and Validation 1," *Radiology*, vol. 0, no. 0, pp. 1–8, 2015.

[75]   D. J. Sandoval, W. Weber, D. Melo, G. M. Hatch, N. Adolphi, and P. H. Heintz, "3.7. Radiation dosimetry comparison between ante-mortem and post-mortem animal tissue: Is post- mortem radiation dosimetry an adequate proxy for measurements in the living?," *J. Forensic Radiol. Imaging*, vol. 2, no. 2, p. 106, Apr. 2014.

[76]   P. Heintz, B. Heintz, D. Sandoval, W. Weber, D. Melo, and R. Guilmette, "SU-ET-481: In Vivo and Post Mortem Animal Irradiation: Measured Vs. Calculated Doses," *Med. Phys.*, vol. 42, no. 6, p. 3445, 2015.

[77]   A. Phantoms, "Alderson Lung/Chest Phantom." 2014.

[78]   CDC, *Biosafety in Microbiological and Biomedical Laboratories (BMBL)*, 5th ed. Health and Human Services, 2009.

[79]   P.-J. P. Lin *et al.*, "Accuracy and calibration of integrated radiation output indicators in diagnostic radiology: A report of the AAPM Imaging Physics Committee Task Group 190," *Med. Phys.*, vol. 42, no. 12, pp. 6815–6829, 2015.

[80] ICRP, "Managing Patient Dose in Digital Radiology. ICRP Publication 93," Stockholm, 2004.

[81] M. S. Stecker *et al.*, "Guidelines for Patient Radiation Dose Management," *J. Vasc. Interv. Radiol.*, vol. 20, no. 7 SUPPL., pp. S263–S273, 2009.

[82] ICRP *et al.*, "ICRP Publication 120: Radiological Protection in Cardiology," *Ann. ICRP*, vol. 42, no. 1, pp. 1–125, 2013.

[83] M. Winslow *et al.*, "USE OF THE VIP-MAN MODEL TO CALCULATE ENERGY IMPARTED AND EFFECTIVE DOSE FOR X-RAY EXAMINATIONS," *Health Phys.*, vol. 86, no. 2, pp. 174–182, 2004.

[84] S. M. Seltzer *et al.*, "Report 85 FUNDAMENTAL QUANTITIES AND UNITS FOR IONIZING RADIATION (Revised)," Oxford, 2011.

[85] G. A. Carlsson, D. R. Dance, J. Persliden, and M. Sandborg, "Use of the concept of energy imparted in diagnostic radiology," *Appl. Radiat. Isot.*, vol. 50, no. 1, pp. 39–62, Jan. 1999.

[86] F. Happey, "The Integration of Radiation Dosage and the Absorption of Energy in Tissue for X and Gamma Radiation," *Br. J. Radiol.*, vol. 14, no. 163, pp. 235–241, Jul. 1941.

[87] R. M. Harrison, "A re-evaluation of the 'saturated scatter' method for estimating the energy imparted to patients during diagnostic radiology examinations," *Phys. Med. Biol.*, vol. 28, no. 6, pp. 701–707, Jun. 1983.

[88] ICRU, "ICRU Report 74," Oxford, 2005.

[89] F. M. Khan, *The physics of radiation therapy*, 4th ed. Baltimore: Lippincott Williams & Wilkins, 2010.

[90] S. Jozela, "Beam Quality Specification in Kilo-voltage Radiotherapy," University of the Witwatersrand Johannesburg, 2007.

[91] W. S. Rasband, "ImageJ." U. S. National Institutes of Health, Bethesda, Maryland, USA.

[92] I. J. Chetty *et al.*, "Reporting and analyzing statistical uncertainties in Monte Carlo–based treatment planning," *Int. J. Radiat. Oncol.*, vol. 65, no. 4, pp. 1249–1259, 2006.

[93] OpenGATE collaboration, "GATE." [Online]. Available: http://www.opengatecollaboration.org/home. [Accessed: 28-Oct-2017].